

12-15-2014

Experimental and Theoretical Studies of Native and Engineered Vascular Tissue Mechanics

Boran Zhou
University of South Carolina - Columbia

Follow this and additional works at: <https://scholarcommons.sc.edu/etd>



Part of the [Biomedical Engineering and Bioengineering Commons](#)

Recommended Citation

Zhou, B.(2014). *Experimental and Theoretical Studies of Native and Engineered Vascular Tissue Mechanics*. (Doctoral dissertation). Retrieved from <https://scholarcommons.sc.edu/etd/3023>

This Open Access Dissertation is brought to you by Scholar Commons. It has been accepted for inclusion in Theses and Dissertations by an authorized administrator of Scholar Commons. For more information, please contact digres@mailbox.sc.edu.

EXPERIMENTAL AND THEORETICAL STUDIES OF NATIVE AND
ENGINEERED VASCULAR TISSUE MECHANICS

by

Boran Zhou

Bachelor of Science
Harbin Institute of Technology, 2009

Submitted in Partial Fulfillment of the Requirements

For the Degree of Doctor of Philosophy in

Biomedical Engineering

College of Engineering and Computing

University of South Carolina

2014

Accepted by:

Tarek Shazly, Major Professor

Melissa Moss, Committee Member

Mark Uline, Committee Member

Xiaomin Deng, Committee Member

Lacy Ford, Vice Provost and Dean of Graduate Studies

ACKNOWLEDGEMENTS

I would like to thank my supervisor Prof. Tarek Shazly for giving me the opportunity to be a part of his laboratory. He provided me with the scientific advice and the enthusiasm without which this work could not be possible. Moreover, I would like to thank him for his encouragement and support to establish collaborations and for his friendship and understanding.

I would also like to thank the members of committee for their time and expertise: Prof. Melissa Moss, Prof. Mark Uline and Prof. Xiaomin Deng.

I express my sincere thanks to Prof. Alexander Rachev for helping me understand theories of biomechanics; Prof. William Scott Argraves and Sandy Klatt for providing tissue-engineered constructs; Prof. Susan Lessner, Prof. Michael Sutton and Prof. John Eberth for letting me use their machines. I would also want to give my thanks to all my group-mates, colleagues: Dr. Jahid Ferdous, Eva Juarez Perez, Gabr Mohamed, Moreira Alexandra, David Primm, and friends who are always with me for suggestions and encouragements. Most importantly, I would like to thank my parents and my sister for their love and support all through my life.

ABSTRACT

Background Implantation of vascular grafts provides a means to restore blood flow in compromised regions of the circulatory system, and thus is used to treat a wide range of cardiovascular diseases. Despite significant advancements in autologous grafting strategies as well as the engineering of synthetic alternatives, mechanical, structural, and compositional incongruities between the graft and the host artery remain as contributing factors to graft failure. The typical failure modality manifests as proximal anastomotic intimal hyperplasia, which places restrictions on the host vessel size currently treated with grafting strategies (> 5 mm internal diameter). In order to improve long-term clinical outcomes, this project is devoted to experimental investigations of native and engineered vascular mechanics, with development of structure-motivated constitutive models that promote both the optimal selection of native vascular grafts and fabrication of engineered vascular substitutes.

Dissertation summary The overall goal of this project is to characterize and model the mechanical properties of native arteries, with focus on the primary renal artery, as well as a representative material for the engineering vascular substitutes. In our first set of studies, we employed an integrated experimental-theoretical methodology to study the passive mechanical behavior of porcine primary renal artery. Inflation-extension tests and structure-motivated constitutive models were used to characterize the contribution of structural constituents, such as elastin and collagen, to the macroscopic mechanical

response of the arterial wall. In our next set of studies, we sought to understand how vascular smooth muscle cell contractile states modulate the mechanical responses of arterial wall. Active stresses induced by vascular smooth muscle cell contraction were derived via isometric contraction studies, and analytical expressions to characterize the biaxial active stress-strain relationships were proposed. Thirdly, for the sake of appropriate selection of an autologous source for coronary artery end-to-end grafting, the passive mechanical behaviors of porcine coronary artery, internal thoracic artery, radial artery, great and lateral saphenous veins were assessed and compared. Differences in compliance, average wall stresses, and deformed inner radii between the coronary artery and the graft were proposed as a basis for optimal tissue selection and implantation strategy. Finally, the mechanical properties of novel engineered vascular constructs were characterized as a function of fabrication protocol. The mechanical response of tissue-engineered constructs, and more specifically the compositional determinants of exhibited behavior, indicates these materials could be further developed for grafting applications. Taken together, the studies encompassed in this dissertation provide a comprehensive framework to improve the clinical implementation of autologous vascular grafts and direct the engineering of vascular substitutes.

TABLE OF CONTENTS

ACKNOWLEDGEMENTS	ii
ABSTRACT	iii
LIST OF TABLES	ix
LIST OF FIGURES	viii
CHAPTER 1: INTRODUCTION	1
1.1 OVERVIEW	1
1.2 SCOPE	6
CHAPTER 2: PASSIVE MECHANICS OF PRIMARY RENAL ARTERIES	10
2.1 ABSTRACT	10
2.2 INTRODUCTION	11
2.3 MATERIALS AND METHODS	14
2.4 RESULTS	20
2.5 DISCUSSION	28
2.6 STUDY LIMITATIONS	29
2.7 CONCLUSIONS	30
2.8 STUDY TRANSITION	31

CHAPTER 3: BIAxIAL VASOACTIVITY OF PRIMARY RENAL ARTERIES	32
3.1 ABSTRACT	32
3.2 INTRODUCTION.....	32
3.3 MATERIALS AND METHODS	35
3.4 RESULTS.....	40
3.5 DISCUSSION	47
3.6 STUDY LIMITATIONS.....	49
3.7 CONCLUSIONS.....	50
3.8 STUDY TRANSITION.....	50
CHAPTER 4 : MECHANICAL ANALYSIS OF AUTOLOGOUS CORONARY ARTERY GRAFTS	51
4.1 ABSTRACT	51
4.2 INTRODUCTION.....	51
4.3 MATERIALS AND METHODS.....	54
4.4 RESULTS.....	57
4.5 DISCUSSION	68
4.6 STUDY LIMITATIONS.....	71
4.7 CONCLUSION	72
CHAPTER 5 : MECHANICAL CHARACTERIZATION OF TISSUE-ENGINEERED VASCULAR CONSTRUCTS	73
5.1 ABSTRACT	73
5.2 INTRODUCTION.....	74

5.3	MATERIALS AND METHODS	77
5.4	RESULTS.....	84
5.5	DISCUSSION	92
5.6	STUDY LIMITATIONS.....	95
5.7	CONCLUSIONS.....	96
CHAPTER 6 :CONCLUSION		97
6.1	DISSERTATION SUMMARY.....	97
6.2	FUTURE STUDIES.....	99
BIBLIOGRAPHY.....		102

LIST OF TABLES

Table 2.1. Geometry of stress-free configuration of porcine primary renal artery.....	22
Table 2.2. Best-fit parameters from the structure-motivated model and dimensions of the zero-stress configuration of six porcine renal arteries. Mean and standard deviation of each value are listed below.	24
Table 3.1. The vessel geometry in the stress-free configuration for each arterial test segment. L_i , L_o , H , Φ are the outer arc length, inner arc length, opening angle, wall thickness, respectively.	41
Table 3.2. Parameters of the proposed analytical expression fitting the active circumferential and axial stresses of the porcine primary renal artery.	47
Table 4.1. Vessel geometry of stress-free configuration.	61
Table 4.2. Material parameters of CA, ITA, RA, GSV and LSV obtained for a four-fiber constitutive model.	64
Table 4.3. Vessel structural properties at representative graft loading conditions ($\lambda_z = 1.2$, $P = 100$ mmHg).....	65
Table 4.4. Vessel mechanical properties at homeostatic and graft loading conditions	66
Table 5.1. Incremental elastic moduli of cellularized and decellularized constructs.	88
Table 5.2. Geometric parameters of statically stretched specimens.	90
Table 5.3. Incremental elastic moduli of elastin and collagen of unstretched and stretched cellularized constructs.....	91
Table 5.4. Burst pressure and geometry of tube.	92

LIST OF FIGURES

Figure 1.1. A schematic illustration of artery in the healthy and atherosclerotic states[4].	2
Figure 1.2. A schematic representation of coronary artery bypass grafting [20].	3
Figure 1.3. A schematic representation of tissue-engineered blood vessels[31].	4
Figure 2.1. A schematic representation of the idealized geometries of the zero-stress configuration (left) and a picture of the primary renal artery in the stress-free configuration (right).	15
Figure 2.2 Experimental setup for extension-inflation testing of vascular specimens (Bose BioDynamic 5270).	16
Figure 2.3. Schematics of the idealized geometries of the (a) zero-stress and (b) deformed arterial configurations.	18
Figure 3.1. Representative pressure-deformed outer diameter and axial wall force-pressure relationships of the porcine primary renal artery at three levels of axial stretch ($\lambda_z = 1.2, 1.3, \text{ or } 1.4$) and at either maximally contracted (\bullet) or fully relaxed (\circ) smooth muscle states. Error bars denote standard deviation of three repeat measurements at each experimental state.	42
Figure 3.2. Representative deformed outer diameter-axial stretch and axial wall force-axial stretch relationships of the porcine primary renal artery at three levels of axial stretch ($\lambda_z = 1.2, 1.3, \text{ or } 1.4$) and at either maximally contracted (\bullet) or fully relaxed (\circ) smooth muscle cells states. Error bars denote standard deviation of three repeat measurements at each experimental state.	43
Figure 3.3. Representative comparison of experimental values and theoretical predictions of circumferential stress-circumferential stretch (A), axial stress-circumferential stretch (B), circumferential stress-axial stretch (C) and axial stress-axial stretch relationships of the porcine primary renal artery at either maximally contracted (\bullet) or fully relaxed (\circ) smooth muscle cells states. Error bars denote standard deviation of three repeat measurements at each experimental state.	44

Figure 3.4. Representative comparison of experimental values (data points) and theoretical predictions (curves) for both the active circumferential (A) and axial (B) stress-stretch ratio of the porcine primary renal artery	46
Figure 4.1. Representative plots of pressure-diameter (A), axial force-axial stretch (B) and compliance-pressure (C) relationships for CA, ITA, RA, GSV and LSV. Compliance calculated at 20 mmHg at the grafted axial stretch ratio.	60
Figure 4.2. Histology of (A) CA, (B) ITA, (C) RA, (D) GSV and (E) LSV.	62
Figure 4.3. Circumferential stress distribution across the vessel wall of (A) CA, (B) ITA, (C) RA, (D) GSV and (E) LSV under physiological loading conditions of coronary artery.....	63
Figure 4.4. Comparison of normalized difference in comprehensive mechanical properties (A), in stresses between homeostatic and grafted loading states (B), in compliance under grafted loading conditions (C), internal radius under grafted loading conditions (D) of RA, ITA, GSV and LSV(mean \pm SD, n=5 for each group) among different groups. (*) $p < 0.05$ represents a significant statistical difference compared with internal thoracic artery.	67
Figure 4.5. Vessel normalized difference in overall mechanical properties as a function of axial stretch ratio.....	68
Figure 5.1. Fabricated Tubular Constructs. A, B, C, and D show different views of an elongated tubular construct that has been cultured for 17 days, E and F show the spherical microcarriers.	78
Figure 5.2. (A) bio-inert posts made of PLA, (B) posts placed in the molds.	79
Figure 5.3. (A) torroids on the post of 2mm. (B) torroids placed on the 3mm post. (C) sideview of stretched torroids.	79
Figure 5.4. A, B, C and D display different view of stacked tube.....	80
Figure 5.5. (A) Experimental Setup of Uniaxial Tensile Testing. (B) Close view of samples. Arrow pointing at the Toroid undergoing displacement.....	81
Figure 5.6. Acquired images from a uniaxial ring experiment on an engineering vascular construct. The distance between markers contained within the central region of the sample longitudinal axis was measured in the undeformed (a) and deformed (b) states to facilitate calculation of a local stretch ratio. The scale bar refers to both images.	82
Figure 5.7. Experimental setup of burst pressure on the fabricated tube.....	83

Figure 5.8. (A) Experimental setup of suture retention strength test. The picture above shows the construct sutured to the plastic cannula mandrel on left, with the moveable post on the right (B) pulling the suture through the vessel wall. 84

Figure 5.9. Experimental preconditioning and data obtained from uniaxial ring test. (A) Ring constructs were preconditioned via three loading-unloading cycles to obtain a reproducible elastic response. (B) Immediately following preconditioning, an identical fourth cycle was performed, and loading data processed to develop stress-stretch relations. Error bars represent the standard deviation of measurements made on four samples. 85

Figure 5.10. (A), Experimental stretch-stress responses (means \pm SE) of cellularized tissue constructs (n=5 tissue constructs from each culture period) and (B), Comparison of experimental stretch- stress responses (means \pm SE) of cellularized and decellularized 17 day constructs (n=5 for each)..... 86

Figure 5.11. Comparison of ultimate tensile strength of cellularized and decellularized constructs. 88

Figure 5.12. Cauchy stress-stretch relationship consisting of elastin dominant, transition and collagen dominant phases of tissue constructs..... 89

Figure 5.13. Comparison of outer diameter (A), inner diameter (B) and thickness (C) among different vascular constructs. 90

Figure 5.14. Comparison of incremental elastic moduli of elastin (A) and collagen (B) as well as comparison of ultimate tensile strength between agarose molds and stretched samples (C) among various fabricated constructs. 91

Figure 7.1. Predicted pressure-outer diameter relationships of cellularized constructs at various culture times 101

CHAPTER 1

INTRODUCTION

1.1 OVERVIEW

Cardiovascular Disease

Cardiovascular disease (CVD) is the leading cause of morbidity and mortality in the United States. It is estimated that 83.6 million American adults carry one or more forms of CVD, with corresponding annual medical cost of \$121.2 billion [1]. Atherosclerosis is the most prevalent manifestation of CVD, and is characterized by the presence of plaques on the vascular wall (Figure 1.1). Plaques are composed of cholesterol and lipid residing on the intima of affected vasculature. Atherosclerotic plaques can impede blood flow and lead to acute ischemia in local tissue, as in the case of a myocardial infarction caused by coronary artery occlusion. Alternatively, mechanically unstable plaques can rupture, under physiological loading and distal vessel occlusion, as typified by cerebral stroke [2]. The genesis and progression of most forms of CVD are in part attributed to damage of arterial endothelium, which is promoted by risk factors including hypertension, high levels of cholesterol, and smoking [3]. The mechanical properties of native vessels play a major part in understanding the physiological and pathophysiological functions of the vessels, having important clinical implications in the diagnosis and treatment of patients with coronary artery disease and atherosclerosis.

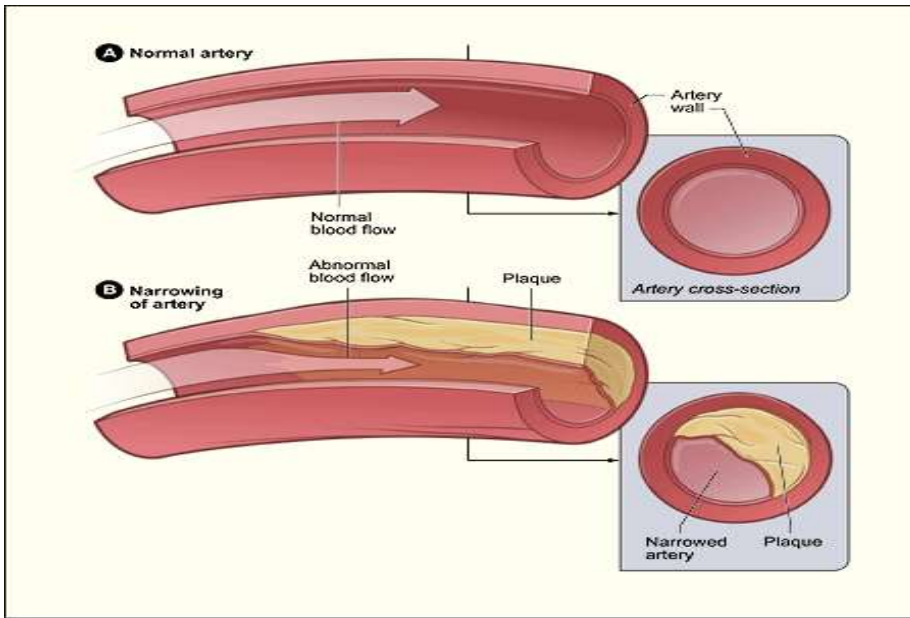


Figure 1.1. A schematic illustration of artery in the healthy and atherosclerotic states[4].

Surgical revascularization

Surgical revascularization procedures are widely employed for treating CVD [5-12]. Coronary arteriovenous graft is mainly used for myocardial revascularization, relieving ischemic resistant to medicine and preventing myocardial infarction. Selection of the graft conduits plays a significant part in ensuring successful rate of arteriovenous graft and increasing its patency as well as patient's survival rate. Venous bypass grafts, such as great and lateral saphenous veins, were firstly developed and are still in use for arteriovenous graft [13]. However, due to premature vein graft blockage and failure, such as graft thrombosis and atherosclerosis, arterial conduits such as left internal mammary artery (LIMA) with better long-term patency rate are used as alternative methods [14-17]. Furthermore, radial artery (RA) with less risk of infection and injury in re-operative surgery is considered as the second best coronary bypass graft [18, 19] (Figure 1.2).

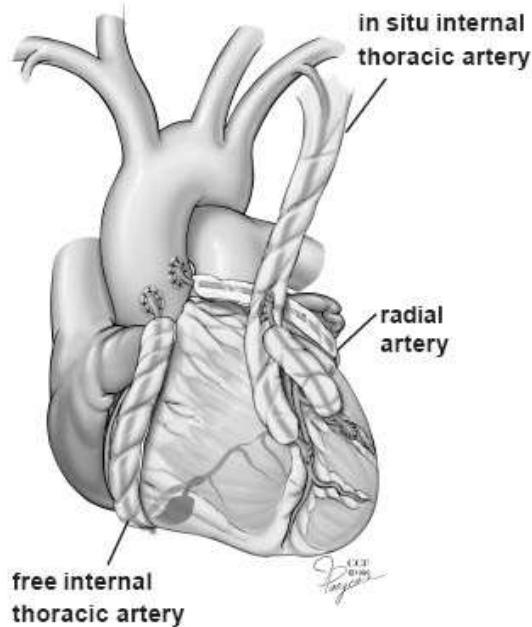


Figure 1.2. A schematic representation of coronary artery bypass grafting [20].

Tissue engineered vascular prostheses

Each year, hundreds of thousands of people undergo vein or artery replacement surgeries. However, systemic vascular disease often means that autologous replacement blood vessels are not available. Despite great advancements in vascular tissue engineering, development of functional arterial replacement grafts that meet requirements for mechanical strength and stiffness and which mimic the biological functionality of a native vessel has been elusive.

A variety of approaches have been developed to fabricate blood vessels [21-25]. These include the use of tubular scaffolds manufactured from natural and synthetic biomaterials that are subsequently seeded with vascular cells to create living prostheses [26-29] (Figure 1.3). A potentially promising approach to fabricate blood vessels is to

stimulate cells to synthesize extracellular matrix (ECM) and form scaffolds with composition and mechanical properties comparable to native blood vessels [30].

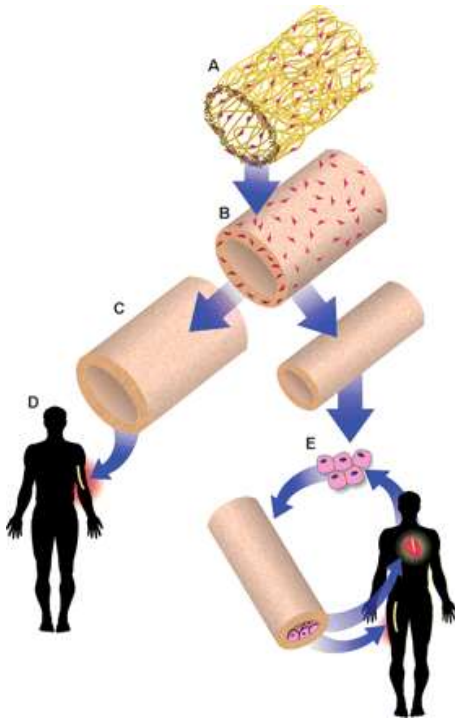


Figure 1.3. A schematic representation of tissue-engineered blood vessels[31].

State of the art of vascular biomechanics

Arteries are multi-layered structures with arranged fibers embedded in an amorphous matrix, with mechanical behavior that is nonlinear. It is accepted that elastin fibers are the primary load-bearing elements over the range of low pressures, while collagen fibers are gradually recruited and bear load at higher pressures [32]. Constitutive models in terms of invariant-based strain energy functions are used to describe this nonlinear elastic behavior. Three main groups of models for vascular tissue mechanics have been proposed based on the principles of continuum mechanics. In all approaches, the arterial tissue is considered as a nonlinear elastic, orthotropic, and incompressible

material. Phenomenological models propose a strain energy density function (SEF) in terms of single analytical function of the components of the strain tensor, from which all stress-strain constitutive relations follow [33, 34]. The functional form and the material constants of the SEF are identified based on a best fit between experimentally recorded data and corresponding theoretical predictions. While phenomenological models can accurately match experimental data, they cannot offer insight into the structural and compositional features of the tissue that give rise to observed mechanical behavior. Conversely, structure-based, one-phase models account for the contribution of the major structural load-bearing constituents of the arterial wall, e.g. elastin, collagen, and vascular smooth muscle cells, by identifying the SEF using a particular structure-based analytical form [35, 36]. Finally, structural-based models coupled with the theory of constrained mixtures result in SEFs that account for the individual mechanical properties and the amount of the structural load-bearing constituents [37, 38]. The theory of constrained mixtures facilitates assessment of arterial remodeling based not only on mechanical stimuli, but also in regards to the specific composition of a given vessel.

In addition to vascular passive responses resulting from the mechanical properties of the intramural elastin and collagen, arterial compliance is also affected by the dynamics of vascular smooth muscle cells (VSMCs). The temporary alteration of the level of VSMCs activation modulates the lumen diameter of blood vessel so as to restore the baseline value of local flow-induced shear stress. Numerous studies have been conducted to study the contribution of VSMCs contractile states to strain and stress distribution across the arterial wall [39-42]. Furthermore, synthetic and proliferative activity of the VSMCs in response to changes in hemodynamic loads was proposed to be

highly associated with VSMCs basal tone, leading to vascular stress-induced remodeling [43-47].

Identification of reference configuration is of great importance for calculating strains and stresses. If a radial cut is introduced on an unloaded ring segment obtained from artery, it springs open into a sector, implying the existence of circumferential residual strains and stresses within the arterial wall due to differential growth during development [21, 48]. Residual strain is quantified by an opening angle bisecting the sector and proposed to homogenize the stress field within the arterial wall under physiological loads [48].

1.2 SCOPE

Among the numerous biomechanical investigations devoted to large blood vessels, surprisingly few have focused on the primary renal arteries. Of the published studies, none provide insight into the stresses experienced by vascular cells under normal or disease states. Wall stresses and strains constitute the local mechanical environment of mechanosensitive vascular cells and thus are major factors governing arterial performance. Wall stresses cannot be measured but instead are calculated via solving a boundary value problem for the deformed vessel, requiring the formulation and identification of the constitutive equations for the renal artery in terms of soft tissue continuum mechanics. Because mechanobiological processes play a key role in not only vascular homeostasis but also pathological progression, identifying the structural determinants of vascular biomechanics is a necessary step to understand the functional consequences of vascular disease and developing therapeutic strategies to restore vessel function. Moreover, the predictive results from solving boundary value problems within

the proposed model can promote assessments for the effects of some therapeutic procedure and can give guidance for optimizing their efficiency.

The following questions, hypotheses and specific aims drive this project, which seeks to provide a basis for selecting coronary arterial end-to-end grafts and designing better tissue-engineered vascular substitutes.

Open Questions

1. How do the primary structural constituents, elastin and collagen, contribute to the passive mechanical response of the primary renal artery?
2. How does multi-axial vascular smooth muscle cell contraction affect the mechanical behavior of the primary renal artery?
3. Will plausible alteration of the axial stretch of an autologous vascular graft significantly impact its mechanical performance?
4. Do established structure-function relationships in native arterial tissue also apply to the mechanical response of engineered vascular substitutes?

Specific Aims

A majority of the published investigations on blood vessel mechanics refer to the thoracic, carotid, coronary, abdominal, or cerebral arteries [37, 49-52]. The sparse published data on renal arteries provide only descriptive information when the smooth muscle is either fully relaxed (passive response) or activated to contract (active response) [53]. Studies to date cannot provide insights into the multifactorial nature of phenomena that dictate renal artery mechanics and cannot predict the arterial response resulting from altered geometry, structure, and loading conditions. There is a pressing need for structure

and function-motivated comprehensive experimental investigations and adequate mathematical modeling, the results of which can bridge the gap in the current knowledge about: (i) the individual contribution of basic structural vascular components (elastin, collagen, and smooth muscle) to the mechanical response; (ii) the multiaxial effects of the smooth muscle contraction; and (iii) a structure-motivated constitutive formulation of the mechanical properties of renal artery tissue that accounts for both the passive and active response. The central premise of this study is that the volume fractions of structural elements and the active response developed by the vascular smooth muscle can be experimentally recorded and incorporated into a constrained mixture rheological model to describe and predict the mechanical performance of renal arteries and genesis of some vascular disorders.

Specific Aim 1: Quantify the contributions of the passive structural components to the mechanical behavior of the primary renal artery

Working hypothesis: The spatial organization, and individual mechanical properties of elastin and collagen can be incorporated into a three-dimensional, one-layered model of the renal artery, the parameters of which can be identified and the predictive power verified from an appropriate set of bi-axial mechanical experiments for the passive mechanical response.

Specific Aim 2: Characterize the biaxial mechanical effects of vascular smooth muscle cells (VSMCs) within the renal arterial wall and incorporate the active stress into constitutive equations of the arterial tissue.

Working hypothesis: Stimulated VSMCs modulate arterial mechanics via generation of active tension in the circumferential and longitudinal directions.

Specific Aim 3: Investigate the passive mechanical and structural properties of various blood vessels and predict their mechanical compatibility in the context of forming end-to-end vascular grafts to the coronary artery.

Working hypothesis: Aiming to reduce the disturbance of the local mechanical environment at the anastomosis, the clinical feasibility of the autologous vascular graft is indicated by the discrepancy in structural and mechanical properties between graft and host artery.

Specific Aim 4: Quantify the mechanical response of fabricated vascular tissue constructs in a uniaxial tensile as well as burst pressure and suture retention experiments.

Working hypothesis: Biofabricated tissue constructs can be modeled as nonlinear, elastic, isotropic, incompressible materials. The results of one-dimensional testing are sufficient to fully characterize the mechanical properties of tissue engineered vascular substitutes prior to structural reorganization induced via mechanical preconditioning.

CHAPTER 2

PASSIVE MECHANICS OF PRIMARY RENAL ARTERIES

2.1. ABSTRACT

The primary renal arteries transport up to one fourth of cardiac output to the kidneys for blood plasma ultrafiltration, with a functional dependence on the vessel geometry, composition, and mechanical properties. Despite the critical physiological function of the renal artery, the few biomechanical studies that have focused on this vessel are either uniaxial or only partially describe its bi-axial mechanical behavior. In this study, we quantify the passive mechanical response of the porcine primary renal artery through bi-axial mechanical testing that probes the pressure-deformed diameter and pressure-axial force relationships at various longitudinal extensions, including the in-vivo axial stretch ratio. Mechanical data are used to parameterize and validate a structure-motivated constitutive model of the arterial wall. Together, experimental data and theoretical predictions of the stress distribution within the arterial wall provide a comprehensive description of the passive mechanical response of the porcine primary renal artery.

2.2. INTRODUCTION

The primary renal artery is a large conduit vessel that directs blood flow to kidneys, and thus is critical to both specific organ function and overall health. As is characteristic for muscle-type vessels, the physiological role of the renal artery is not only to convey but also regulate blood flow in response to mechanical and/or biochemical stimuli [54]. An adaptive mechanical response evokes a change in lumen diameter that tends to maintain blood flow rate and wall stresses at baseline values [55]. Alterations in vessel geometry, tissue mechanical properties, or vasomotor function can lead to a maladaptive arterial response that manifests as arterial occlusion, reduced blood supply, or abnormal wall stress distribution [56]. Renal vascular disease (RVD) is associated with arterial maladaptation and occurs in approximately 7% of the elderly population, potentially causing stenosis, renovascular hypertension, chronic renal insufficiency, or end-stage renal disease. In addition to compromising kidney function, RVD can incite systemic disorders, including impairments of acid-base blood balance, electrolyte concentrations, and extracellular fluid volume [21-23, 57]. Due to the critical nature of kidney physiologic functions and the impact on overall health as well as clinical significance for surgical procedure, there is a pressing need for mechanical characterization of the renal artery.

The renal arteries direct approximately 25% of cardiac output to the kidneys for glomerular filtration, playing a critical role in both specific organ function and overall health [38, 52]. Renal arteries are muscle-type vessels that control blood flow through changes in lumen diameter, with functional dependence on initial vessel geometry, mechanical properties of the vascular tissue, contractile state of the vascular smooth

muscle cells (VSMCs), and arterial pressure. Cumulatively, these factors determine the stress field within the arterial wall and thus impact the phenotype of mechanosensitive vascular cells [38, 52]. Because stresses are not directly measured but rather calculated, an integrated experimental/theoretical approach is required to understand the mechanical behavior of the renal artery and the factors that govern mechanically-mediated biological processes.

The sparse published biomechanical data on renal arteries are either uniaxial or only partially describe as opposed to explain the fundamental determinants of mechanical behavior [24, 38, 47, 52]. Studies to date cannot provide insights into the multifactorial and multidirectional nature of phenomena that dictate renal artery mechanics and cannot predict how structural or compositional alterations in the arterial wall will impact vessel performance. The dynamic environment of the renal artery implies that retention of performance depends on the ability of the vessel to respond appropriately to change. The high muscle content of renal arteries enables a rapid alteration of vessel tone in response to transient fluctuations in blood flow or pressure. Vessel tone is tuned via SMC contraction, which is a mechanosensitive process that is concurrently mediated by flow-induced shear at the endothelium, pressure-induced medial stretch, and baroreceptor signaling from the sympathetic nervous system [25, 56, 58, 59]. Arteries respond to long-term alterations in arterial pressure and blood flow by changing geometry, structure, and composition. This response is termed remodeling and plays an important role in normal arterial physiology and in the genesis and progression of certain vascular disorders [49, 56, 60]. Remodeling results from the altered vascular cell activity caused by perturbed local stresses and strains, which trigger a series of events that ultimately lead to cell

proliferation, hyperplasia, cell apoptosis or necrosis, hypertrophy, and cell migration, and elicits imbalance between extracellular matrix synthesis and degradation. Adaptive remodeling is long-term responsive process of arterial tissue that preserves the baseline mechanical environment in the arterial wall despite sustained changes in loading, the former characterized by local stresses and strains and the latter by blood flow rate, arterial pressure, and longitudinal stretching [61-64]. Maladaptive remodeling occurs when the baseline mechanical state is not fully restored, resulting in suboptimal values of flow-induced shear stress at the endothelium, circumferential wall stresses, and/or linearized structural wall stiffness in the physiologic strain range [62, 65-67]. Maladaptive remodeling is postulated to be a contributing factor and potentially the underlying cause of various manifestations of cardiovascular disease (CVD) [68-70]. With CVD accounting for almost half of deaths in industrialized nations, it is important to understand the fundamental process of arterial remodeling in all vital regions of the circulatory system.

From both a basic science and clinical perspective, there is a clear need for structure- and function-motivated comprehensive experimental investigations and adequate mathematical modeling of renal artery mechanics, the results of which will provide a structure-based constitutive formulation of renal artery tissue that delineates the individual contributions of primary load-bearing elements to the overall mechanical behavior. The central premise of our study is that the processes underlying renal artery mechanical behavior caused by changes in the global mechanical environment and/or arterial structure can be understood with structure-based mathematical models that

account for simultaneous, stress-driven alterations of the mass and mechanical properties of the main structural constituents of the arterial wall.

2.3. MATERIALS AND METHODS

Kidneys (n=6) were harvested from 7 month old pigs (mean weight of 240 pounds) at the local slaughterhouse. The kidneys were rinsed with saline solution, stored in an ice-cold solution, and transported to the laboratory.

Vessel isolation

All tissue handling protocols were approved by the Institutional Animal Care and Use Committee at the University of South Carolina. Upon kidney arrival, the primary renal artery was isolated from the surrounding tissue, washed in phosphate buffered saline (PBS), dissected free of perivascular tissue, and mounted on stainless steel cannula for mechanical testing. Prior to excision, the in situ length of the vessel segment prior to excision (L_{in_situ}) and following excision (L) were measured and used to calculate the in situ axial stretch ratio ($\lambda_{in} = L_{in_situ}/L_{no\ load}$).

Zero-stress configuration

It is well-established that the zero-stress configuration of an artery is close to a circular sector and can be obtained after a radial cut on an unloaded ring segment. The zero-stress configurations of renal artery samples were assessed via image analysis (ImageJ) of opened-up ring segments that had reached an equilibrated state (Figure 2.1). The inner (L_i) and outer (L_o) arc lengths and cross-sectional area (A) were measured for multiple rings from each arterial sample, and used to calculate the opening angle (Φ_o) and wall thickness (H) of the circular sector as follows:

$$\Phi_o = \pi - \frac{L_o - L_i}{2H} \quad \text{and} \quad H = \frac{2A}{(L_o + L_i)} \quad (2.1)$$

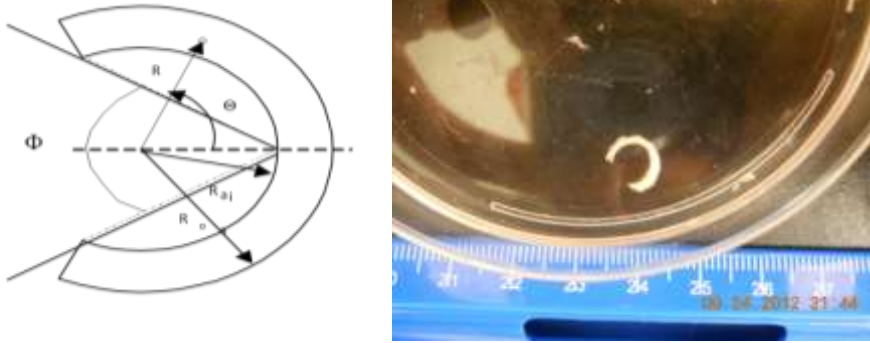


Figure 2.1. A schematic representation of the idealized geometries of the zero-stress configuration (left) and a picture of the primary renal artery in the stress-free configuration (right).

Mechanical testing

A chambered vascular testing system (Bose BioDynamic 5270, Figure 2.2) will be configured to impart controlled luminal perfusion and constant axial stretch to excised segments of porcine renal vasculature. Automated system software (Wintest 4.1) and an external camera integrated via LabVIEW (National Instruments) will be used to continuously monitor vessel geometry, luminal pressure and axial force. Arterial segments were mounted onto stainless steel cannula to perform inflation-extension tests. Throughout mechanical testing, arteries will be maintained in Krebs solution (37 °C and Ph 7.4) and continuously bubbled with standard gas (95% O₂ + 5% CO₂).



Figure 2.2. Experimental setup for extension-inflation testing of vascular specimens (Bose BioDynamic 5270).

Arteries were extended to $L_{in-situ}$ and preconditioned with five inflation/deflation cycles (pressure range 0 – 200 mmHg) via controlled luminal flow of PBS to obtain an elastic pressure-diameter response. Segments were extended and held at fixed lengths (l) that yield axial stretch ratios ($\lambda_z = l/L_{no_load}$) ranging from 90% to 110% of the native value. For quasi-static pressure-diameter testing, segments were pressurized up to 200 mmHg with 25 mmHg steps at a step rate of 0.2 mmHg/s. The average axial force, luminal pressure, and outer diameter recorded over a 30 second interval were reported for each experimental state (pressure and axial stretch ratio). At the end of mechanical testing, six rings (1 mm length) were cut from regions spanning the vessel length. Ring segments were used to determine the composition of the arterial wall.

Histological analysis

Histological analyses of vessel segments were conducted in parallel to measure the amount of structural components and provide further insight into their relative

influence on renal artery mechanics. Following mechanical testing, multiple ring samples from each arterial test segment were paraffin-embedded and processed with Verhoeff-Van Gieson and picrosirius red staining protocols. Image analysis (ImagePro and ImageJ) of histological slides was used to estimate the area fractions of elastin and collagen within each segment. Average values were recorded for each vessel and expressed as a percentage of total vessel dry mass.

Constitutive modeling

Mechanical testing data can describe the mechanical response of the artery in terms of pressure-diameter relationships at different longitudinal stretch ratios and force-longitudinal stretch ratio relationships at different pressures. However, this information does not reveal the mechanical properties of the vascular tissues in terms of stress-strain relations, as the stress field in the arterial wall cannot be measured. In a range of basic science and medical arenas, including disease diagnosis, cellular signal mechanotransduction, and arterial tissue biofabrication, it is advantageous to understand the individual contribution of basic structural constituents to the entire arterial mechanical response. Accordingly, one of the major objectives of vascular biomechanics is the determination of the constitutive equations that describe tissue mechanical properties and allow formulating and solving boundary value problems with predictive power.

To achieve this goal, a mathematical model of the passive mechanical response of the renal artery was developed based on the following assumptions: (i) the opened configuration obtained after a radial cut on an unloaded arterial segment is considered as a circular sector and is taken as a stress-free reference configuration for calculating

strains, thus accounting for the effects of the residual strains that exist in the traction free configuration; (ii) arterial geometry is considered as a 3-D thick-walled cylindrical tube under applied pressure and longitudinal extension in an axisymmetric deformed state; (iii) the arterial wall is a constrained mixture of elastin, collagen and smooth muscle cells (SMCs), with each constituent representing a non-linear elastic incompressible solid that undergoes finite deformations; (iv) the contribution of the vascular SMCs to the passive response is negligible.

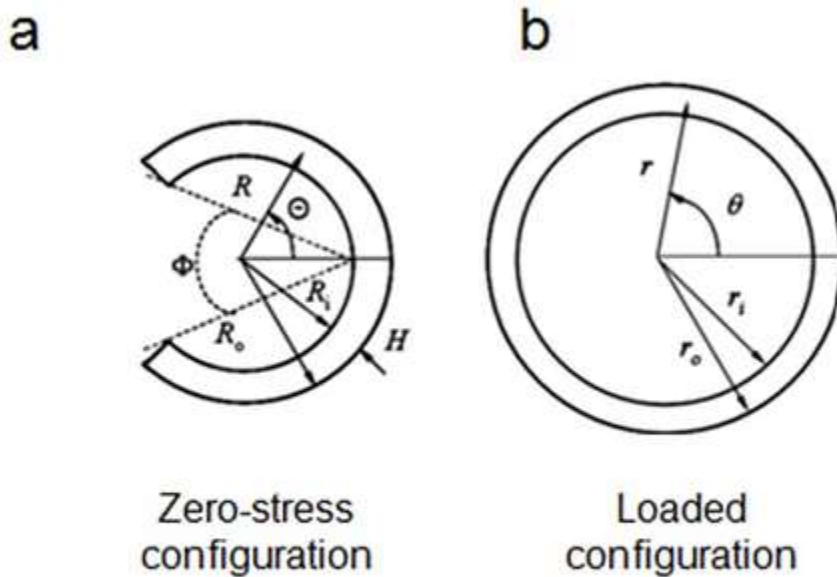


Figure 2.3. Schematics of the idealized geometries of the (a) zero-stress and (b) deformed arterial configurations.

The deformation of the artery is characterized by the right Cauchy-Green strain tensor defined as:

$$[C] = \text{diag}\{\lambda_r^2, \lambda_\theta^2, \lambda_z^2\} = \text{diag}\left\{\left(\frac{dr}{dR}\right)^2, \left(\frac{\chi r}{R}\right)^2, \lambda^2\right\}, \quad (2.2)$$

Where λ_i $i = r, \theta, z$ are the stretch ratios in the radial, circumferential and longitudinal direction, respectively; R and r are the current undeformed and deformed radii; Φ is the opening angle (Figure 2.3); and $\chi = \pi/(\pi - \Phi)$.

The passive Cauchy stress tensor $[T^p]$ is developed by the elastin and collagen and defined as.

$$[T^p] = \text{diag}\{t_r^p, t_\theta^p, t_z^p\} = \text{diag}\left\{p + \lambda_r \frac{\partial W}{\partial \lambda_r}, p + \lambda_\theta \frac{\partial W}{\partial \lambda_\theta}, p + \lambda_z \frac{\partial W}{\partial \lambda_z}\right\} \quad (2.3)$$

where p is unknown function due to the incompressibility of the mixture and also accounts for the mechanical contribution of the water fraction; W is the strain energy density function;

We adapted a previously proposed structure-motivated strain energy function and seek W in the following form:

$$W = c(I_1 - 3) + \sum_{k=1,2,3,4} \frac{b_{1k}}{2b_{2k}} \{ \exp[b_{2k}(\lambda_k^2 - 1)^2] - 1 \} \quad (2.4)$$

where k denotes a family of collagen fibers oriented at a mean angle of $\pm \alpha_k$ with respect to the longitudinal (z) direction; c , b_{1k} , and b_{2k} are material constants; $I_1 = \lambda_r^2 + \lambda_\theta^2 + \lambda_z^2$ is the first invariant of the right Cauchy-Green strain tensor; and $\lambda_k^2 = \lambda_r^2 \sin^2(\alpha_k) + \lambda_z^2 \cos^2(\alpha_k)$ describes the stretch of each family of collagen fibers.

The mathematical model briefly described above motivates the experimental testing in the previous subsection. Given the analytical form of the functions in the constitutive equations, the experimental data are acquired and processed to determine model variables and parameters.

For quasi-static inflation-extension of an artery, given the initial geometry, longitudinal stretch ratio, and the constitutive equations for the passive mechanical response, it can be shown that the theoretically calculated pressure (P^T) and axial force (f_{wall}^T) are,

$$P^T = \int_{r_i}^{r_o} \left(\lambda_\theta \frac{\partial W}{\partial \lambda_\theta} - \lambda_r \frac{\partial W}{\partial \lambda_r} \right) \frac{dr}{r}, \quad \int_{r_i}^{r_o} \left(2 \left(\lambda_z \frac{\partial W}{\partial \lambda_z} \right) - \lambda_\theta \frac{\partial W}{\partial \lambda_\theta} - \lambda_r \frac{\partial W}{\partial \lambda_r} \right) r dr \quad (2.5)$$

where r_i and r_o is the vessel deformed inner and outer radius, respectively.

The material constants (c , b_{1k} , b_{2k}) were determined via non-linear regression of measured P and f_{wall} (MATLAB). The parameterized model was validated by comparing model predictions against recorded experimental data that have not been used for parameter identification.

2.4. RESULTS

Pressure-diameter and pressure-axial force curves

Quasi-static inflation-extension tests of the primary porcine renal arteries generated bi-axial data describing the passive mechanical response. The pressure-outer deformed diameter relationships exhibited a high degree of nonlinearity at all examined levels of fixed axial stretch (Figure 2.4 (A)). The renal artery Peterson's modulus (E_p) was calculated for each vessel at physiologic loading conditions ($P = 13.33$ kPa, $\lambda_z = \lambda_{in-situ}$), with an average value of 251.3 ± 133.5 kPa.

An increase in pressure generally caused an increase in the axial wall force at axial stretch ratios at or above the in situ value, although an inverse trend was exhibited at low pressure (Figure 2.4 (B)). Vessel bucking was induced at higher pressures when

the axial stretch ratio was below the in-situ value, requiring the exclusion of corresponding data from the mechanical testing data set. Increased axial stretch resulted in higher axial force at all pressures.

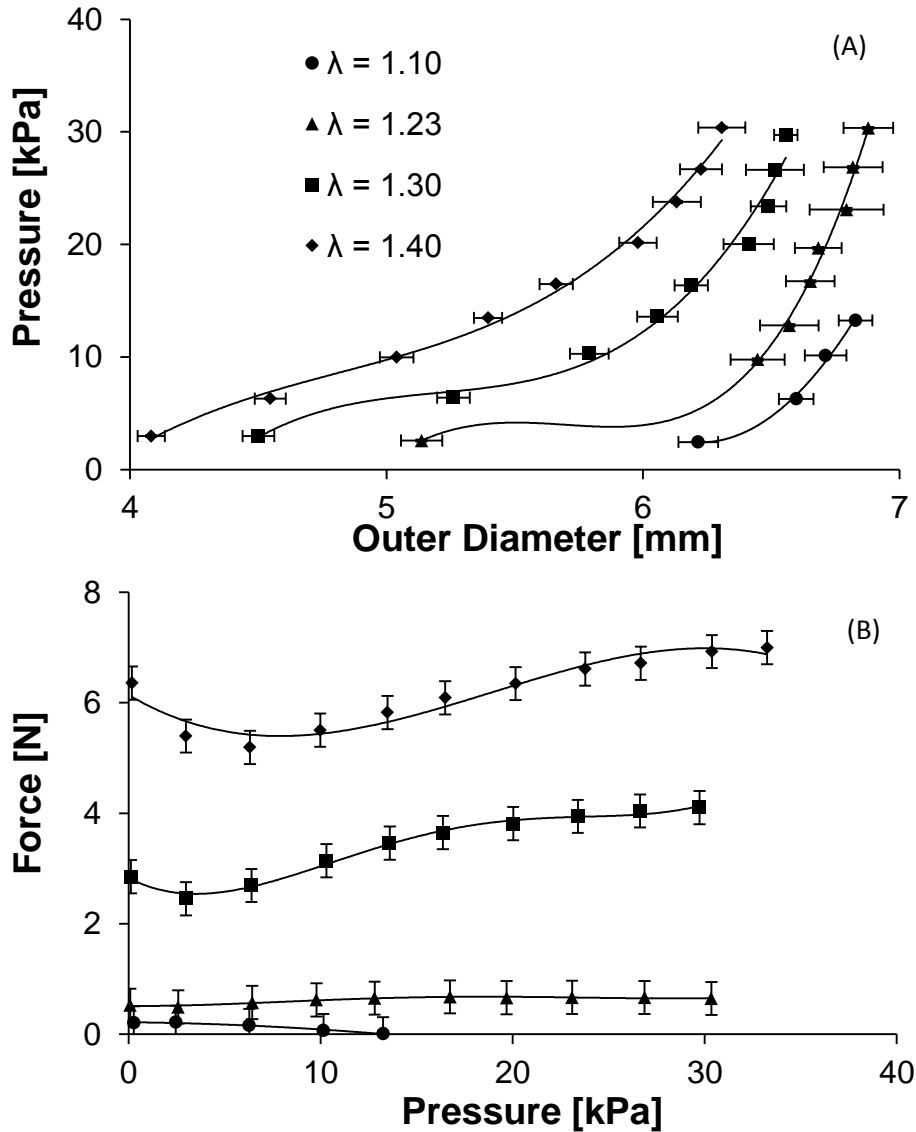


Figure 2.4. Representative data for the pressure-deformed outer diameter (A) and axial wall force-pressure (B) relationships of the porcine primary renal artery at four levels of axial stretch (1.1, 1.23, 1.3 and 1.4). Data points represent mean values (n=3); error bars denote standard deviation.

Zero-stress configuration

The zero-stress configuration of the renal artery was modeled as a circular sector characterized by an inner arc length, outer arc length, and wall area, with average dimensions of 13.4 ± 2.8 mm, 17.3 ± 2.4 mm, and 17.8 ± 0.9 mm², respectively. The opening angle of each sector was calculated based on these measurements, with an average value of $84.0 \pm 12.4^\circ$. The geometrical parameters characterizing the zero-stress configuration are reported for each vessel in Table 2.1.

Table 2.1. Geometry of stress-free configuration of porcine primary renal artery

Vessel	R_i [mm]	H [mm]	Φ [°]	L_i [mm]	L_o [mm]	A [mm ²]
1	4.58	1.47	82.55	15.59	20.59	26.61
2	4.41	1.47	105.48	11.47	15.29	19.69
3	3.04	1.29	79.68	10.65	15.16	16.64
4	2.99	1.21	72.52	11.21	15.76	16.34
5	5.70	0.63	90.58	17.78	19.75	11.88
6	3.71	0.90	73.43	13.79	17.13	13.89
Avg.	4.07	1.16	84.04	13.41	17.28	17.84
STD.	1.04	0.33	12.40	2.83	2.36	0.87

Arterial wall composition

The dry area fractions of elastin and collagen in the arterial wall were determined via histological staining and image analyses (Figure 2.5). Elastin had an area fraction of 12.6 ± 0.05 % and was primarily concentrated in the internal elastic lamina. Collagen had an area fraction of 36.4 ± 0.08 %, with a relatively greater concentration in the adventitia as compared to the media.

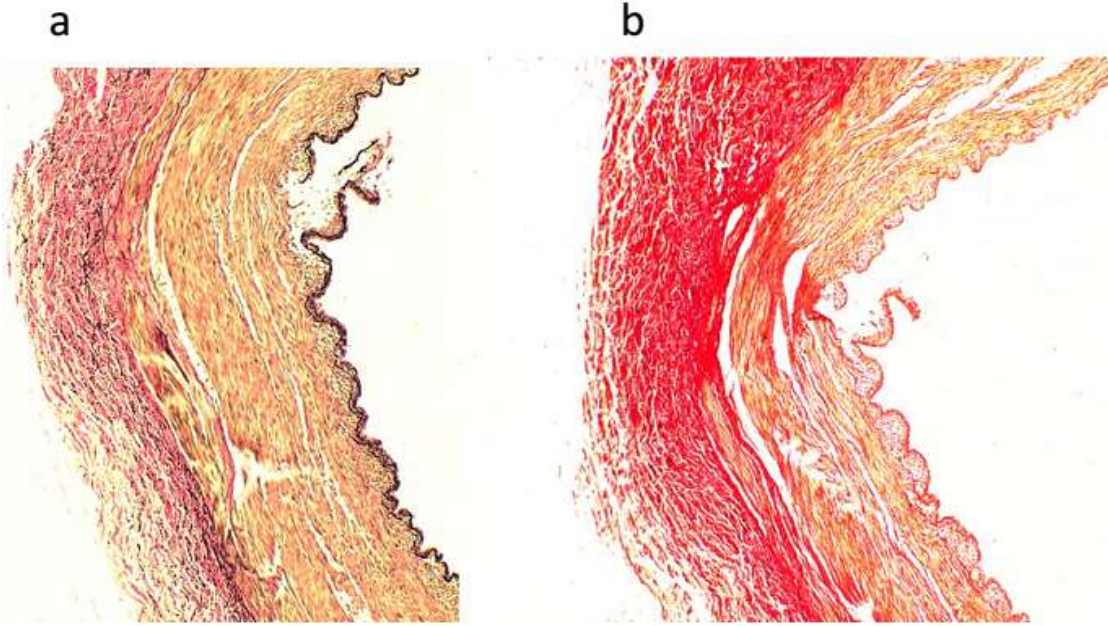


Figure 2.5. Representative histological images of the porcine renal artery wall viewed at 40x magnification. Elastin is black under Verhoeff-Van Gieson staining (a), while collagen is pink/red under picrosirius red staining (b). Quantitative image analysis based on hue, saturation, and luminescence thresholds was used to measure the dry mass fractions of total wall elastin and collagen.

Parameter identification

The parameter values for the proposed constitutive model were identified based on non-linear regression between experimental and theoretical P and f (Table 2.2). The resultant parameter values were obtained via programming of the following value boundary limits and initial guesses in the fitting algorithm. The identified values for all parameters were insensitive to the selected boundary limits and the initial guesses. The reported residual values were calculated as follows, and correspond to acceptable fits between experimental and theoretical data:

$$Residual = \left\{ 0.5 \sum_{i=1}^N \left(\frac{P_E - P_T}{P_E} \right)^2 + 0.5 \sum_{i=1}^N \left(\frac{f_E - f_T}{f_E} \right)^2 \right\} \quad (2.6)$$

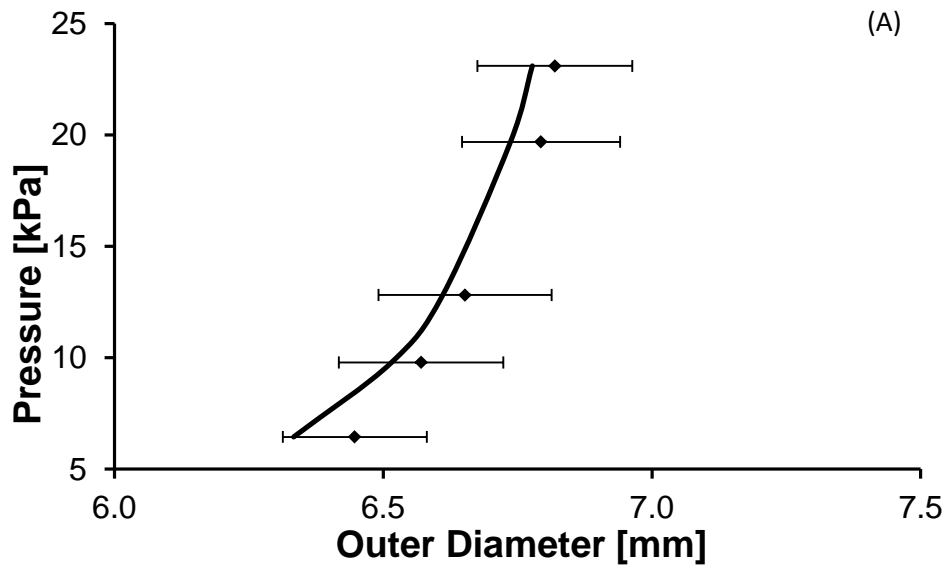
where subscripts E and T denote experimental and theoretical values, respectively.

Table 2.2. Best-fit parameters from the structure-motivated model and dimensions of the zero-stress configuration of six porcine renal arteries. Mean and standard deviation of each value are listed below.

Vessel	c [kPa]	b_{11} [kPa]	b_{12}	b_{21} [kPa]	b_{22}	b_{31} and b_{41} [kPa]	b_{32} and b_{42}	α_1 [deg]	α_2 [deg]	α_3 [deg]	α_4 [deg]	Residual
1	5.1	3.0	0.5	54.7	0.9	7.0	6.9	90	0	57.7	-57.7	0.7
2	19.4	6.7	6.2	0.5	4.6	6.1	6.9	90	0	46.4	-46.4	1.5
3	0.5	17.6	6.6	9.1	5.5	36.0	1.9	90	0	34.8	-34.8	0.6
4	0.5	16.0	7.9	9.7	3.6	33.6	3.0	90	0	42.2	-42.2	1.1
5	0.5	45.5	6.2	14.6	4.6	5.6	6.3	90	0	90.0	-90.0	1.3
6	2.7	5.0	6.2	16.0	2.6	7.7	4.3	90	0	38.1	-38.1	1.9
Avg.	4.8	15.6	5.6	17.4	3.6	16.0	4.9	90	0	51.5	-51.5	1.2
STD.	7.4	15.8	2.6	19.1	1.7	14.6	2.1	0	0	20.4	-20.4	0.5

Model validation

Model predictions for the pressure-diameter and force-axial stretch (Figure 2.6) relationships of the renal artery agreed well with experimental data over the examined range of mechanical behavior. Moreover, predicted mean stress versus stretch curves in the circumferential and axial (Figure 2.7) directions also agreed with the measured mechanical response.



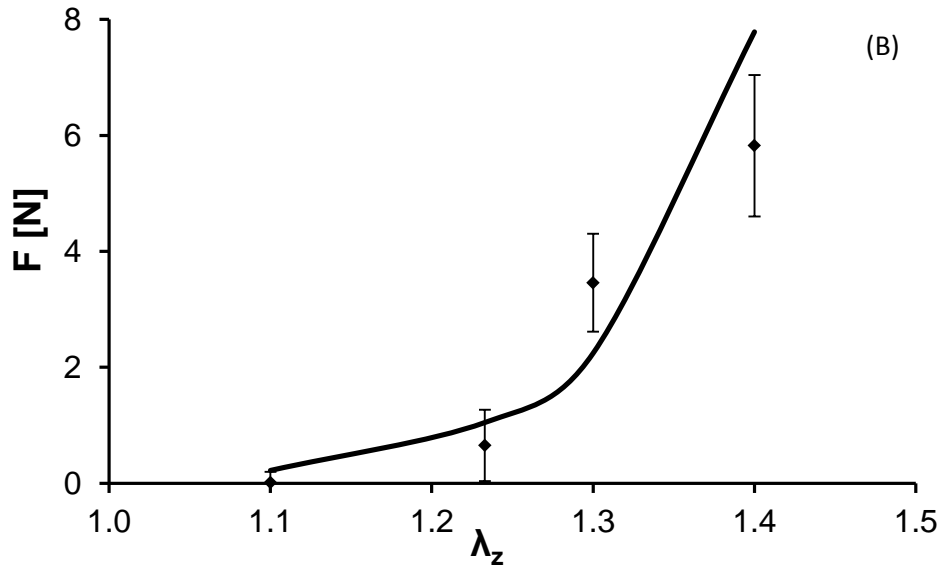


Figure 2.6. Representative comparison of experimental values (data points) and theoretical predictions (curves) for the (A) pressure-deformed outer diameter and (B) wall force-axial stretch ratio relationships of the porcine renal artery. Error bars denote standard deviation of experimental measurements ($n = 3$).

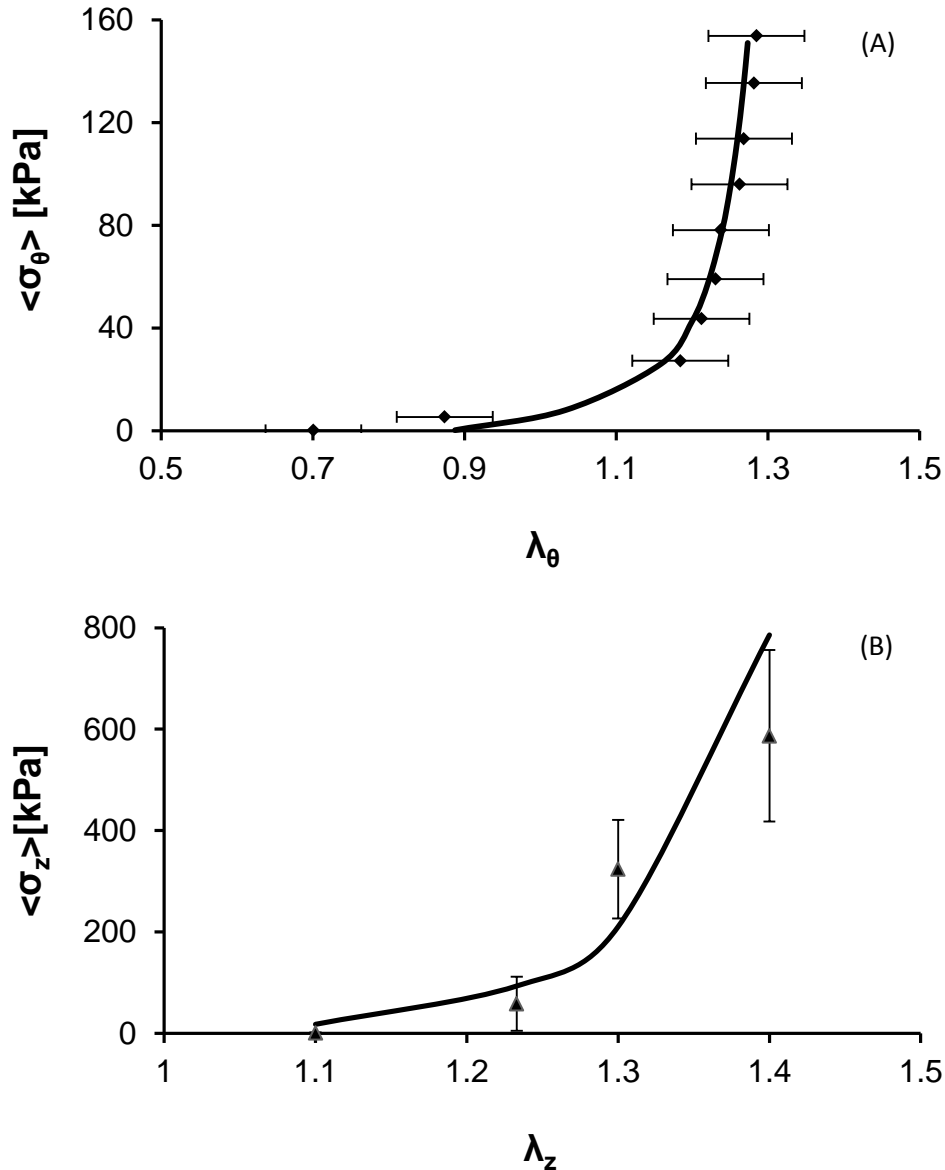


Figure 2.7. Representative comparison of experimental values (data points) and theoretical predictions (curves) for the (A) mean circumferential stress-circumferential stretch ratio and (B) mean axial stress-axial stretch ratio relationships of the porcine renal artery. Error bars denote standard deviation of experimental measurements ($n = 3$).

Wall stress distribution

The model was used to predict the circumferential stress across the arterial wall thickness (Figure 2.8). Under loading close to physiologic conditions ($\lambda_z = \lambda_{in-situ}$, $P \approx 100$ mmHg), the circumferential stress was maximal at the inner surface and decreased with

increasing radial position. The stress distribution was qualitatively reversed when $\lambda_z < \lambda_{in-situ}$, as circumferential stress increased with radial position.

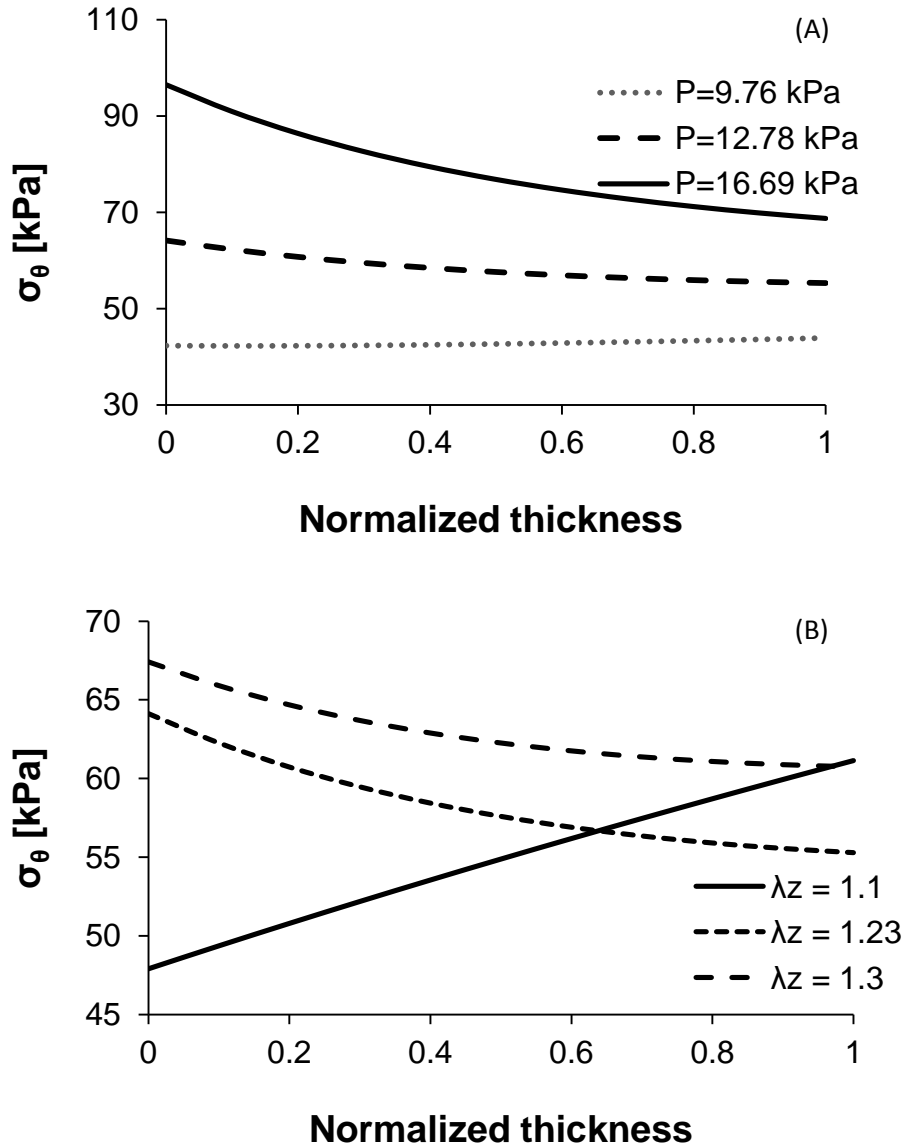


Figure 2.8. (A) Representative predictions of circumferential stress throughout the arterial wall at the in-situ axial stretch ratio (1.23) and pressures of 9.76 kPa, 12.78 kPa, and 16.69 kPa. (B) Representative predictions of circumferential stress distribution at fixed pressure (13.33 kPa) and axial stretch ratios of 1.1, 1.23, and 1.3. In both plots, the radial position has been normalized such that 0 and 1 refer to the inner and outer deformed radii, respectively.

2.5 DISCUSSION

The aim of this study was to quantify the passive mechanical response of the primary porcine renal artery and develop a mathematical model that facilitates calculation of arterial wall stresses and strains under physiologic loading. The obtained results can be sorted according their descriptive and predictive characteristics. The passive mechanical response is described in terms of the internal pressure-deformed diameter and internal pressure-axial force relationships at fixed arterial lengths. Moreover, data are processed to calculate parameters that describe a local linearized measure of the mechanical response, namely the pressure-diameter modulus in the neighborhood of physiologic loading conditions. A structure-motivated constitutive model of the renal artery was proposed and validated to allow solving boundary-value problems, the solutions of which predict arterial response and wall stress distribution under different loading scenarios.

A majority of the generated data on the renal artery are within range of published results for other porcine arteries. The opening angle which characterizes the zero-stress configuration of the renal artery was found to be $84.0 \pm 12.4^\circ$, which is similar to values reported for the porcine carotid ($84.7 \pm 9^\circ$) and left circumflex ($75 \pm 29^\circ$) arteries [55, 59]. Experimental results show a nonlinearity of the pressure-deformed diameter relationship, which is commonly observed and attributed to the non-linear mechanical response of elastin and gradually increased load-bearing of collagen fibers as they straighten out at higher pressures. The character of the pressure-axial force response and dependence on axial stretch ratio are in qualitative agreement with most of the published data on large conduit arteries.

Despite the general agreement with mechanical data on functionally similar vessels acquired ex-vivo, the pressure-deformed diameter curve of the primary renal artery does not exhibit the typical convex portion over the range of low pressures. This novel attribute of the passive response is possibly due to the low elastin content of the arterial wall ($12.6 \pm 0.05\%$), which is notably less than the 19% - 53% elastin content reported for the porcine carotid artery [59]. Alternatively, it is possible that the collagen fibers in this vessel have a less wavy unloaded configuration, and thus contribute to load-bearing even at low pressures.

The pressure-diameter modulus of the renal artery near physiologic loading conditions is 251.3 ± 133.5 kPa, which is significantly greater than the value reported for the same vessel in-vivo (24 ± 1 kPa) [71] but similar to ex-vivo measurements of the porcine abdominal aorta (219 ± 17 kPa) [72]. The discrepancy between Peterson's modulus in-vivo and ex-vivo might be due to the contribution of vascular tone in-vivo. Contraction of the vascular smooth muscle reduces the deformed diameter of the vessel and circumferential stretch ratio, which in turn decreases the structural stiffness due to the non-linearity of the mechanical response.

2.6 STUDY LIMITATIONS

The limitations of this study are associated with the introduced assumptions. The variation of collagen fiber orientation is only partially accounted for by the four fiber constitutive model, while there is in fact a continuous distribution of fiber orientations. Moreover, the proposed one-layered model assumes that the arterial wall composition and structure are uniform in the radial direction. More detailed assessment of arterial wall composition and structure may impact theoretical predictions of the stress-strain

relationships and attribute the mechanical response to individual load-bearing constituents.

Quantifying the passive mechanical properties is a requisite step to understanding the primary determinants of renal artery mechanical performance. Subsequent studies that probe the VSMC-mediated active mechanical response, the baroreceptor-mediated response to arterial pressure, and the endothelial-cell mediated response to shear, will together elucidate the renal artery mechanical response in conditions of health and disease. Additional histological studies could provide insight into the microstructural configuration of collagen within the arterial wall, and help explain the particular shape of the obtained pressure-deformed diameter response curves.

2.7 CONCLUSIONS

In both basic science and clinical research, including disease diagnosis, cellular signal mechanotransduction, and vascular tissue engineering, it is advantageous to understand the arterial mechanical response under various loading conditions and states of health. Accordingly, one of the major objectives of vascular biomechanics is the determination of the constitutive equations that describe tissue mechanical properties and allow formulating and solving boundary value problems with predictive power. In the present study, bi-axial mechanical testing coupled with structure-motivated constitutive modeling enabled quantification of the passive mechanical response of the primary porcine renal artery, including assessment of the stresses experienced by vascular cells within the arterial wall. Quantifying the passive mechanical response of renal arteries is a necessary step to understanding normal and aberrant mechanical performance, and may

provide insight into the genesis and progression of certain forms of renal vascular disease.

2.8 STUDY TRANSITION

The uniform circumferential stress distribution across the primary renal arterial wall under physiological loading conditions exhibits function of extracellular matrix (ECM) to ensure optimal performance of the vascular smooth muscle cells (VSMCs). VSMCs contraction plays a significant role in overall mechanical behavior and potentially exerts contractile forces in more than one principal direction within the arterial wall. Being a muscular-type vessel, it is reasonable to expect that renal arteries manifest a more sophisticated vasomotor response compared to elastic-type conduit vessels. To this end, we next investigate the biaxial effects of vascular smooth muscle contraction on the mechanical response of primary renal artery and propose an analytical form accounting for contribution of biaxial VSMCs contraction to better understand the active stress-stretch relationships within the muscular arterial wall.

CHAPTER 3

BIAXIAL VASOACTIVITY OF PRIMARY RENAL ARTERIES

3.1 ABSTRACT

This study verified the development of active circumferential and axial stresses in the porcine primary renal arterial wall over a range of physiological pressure when the vascular smooth muscle cells are stimulated to contract by analyzing the experimental data from the in-vitro inflation-extension test. The results obtained showed that active axial stress-stretch relationship was non-monotonic while active circumferential stress increased almost linearly with circumferential stretch ratio. The parameters associated with the analytical form incorporating both the axial and circumferential stretches fit experimental data and indicate deformed configurations where active stress is maximal and minimal.

3.2 INTRODUCTION

Renal arterial disease has increasingly gained recognition as a risk factor for cardiovascular morbidity and mortality. Hypertension is a major risk factor for the development of renovascular disease. As a typical muscular conduit artery in which the media is mostly occupied with vascular smooth muscle cells (VSMCs), primary renal arteries are capable of regulating the local blood flow through modulating VSMCs contractile state to restore baseline values of flow-induced shear stress imparted on the

endothelial cells. Moreover, it has been shown that vasoconstriction can reduce the transmural distribution of stress induced by the elevation of blood pressure. Despite the critical vasomotor function of the renal artery, few biomechanical studies have focused on the biaxial active stress-strain relationships of VSMCs contraction. Mechanosensitive VSMCs are able to tune the vessel tone via contraction concurrently mediated by flow-induced shear stress at the endothelium, pressure-induced medial stretch, and baroreceptor signaling from the sympathetic nervous system [33, 35, 50, 73-76]. It was also deduced from biochemical studies that VSMCs contractile states are affected by level of neurotransmitters, hormones and paracrine [77]. In this study, we propose that active stresses induced by the alteration in the vascular smooth muscle tone are bi-axially dependent on the strains.

Numerous biomechanical investigations have been conducted to identify and formulate active stress-strain relationship produced by VSMCs contraction. The magnitude and functional dependence of the active stresses on the strain measures were often postulated based on the basis of histology, biophysics of VSMC contraction [78, 79]. Dobrin firstly suggested that the active circumferential stress was a function of length-tension and tension-dose relationship obtained from the isometric contraction test [80, 81]. These active stress-strain relationships were then investigated and fitted with analytical forms within the framework of continuum mechanics [82], within which various constitutive models were proposed to quantify the contribution of VSMCs contraction on the mechanical response of vascular tissues [47, 52, 83-87]. Both active circumferential and axial stresses were assumed to be as a function of circumferential stretch ratio since large portion of VSMCs are circumferentially oriented within the

vascular wall [88]. However, some studies showed that active axial stress was solely dependent on axial stretch ratio [89]. Notwithstanding great advancements of theoretical research in modeling active responses of VSMCs, there is still need to clarify the correlation of active stresses and corresponding stretch ratios.

Experimental quantification of the active stresses is mostly assessed by processing the in-vitro recorded deviation in deformed outer diameter and axial force of a tubular arterial specimen inflated by an internal pressure at fixed axial stretch ratio [90-92]. The effect of VSMCs contraction on strain distribution across the vessel wall thickness was evaluated by measuring the opening angles of arterial sector due to various doses of vasoconstrictor or vasodilator, from which can be implied that alteration of VSMCs basal tone were able to homogenize intramural strain within the arterial wall under physiological loads [93]. Although extensive studies have been carried out to experimentally probe active vascular mechanical responses, few biomechanical investigations have focused on the active bi-axial mechanical behaviors of primary renal arteries.

In vivo axial stretch of arterial tissue plays a key role in maintaining vessel structural stability via maintaining axial force independent of pulsatile blood pressure [94]. Some researches illustrated that the VSMCs basal tone was affected by the degree of longitudinal stretches [95, 96]. Despite the significant physiological function of in vivo axial stretch, little work has been done to quantify the effect of VSMCs basal tone on in vivo axial stretch.

The aim of the present study is to experimentally assess the active stress-stretch relationships within the renal arterial wall and propose analytical expressions accounting

for biaxial VSMCs contraction. Integration of analytical forms modeling biaxial VSMCs contraction and structure-motivated constitutive models will facilitate formulating and solving boundary value problem of renovascular biomechanics.

3.3 MATERIALS AND METHODS

Theoretical framework

The recorded mechanical responses were manifested as the deformed outer diameter (d_o), the measured axial force (f_M) at various imposed axial stretch ratios (λ_z) within a reasonable range of luminal pressure (P). Based on the deformed outer radius ($r_o = d_o/2$) and assumption of vessel incompressibility, the deformed inner radius (r_i) is calculated as follows:

$$r_i = \sqrt{r_o^2 - \frac{A}{\pi\lambda_z}} \quad (3.1)$$

The arterial tissue is assumed to be an orthotropic incompressible elastic material, with axes of orthotropic in the radial (r), circumferential (θ) and axial (z) directions. The total Cauchy stress in the arterial wall is assumed as a sum of a passive stress with components $\sigma_r^p, \sigma_\theta^p, \sigma_z^p$ and an active stress that has components σ_θ^a and σ_z^a in the circumferential and axial direction. The passive stress is derived from the strain-energy density function (SEF) W which is a function of the principal Green strains $E_i = \frac{1}{2}(\lambda_i^2 - 1), i = r, \theta, z$, where λ_i are the corresponding principal stretches. Because of condition of material incompressibility the components of the Green strain tensor are not independent but satisfy the condition $(2E_r + 1)(2E_\theta + 1)(2E_z + 1) = 1$. Using this equation E_r can be eliminated as argument of the SEF W , I.e. $W = (E_\theta, E_z)$. Following

the approach for derivation of the passive constitutive relations of the arterial tissue when the SMCs are stimulated to contract

$$\sigma_{\theta}^c = \sigma_r^p + \lambda_{\theta} \frac{\partial W}{\partial \lambda_{\theta}} + \sigma_{\theta}^a, \quad \sigma_z^c = \sigma_z^p + \lambda_z \frac{\partial W}{\partial \lambda_z} + \sigma_z^a, \quad (3.2)$$

Due to existence of residual strains in the unloaded ring tubular segment and the synergistic effects of the active stress, the stress and strain distribution across the arterial wall is close to uniform [97]. Therefore the mean values are able to describe the stress and strain state. Hereafter the stresses and strains represent the mean values.

Consider two deformed states: one when the artery is fully relaxed (passive response), and another when the smooth muscle is stimulated to produce the so-called isometric contraction. In the latter case the artery experiences the same circumferential stretch and same axial stretch as in the case of passive response but is inflated by different pressure. The active axial stress can be calculated by subtracting the stress in the arterial wall when the smooth muscle cells are maximally relaxed from the total stress when the smooth muscle cells are stimulated to contract under isometric contraction.

$$\sigma_{\theta}^a = \sigma_{\theta}^{ic} - \sigma_{\theta}^p - \sigma_r^p, \quad \sigma_z^a = \sigma_z^{ic} - \sigma_z^p - \sigma_r^p, \quad (3.3)$$

The subscripts ic stands for the case of isometric contracted state.

The mean values of wall stresses can be calculated directly from the experimental data as follow [98]:

$$\bar{\sigma}_r = -P \frac{r_i}{r_o + r_i}, \quad \bar{\sigma}_{\theta} = -P \frac{r_i}{r_o - r_i}, \quad \bar{\sigma}_z = \frac{f}{\pi(r_o^2 - r_i^2)} \quad (3.4)$$

Where r_o is the deformed outer radius.

$$\sigma_{\theta}^a = r_i \left(\frac{1}{r_o - r_i} + \frac{1}{r_i + r_o} \right) (P_{ic} - P_p), \quad \sigma_z^a = \frac{F_{ic} - F_{wr}}{A} + \frac{r_i(P_{ic} - P_p)}{r_i + r_o} \quad (3.5)$$

Where P_p and P_{ic} refer to the pressure in the case of passive response and isometric contraction, respectively.

On the other hand, the mean stretch ratios in the circumferential and axial directions are

$$\lambda_{\theta} = \frac{2\pi(r_o+r_i)}{C_o+C_i}, \quad \lambda_z = \frac{l}{L} \quad (3.6)$$

l is distance between marks in the current deformed state and L the distance between the same points in the traction free state when the SMCs are fully relaxed. Thus after processing the experimental pressure-diameter and extension-force data in the case passive response and response under isometric contraction, it is possible to obtain a set of experimental active stress vs. principal stretches. The analytical form of the phenomenological constitute relations $\sigma_{\theta}^a = \sigma_{\theta}^a(\lambda_{\theta}, \lambda_z)$ and $\sigma_z^a = \sigma_z^a(\lambda_{\theta}, \lambda_z)$ are determined on the basis of certain general and experimental-based characteristics of the active response; the model parameters involved in these relations are quantified to yield the best fit predictions of experimental stress given by Eqs. () from the condition of minimization of the objective functions

$$\Omega_{\alpha} = \sum_{n=1}^N \left(\frac{\sigma_{\alpha}^{a(teor)} - \sigma_{\alpha}^{a(exp)}}{\sigma_{\alpha}^{a(exp)}} \right)_n^2, \quad \alpha = \theta, z \quad (3.7)$$

where $n=1, 2, \dots, N$ is the number of the experimental states.

The passive constitutive modeling follows the slightly modified commonly accepted methodology for quantification of strain energy function W on the basis of experimental data from inflation-extension mechanical tests [99]. We adopted a previously proposed four fiber model for the passive mechanical properties according which the strain energy function is sought in the form

$$W = c (I_1 - 3) + \sum_{k=1,2,3,4} \frac{b_{1k}}{2b_{2k}} \left\{ \exp \left[b_{2k} (\lambda_k^2 - 1)^2 \right] - 1 \right\} \quad (3.8)$$

The first term accounts for contribution of the elastin. c is a material constant, and $I_1 = \lambda_\theta^2 + \lambda_z^2 + (\lambda_\theta \lambda_z)^{-2}$ is the first invariant of the Cauchy-Green strain tensor. The second term includes the contribution of four families of collagen fibers. Subscript k denotes a family of collagen fibers oriented at a mean angle of α_k with respect to the longitudinal vessel axis; b_{1k} , and b_{2k} are material constants; and $\lambda_k = \sqrt{\lambda_\theta^2 \sin^2 \alpha_k + \lambda_z^2 \cos^2 \alpha_k}$ is the stretch ratio of each family of collagen fibers due to deformation. The material constants c , b_{1k} , b_{2k} are determined by the minimization of the following objective function

$$\Omega_p = \sum_{n=1}^N \left(\frac{\sigma_{\theta n}^T - \sigma_{\theta n}^E}{\sigma_{\theta n}^E} \right)^2 + \sum_{n=1}^N \left(\frac{\sigma_{z n}^T - \sigma_{z n}^E}{\sigma_{z n}^E} \right)^2 \quad (3.9)$$

The superscript E and T refer to the experimentally recorded and theoretically calculated values of the circumferential and axial stresses as follows

$$\sigma_\theta^E = P_p \frac{r_i}{r_o - r_i}, \quad \sigma_z^E = \frac{f_p}{\pi (r_o^2 - r_i^2)} \quad (3.10)$$

$$\sigma_\theta^T = \lambda_\theta \frac{\partial W}{\partial \lambda_\theta} - P_p \frac{r_i}{r_o + r_i}, \quad \sigma_z^T = \lambda_z \frac{\partial W}{\partial \lambda_z} - P_p \frac{r_i}{r_o + r_i}. \quad (3.11)$$

Mechanical testing

In our study, experimental protocol of quantifying the active axial stress in mouse aorta was followed with slight modifications [89]. 5 sets of primary renal arteries were excised from freshly harvested adult porcine (7 month old) kidneys. Preliminary studies quantifying the effect of VSMCs basal tone on the in situ axial stretch had been done prior to mechanical testing. Before dissecting the arteries between aorta and kidneys, two

dots of tissue marking dye were applied between proximal and distal sites of the sample and distance between these dots was measured using digital caliper. Samples were then removed from the organs and the unloaded length with VSMCs basal tone was measured. Afterwards, it was placed on the petri dish filled with 10^{-5} M sodium nitroprusside diluted with Krebs-Heisenleit solution and equilibrated for 30 min, distance between dots was measured again to get fully-relaxed un-loaded length. In-situ axial stretch ratio was calculated as the ratio of in-situ length to un-loaded length of sample ($\lambda_{in,situ} = L_{in-situ}/L_{no\ load}$).

Once primary renal arteries were harvested and rinsed with phosphate buffer solution (PBS), they were then cannulated and mounted to a chambered mechanical testing system configured for inflation-extension experiments (Bose BioDynamic 5270). Arterial samples were submerged in and perfused with continuously aerated (95% O₂ + 5%CO₂) Krebs-Henseleit solution at 37° and pH of 7.4. The active mechanical response was assessed under maximal VSMC contractile state which was induced by adding to the circulating medium with 10^{-5} M epinephrine and allowed the artery to acclimate for 15 min. Following stimulation, arterial samples were mechanically preconditioned at an axial stretch ratio of 1.1 with 5 cycles of pressurization (pressure range of 20-200 mmHg, pressure change rate of 1.5 mmHg/s). Samples were then subjected to a quasi-static pressure increase (20 – 200 mmHg, 20 mmHg steps) at three levels of axial stretch span $\lambda_{in,situ}$ with the vessel outer diameter and axial force monitored at each experimental state via integrated system components and software (Wintest and Labview). The passive mechanical response was assessed under a fully relaxed VSMCs state by changing the circulating medium from 10^{-5} M epinephrine to 10^{-5} M sodium nitroprusside (SNP)

solution and acclimated for 15 min. Vessels in the fully relaxed VSMCs state were mechanically preconditioned and subjected to extension-inflation tests as described above.

Upon the completion of mechanical testing, ring segments (1 mm width) were cut from the central part of each artery, allowing equilibration for 30 min in Krebs-Henseleit solution. The opened-up sector was quantified via analytical microscopy and considered as the stress-free configuration of the arterial wall.

The inner (L_i) and outer (L_o) arc lengths as well as thicknesses (H) of sectors from each arterial sample were measured and used to calculate the opening angle (Φ_o) and cross-sectional area (A) of the circular sector as follows:

$$\Phi_o = \pi - \frac{L_o - L_i}{2H} \quad \text{and} \quad A = \frac{H(L_o + L_i)}{2} \quad (3.3)$$

3.4 RESULTS

Morphometric measurements of the porcine primary renal arteries in the stress-free configuration obtained via image analysis are shown in Table 3.1. The average values obtained among five vessels for inner L_i and outer L_o arc lengths as well as the thickness were 10.63 ± 1.8 mm, 15.17 ± 2.96 mm, and 1.13 ± 0.14 mm, respectively. Opening angle of each idealized sector was calculated based on these measurements. Calculated values of opening angle for all the samples were $66.32 \pm 23.7^\circ$. Preliminary studies showed that the in situ axial stretch in the VSMCs fully relaxed state decreased by 5% compared to that of the artery with VSMCs basal tone.

Table 3.1. The vessel geometry in the stress-free configuration for each arterial test segment. L_i , L_o , H , Φ are the outer arc length, inner arc length, opening angle, wall thickness, respectively.

Sample	Outer arc-length(L_o) [mm]	Inner arc-length(L_i) [mm]	Thickness(H) [mm]	$\lambda_{z, \text{in-situ}}$
1	15.53	11.44	0.98	1.23
2	11.33	7.68	1.17	1.20
3	14.64	11.04	1.09	1.30
4	19.60	12.49	1.36	1.46
5	14.72	10.49	1.07	1.32
Average	15.17	10.63	1.13	1.30
SD	2.96	1.80	0.14	0.10

Representative pressure – deformed outer diameter and axial force-pressure relationships span the in situ axial stretch ratio in both the fully relaxed and maximally contracted VSMCs states of the primary renal artery exhibit high degree of nonlinearity (Figure 3.1). Peterson’s modulus which is a reasonable measure of arterial stiffness (E_p) was calculated for each vessel at physiological loading conditions ($P = 13.33$ kPa, $\lambda_z = \lambda_{\text{in-situ}}$), using equations as follows:

$$E_p = \frac{D\Delta P}{\Delta D} \quad (3.4)$$

Obtained results showed that average values of elastic moduli of arterial wall under both the maximally contracted and fully relaxed VSMCs were 192.64 ± 15.26 kPa and 249.13 ± 152.26 kPa. At pressure of 100 mmHg, there was significant reduction in deformed outer diameter of primary renal artery when VSMCs were maximally contracted compared with that when VSMCs were fully relaxed at various axial stretches. Conversely, maximally contracted VSMCs resulted in an increase in axial force of primary renal artery versus that when VSMCs were fully relaxed (Figure 3.2).

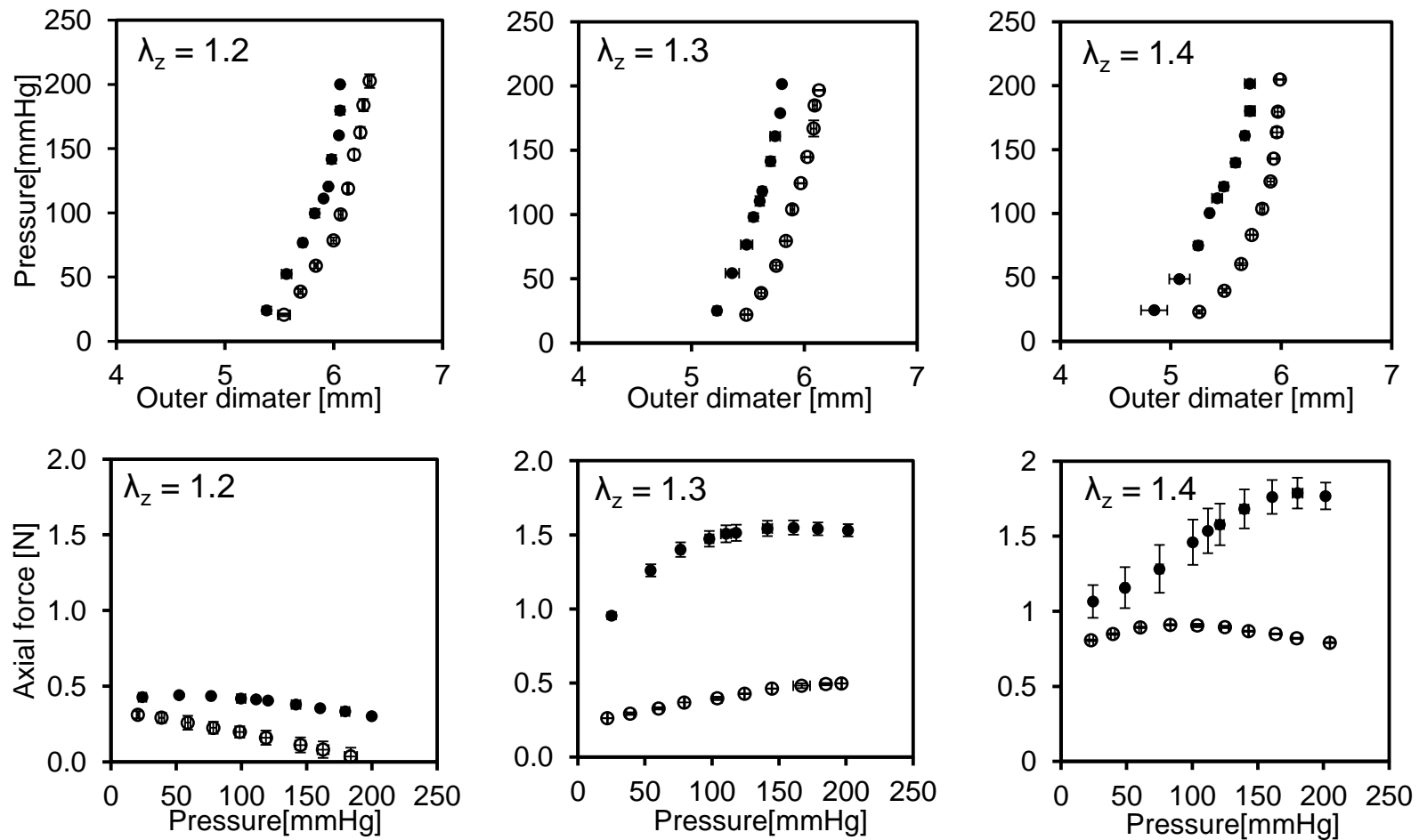


Figure 3.1. Representative pressure-deformed outer diameter and axial wall force-pressure relationships of the porcine primary renal artery at three levels of axial stretch ($\lambda_z = 1.2, 1.3$, or 1.4) and at either maximally contracted (\bullet) or fully relaxed (\circ) smooth muscle states. Error bars denote standard deviation of three repeat measurements at each experimental state.

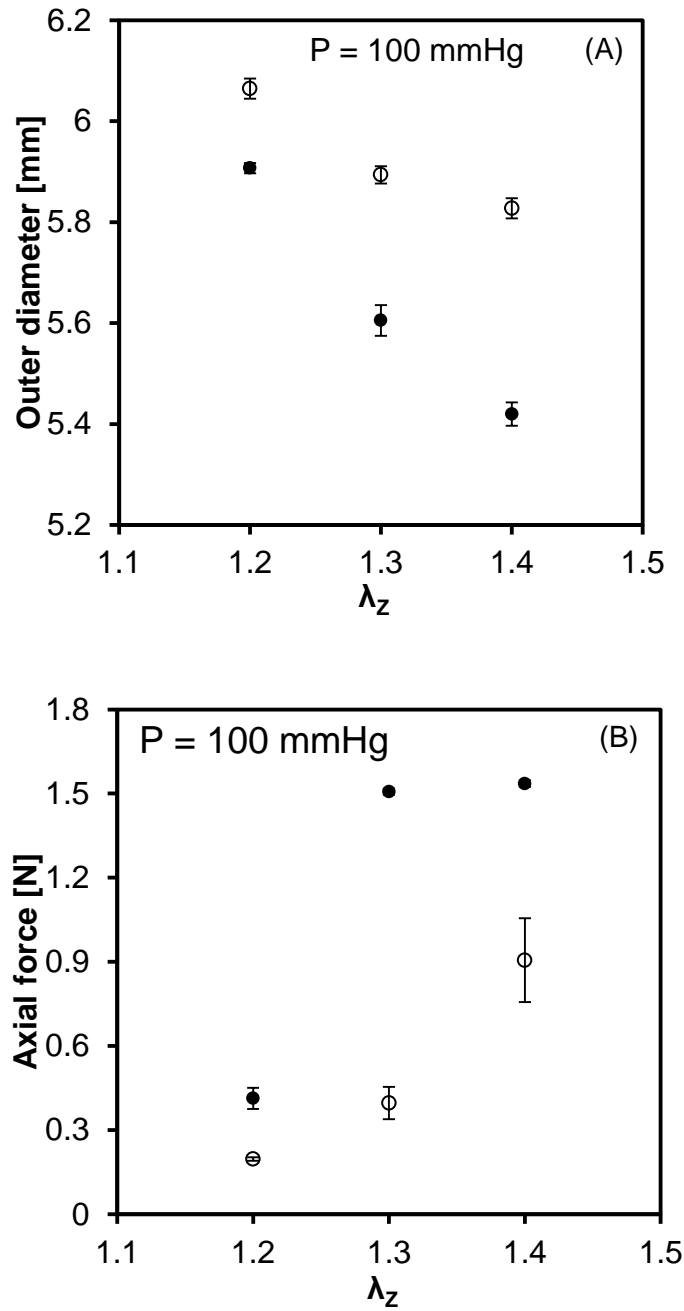


Figure 3.2. Representative deformed outer diameter-axial stretch and axial wall force-axial stretch relationships of the porcine primary renal artery at three levels of axial stretch ($\lambda_z = 1.2, 1.3, \text{ or } 1.4$) and at either maximally contracted (•) or fully relaxed (◊) smooth muscle cells states. Error bars denote standard deviation of three repeat measurements at each experimental state.

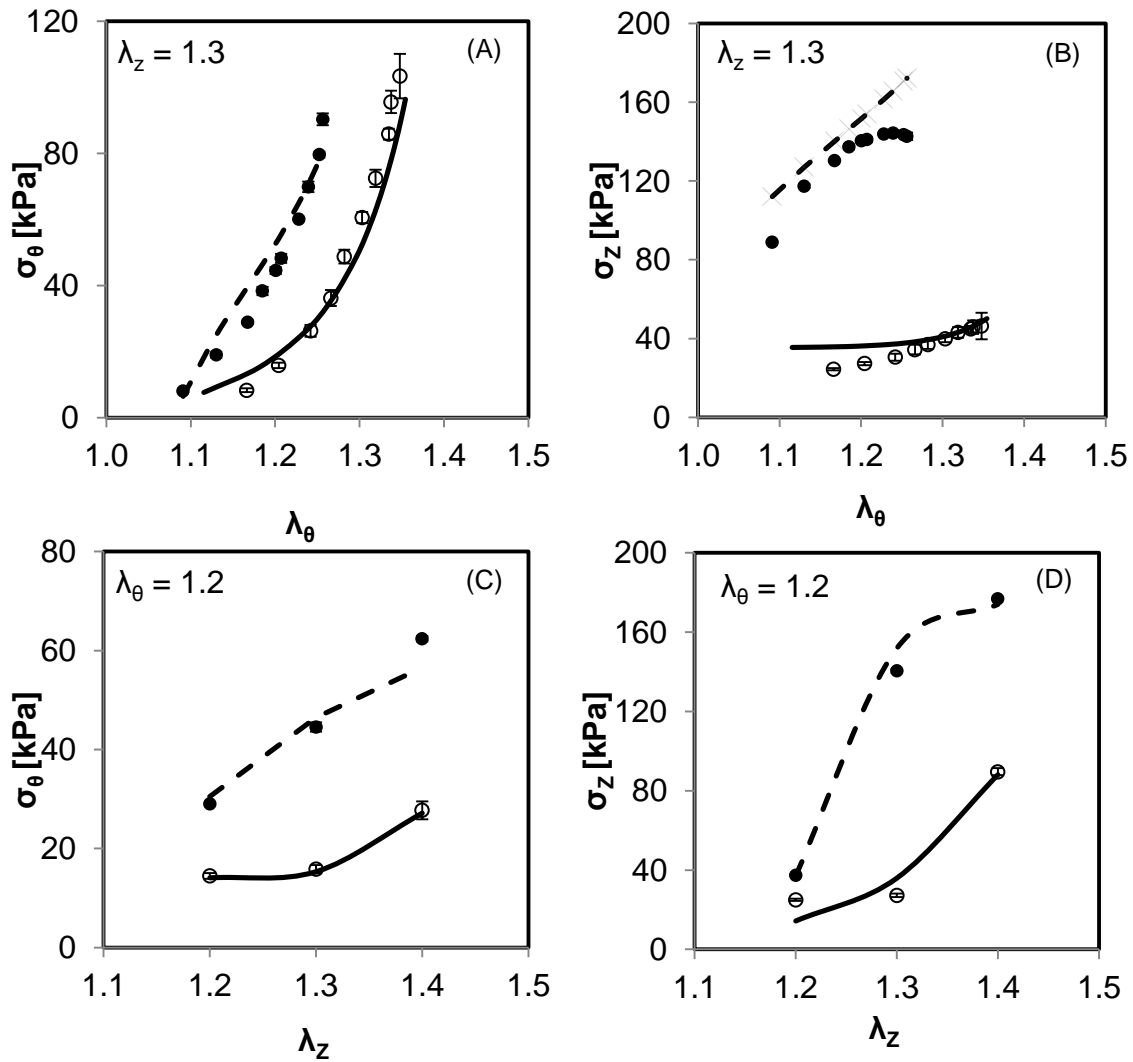


Figure 3.3. Representative comparison of experimental values and theoretical predictions of circumferential stress-circumferential stretch (A), axial stress-circumferential stretch (B), circumferential stress-axial stretch (C) and axial stress-axial stretch (D) relationships of the porcine primary renal artery at either maximally contracted (\bullet) or fully relaxed (\circ) smooth muscle cells states. Error bars denote standard deviation of three repeat measurements at each experimental state. Blue circle represent the physiological states.

At the in situ axial stretch ratio, total circumferential stress - circumferential stretch curve of primary renal artery shifted leftwards while total axial stress - circumferential stretch curve shifted upwards when VSMCs were maximally contracted. Meanwhile, at the same circumferential stretch ratio, maximally contracted VSMCs

resulted in increase in total circumferential and axial stresses of primary renal artery at various axial stretch ratios (Figure 3.3). Active circumferential and axial stresses were derived after having processed all experimental data. The active axial stress – stretch displays a non-monotonic relationship while active circumferential stress increased linearly with circumferential stretch ratio (Figure 3.4). Numerical surface fitting algorithm was used to identify the following analytical expressions for the derived active stresses as a function of stretch ratios

$$\sigma_{\theta}^a = \alpha_1(\alpha_2\lambda_z - 1) \lambda_{\theta} \left[1 - \left(\frac{\lambda_{\theta,max} - \lambda_{\theta}}{\lambda_{\theta,max} - \lambda_{\theta,0}} \right)^2 \right] \quad (3.5)$$

$$\sigma_z^a = \beta_1(\beta_2\lambda_{\theta} - 1) \lambda_z \left[1 - \left(\frac{\lambda_{z,max} - \lambda_z}{\lambda_{z,max} - \lambda_{z,0}} \right)^2 \right] \quad (3.6)$$

where $\lambda_{\theta,max}$ and $\lambda_{z,max}$ are the stretch ratios at which the active circumferential and axial stresses are maximal; $\lambda_{\theta,0}$ and $\lambda_{z,0}$ are the stretch ratios below which no active stresses are developed; α_1 , α_2 , β_1 and β_2 are material constants. Experimentally derived active stress-stretch data was fitted with parameters $\alpha_1 = 308$ kPa, $\beta_1 = 235.4$ kPa, $\lambda_{\theta,max} = 1.98$ and $\lambda_{z,max} = 1.32$, $\lambda_{\theta,0} = 1.08$ and $\lambda_{z,0} = 1.15$. The proposed analytical expressions for active stresses correlate well with experimental data of the active response (Table 3.2 and Figure 3.4).

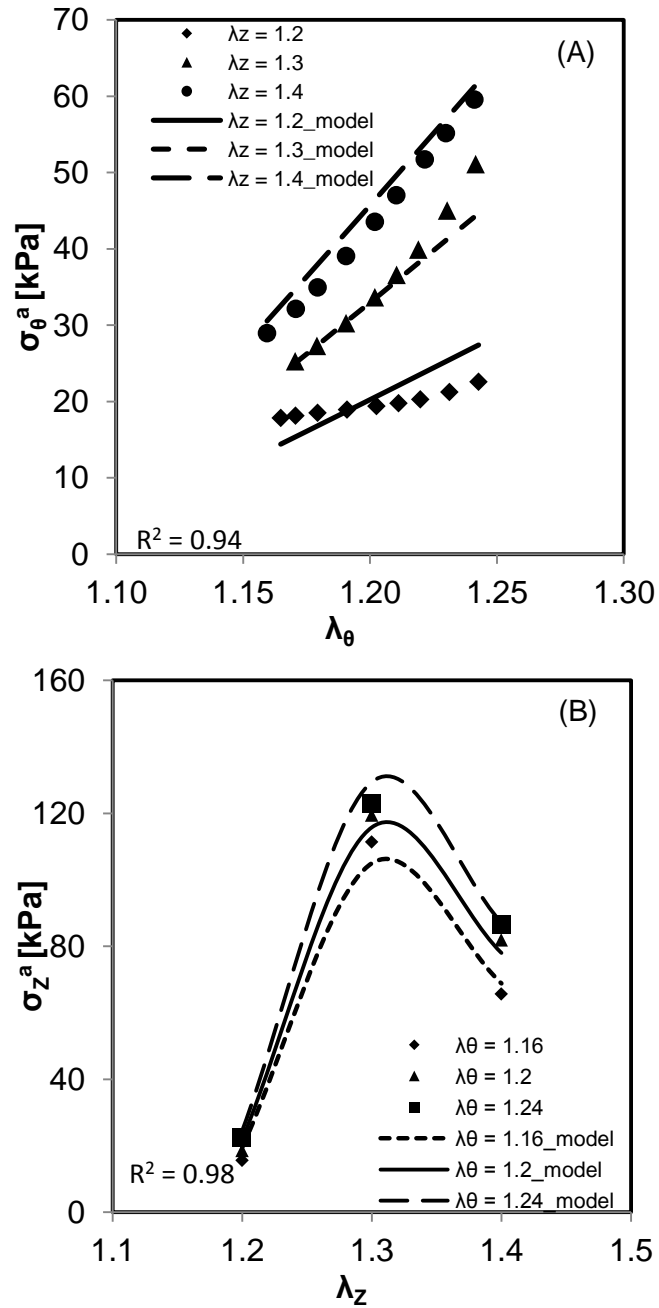


Figure 3.4. Representative comparison of experimental values (data points) and theoretical predictions (curves) for both the active circumferential (A) and axial (B) stress-stretch ratio of the porcine renal artery

Table 3.2. Parameters of the proposed analytical expression fitting the active circumferential and axial stresses of the porcine primary renal artery.

Sample	α_1 [kPa]	α_2	$\lambda_{0,max}$	$\lambda_{0,0}$	R^2	β_1 [kPa]	β_2	$\lambda_{z,max}$	$\lambda_{z,0}$	R^2
1	295	0.95	1.56	0.68	0.99	98.00	2.10	1.27	1.10	0.98
2	295	0.99	1.42	0.97	0.79	175.50	1.14	1.26	1.08	0.99
3	308	1.04	1.98	1.08	0.92	235.40	1.15	1.32	1.15	0.99
4	295	0.83	1.61	0.67	0.86	42.75	2.10	1.46	1.33	0.93
5	298	0.83	1.25	1.08	0.76	80.10	1.40	1.34	1.28	0.98
Average	298.24	0.93	1.56	0.90	0.86	126.35	1.58	1.33	1.19	0.97
SD	5.72	0.09	0.27	0.21	0.09	77.84	0.49	0.08	0.11	0.02

3.5 DISCUSSION

The aim of this study was to quantify the active mechanical response of the primary porcine renal artery and develop an analytical expression that is able to model the derived biaxial active stress-stretch relationships. The mechanical response of primary renal arteries is expressed in terms of the deformed outer diameter-internal pressure and axial force-internal pressure relationships at multiple longitudinal extensions. There was a significant decrease in the deformed outer diameter over the entire measurement range when VSMCs were maximally contracted when the axial stretch $< \lambda_{in-situ}$. For the axial force-pressure relationship, the axial force increased significantly from 0 to 200 mmHg under maximal VSMCs contraction when the axial stretch $< \lambda_{in-situ}$.

The characteristics of pressure-deformed outer diameter and axial force-pressure response both in maximally contracted and fully relaxed VSMCs states are in agreement with other published data on large muscular arteries [91, 100]. The deformed outer diameter of the vessel at certain pressure was reduced due to the exerted contractile forces of the vascular smooth muscle cells, which in advance increase the structural stiffness because of the nonlinear mechanical responses of the vessel by comparing the elastic moduli between maximally contracted and fully relaxed VSMCs. Contractile states affect arterial stiffness which manifested as a factor of progression of chronic kidney disease and end-stage renal disease [101].

The dependence of the active stresses on both circumferential and axial stretches might have several plausible explanations. VSMCs could be axially-, circumferentially- and/or helically-oriented within the arterial wall. It is possible that the contraction of the vascular smooth muscle cells causes a reorientation of the collagen fibers, such that the axial and circumferential stress borne by the extracellular matrix in the contracted and relaxed vessel are different [89]. It was shown that axial active mechanical response was attributed to the multi-axial VSM contraction and arrangement [102]. Detailed histological evaluation of the primary renal arterial wall under applied loads would provide further insight into the factors that mediate the active response.

Due to incompressibility of arterial wall, arterial longitudinal length was shortened as VSMCs mostly aligning in the circumferential direction relaxed and expanded. Therefore, the in situ axial stretch was increased in the fully-relaxed VSMCs state compared to that of VSMCs basal tone. Moreover, parameters fitted into the analytical form for deriving active stresses showed that the sensitivity of VSMCs

contractility varied with degree of extension. This assumption was indirectly supported by the findings that VSMCs contractility of cerebral arteries was pretty sensitive to its axial stretch [95]. There is a need to further quantify the axial mechanochemical response of the arterial tissues.

The degree of VSMCs contractile states was proposed to be highly associated with the early response of vascular remodeling induced by abnormal alteration in hemodynamic loads, aiming to restore the baseline values of intramural stresses [44, 47, 82, 87]. Perturbation of local stresses and strains may alter the cell phenotype, triggering a chain of events such as cell proliferation, migration, apoptosis or necrosis as well as synthesize and degradation of extracellular matrix. Given the attribution of maladaptive remodeling to CVD, it is important to comprehend the fundamental mechanism of arterial mechanotransduction in critical vasculature system [68-70].

3.6 STUDY LIMITATIONS

The level of VSMCs activation is only partially accounted for by circumferential and axial stretch ratios at VSMCs maximally contractile states while in actuality there is sigmoidal relationship between smooth muscle activation and agonist concentration [88]. Therefore, future experimental studies of renal artery should take dose response effect into account. Secondly, the proposed analytical forms did not incorporate the mass fraction of structural constituents within the arterial wall. There is further need to construct structure-based analytical forms incorporating morphological quantification of arterial wall.

3.7 CONCLUSIONS

In conclusion, biomechanical response of porcine primary renal artery accounting for VSMCs contractile states was probed by biaxial mechanical testing. The derived active circumferential and axial stresses were fitted with proposed analytical expressions. The results revealed that active circumferential stress monotonically increased with circumferential stretch while active axial stress-strain relationship is non-monotonic. The proposed analytical expressions coupled with structure-based constitutive models is a requisite step for modeling the growth and remodeling of vascular tissues, facilitating formulating and solving specific boundary value problems of vascular maladaptation.

3.8 STUDY TRANSITION

The integrated theoretical-experimental study of passive and active mechanical behaviors of porcine primary renal artery provides significant mechanical information for cardiovascular mechanobiology. The common surgical procedures for treating cardiovascular disease are implantation of autologous coronary artery vascular grafts. To this end, we next characterize the passive mechanical behaviors of various candidates for coronary artery end-to-end grafts using established experimental methodology and theoretical modeling, evaluating their suitability for coronary artery grafts.

CHAPTER 4

MECHANICAL ANALYSIS OF AUTOLOGOUS CORONARY ARTERY GRAFTS

4.1 ABSTRACT

This study provided a methodology to evaluate the mechanical equivalency of various autologous vascular grafts for an end-to-end anastomosis to a coronary artery. Passive mechanical response of porcine coronary artery, internal thoracic artery, radial artery, great and lateral saphenous veins were quantified via inflation-extension tests which probes pressure-diameter and axial force-pressure relationships at various degree of longitudinal extension. Experimental data were then used to parameterize and validate a structure-motivated constitutive model of the vascular wall. The normalized difference in structural and mechanical properties between the host artery and graft vessel were compared. Taken together, experimental and theoretical comparisons in the structural and mechanical properties of various graft vessels will provide a framework to select a mechanics-matched end-to-end autologous coronary artery graft.

4.2 INTRODUCTION

Implantation of autologous vascular grafts is one of the surgical procedures for myocardial and peripheral revascularization [103, 104]. 395,000 coronary artery (CA) grafting surgeries were performed in 2013, an operation for treating obstructive coronary

disease in which autologous tissue source is used to bypass or replace compromised segment [105]. Saphenous vein graft (SVG) with advantage of similar size and ease of access was firstly and is still used for myocardial reconstruction. Significant disadvantages of SVG are its late degeneration manifested as diffuse intimal thickening as well as redundant circulation and high failure rates [18]. Internal thoracic arteries (ITA) with lower postoperative occlusion rates are proven to have long-term clinical superiority over SVG [15, 16, 106-108]. With the introduction of antispastic drugs, the use of radial artery (RA) as an alternative conduit with good early and intermediate-term outcomes has dramatically increased during the last decade [14, 18, 109-112].

Morphological and microstructural properties of autologous vascular grafts are quite different from that of coronary artery, accounting for the differences in the success rates. The ITA was observed with elastomuscular microstructure in which a transition of elasticity within the media exists from proximal to distal segments, whereas SVG is long large-caliber peripheral vein of which inner media and adventitia are comprised of distinct longitudinal bundle of smooth muscle cells [108, 113]. RA as a muscular medium-size artery with large portion of smooth muscle cells reside in the media does not behave like elastic large artery [112, 114, 115]. There is clear correlation between microstructure and mechanical behavior of vascular grafts. However, little attention has been accorded the individual mechanical contribution of structural components to the macroscopic mechanical response of various vascular grafts.

Although extraordinary progress in vascular grafting strategies was made in the last few decades, graft failure remains a major problem in clinical medicine. The underlying causes of vascular graft failure include early proximal intimal hyperplasia and

subsequent atherosclerosis which restrict the lumen size and impede the blood flow [14, 109, 110, 116-120]. Compliance incongruities in terms of discrepancy of the circumferential pulsatile deformation between the graft and host artery is considered as one of the underlying causes of graft failure. For a cylindrical tube inflated by an internal pressure, compliance is a measure of overall mechanical response of tube by associating the normalized increase in tube diameter with the increase in pressure within a physiological range. An inverse proportional relationship between graft patency and compliance mismatch was reported in previous work [121-123]. Mechanical constraints on the deformation of the host artery and graft at the anastomotic sites may alter their inner radii and correspondingly change the blood flow pattern, leading to abnormal low wall shear stress on the endothelial cells [124-126]. Meanwhile, the degree of longitudinal extension of graft may affect its mechanical performance as well as that of the attached target artery [127]. Therefore, it is necessary to comprehend the impact of orthogonal compatibility of grafted vessel.

When vascular conduit is grafted under the new hemodynamic conditions, its local mechanical environment at the anastomosis is disturbed. The deviation between its homeostatic and grafted stress states may trigger adaptive remodeling in terms of smooth muscle cell proliferation and synthesis of extracellular matrix. These events alter vascular wall thickness and lumen diameter so as to restore the baseline values of mean circumferential and shear stresses and in turn create a thermodynamically stenosis or occlusion [50, 121, 128-136]. Quantification of stress distribution of grafts under various hemodynamic loads is important for us to understand mechanism of mechanotransduction and etiology of failure.

In the present work we investigated the mechanical properties of the CA, RA, ITA and great saphenous vein (GSV) and lateral saphenous vein (LSV) via biaxial mechanical testing and structure-motivated constitutive modeling. We assessed and compared the averaged vascular wall stresses, compliance and deformed inner radii between candidate of graft vessels and CA under grafted loading conditions. Results from this study will serve as a basis for optimal selection of end-to-end coronary artery graft.

4.3 MATERIALS AND METHODS

Native Vessel procurement

All tissue handling protocols were approved by the Institutional Animal Care and Use Committee at the University of South Carolina. Porcine heart, leg and arm were purchased from a local slaughterhouse immediately after sacrifice of adult animals (60-70 kg) and stored in ice for transport to the laboratory. Upon organs arrival, CA, SV, RA and ITA were excised from the surrounding tissue, washed in phosphate buffered saline (PBS), dissected free of perivascular tissue, and the branches were ligated with suture under dissection microscope in 4°C PBS (physiological buffer solution).

Samples were then cannulated for mechanical testing. These segments harvested from the same pig were studied in parallel. Samples were secured within a chambered vascular testing system (Bose BioDynamic 5270) via 4-0 sterile suture. The testing chamber was filled with phosphate buffered saline solution and maintained at 37 °C.

Mechanical testing

The original unloaded outer diameter and axial length of the mounted sample (zero pressure and zero axial force) were measured using caliber and custom LabView software, with each measurement repeated for verification. For a 15 min of acclimation at

a luminal pressure of 80 mmHg and in vivo axial stretch obtained from pilot studies, the specimen was preconditioned via a 5 cycles of pressurization from 0 to 200 mmHg at ~1.3 mmHg/s to exclude the excessive hysteresis. Biaxial data were then collected during cyclic pressurization tests in 20 mmHg steps from 0 to 200 mmHg at the same rate and mean in vivo stretch as well as at 10% above and below this stretch.

Zero-stress configuration

It is well documented that stress-free configuration which manifested as a sector obtained from making a radial cut on an unloaded ring segment is used to quantify the strain. The opening angle which bisect the sector is an indicator of the residual stress existed in the ring segment. 3 measurements around the circumference of each sector were averaged to yield mean values for each specimen.

Histology

Following mechanical testing, multiple ring samples from each test segment were paraffin-embedded and processed with Verhoeff-Masson's combination staining protocols. Histological slides were then analyzed using light microscopy and estimated the area fractions of elastin and collagen within each segment. Average values were recorded for each vessel and expressed as a percentage of total vessel dry mass.

Constitutive framework

We employed a ‘‘four fiber family’’ structure-motivated constitutive model to quantify the measured passive biaxial mechanical behaviors.

$$W(C, M^i) = \frac{c}{2} (I_c - 3) + \sum_{k=1,2,3,4} \frac{b_1^k}{2b_2^k} \{ \exp[b_2^k (I_4^2 - 1)^2] - 1 \} \quad (4.1)$$

Where c , b_1^k are material parameters with units of stress and b_2^k are dimensionless,

$I_c = \text{tr}\mathbf{C} = \lambda_r^2 + \lambda_\theta^2 + \lambda_z^2$ is the first invariant of the right Cauchy-Green tensor, and $I_4^2 = \mathbf{M}^i \cdot \mathbf{C}\mathbf{M}^i$ is the square of the stretch of the i th collagen fiber family. Collagen fiber orientations are defined in the reference configuration by unit vector \mathbf{M}^i , which depends on the fiber angles α^i defined between fiber and axial directions. So the axial and circumferential fibers were defined at $\alpha^1 = 0^\circ$ and $\alpha^2 = 90^\circ$, respectively, while symmetrically oriented diagonal fibers were defined via a single parameter, $\alpha^3 = -\alpha^4 = \alpha$.

$$I_4 = \lambda_z^2 \cos^2 \alpha + \lambda_\theta^2 \sin^2 \alpha, \quad (4.2)$$

These two diagonal collagen fiber family are approximately mechanically equivalent, so $b_1^3 = b_1^4$, $b_2^3 = b_2^4$. This model requires estimation of 8 unknown parameters ($c, b_1^1, b_2^1, b_1^2, b_2^2, b_1^3, b_1^4, \alpha$) that characterize the passive mechanical behavior. Best-fit values of unknown parameters were determined using a nonlinear least square minimization of the error Ω between theoretically predicted and experimentally inferred applied loads, namely

$$\Omega = \sum_{n=1}^N \left[\left(\frac{P_n^T - P_n^E}{P_n^E} \right)^2 + \left(\frac{F_n^T - F_n^E}{F_n^E} \right)^2 \right] \quad (4.3)$$

Where N is the total number of data points. The error Ω was minimized using the built-in function *lsqnonlin* in MATLAB, physical constraints were imposed so that $c, b_1^k, b_2^k \geq 0$ and $0 \leq \alpha_0 \leq \pi/2$.

In order to evaluate functional equivalency between the graft and host artery under grafted loading conditions with equal pressure and axial stretch ratio, criteria was proposed yielding the following system of equations:

$$\Omega_s = \frac{2|\sigma_\theta^* - \sigma_\theta^g|}{(\sigma_\theta^* + \sigma_\theta^g)} + \frac{2|\sigma_z^* - \sigma_z^g|}{(\sigma_z^* + \sigma_z^g)} \quad (4.4)$$

$$\Omega_c = \frac{2|c^g - c^h|}{(c^g + c^h)} \quad (4.5)$$

$$\Omega_{ri} = \frac{2|r_i^g - r_i^h|}{(r_i^g + r_i^h)} \quad (4.6)$$

$$\Omega = \frac{2|\sigma_\theta^* - \sigma_\theta^g|}{(\sigma_\theta^* + \sigma_\theta^g)} + \frac{2|\sigma_z^* - \sigma_z^g|}{(\sigma_z^* + \sigma_z^g)} + \frac{2|c^g - c^h|}{(c^g + c^h)} + \frac{2|r_i^g - r_i^h|}{(r_i^g + r_i^h)} \quad (4.7)$$

σ_θ^* (σ_z^*) is mean circumferential (axial) stress of graft under its own homeostatic state, σ_θ^g (σ_z^g) is mean circumferential (axial) stress of graft under physiological mechanical states of host artery (coronary artery). C^g is the compliance of graft under physiological mechanical states of host artery (coronary artery), C^h is compliance of host artery (coronary artery) under physiological mechanical states. r_i^g is the inner radius of graft under mechanical states of host artery (coronary artery), r_i^h is inner radius of host artery (coronary artery) under physiological mechanical states.

Statistical analysis

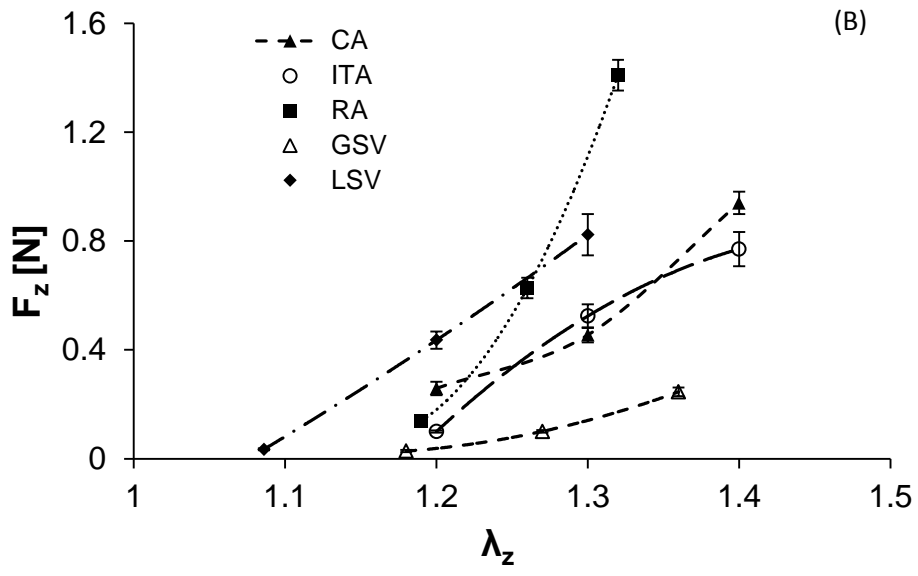
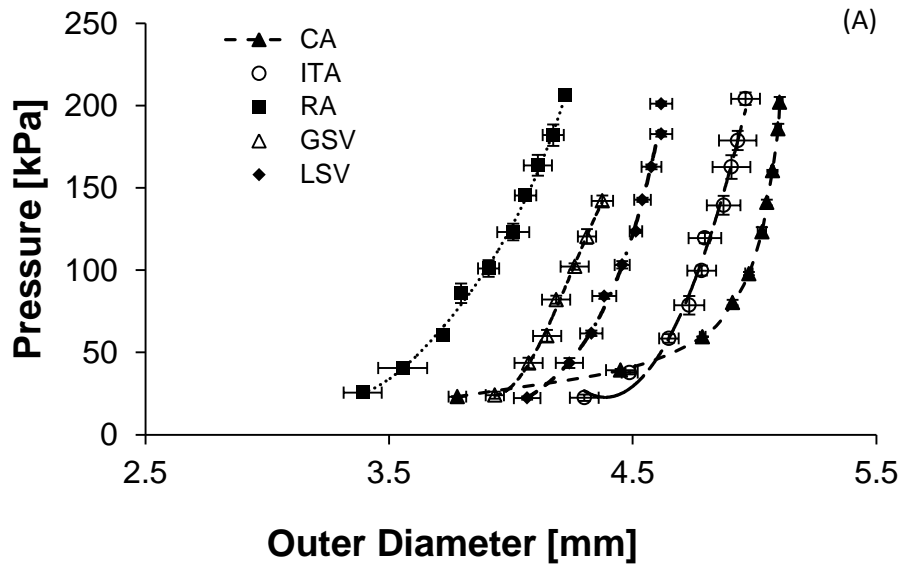
All data are expressed as mean \pm STD unless otherwise specified. Statistical significance was evaluated by using student t-test for unpaired values. For the overall study, values were considered statistically significant at $p < 0.05$.

4.4 Results

Mechanical response of tested specimens

Pressure – deformed outer diameter relationships of the porcine CA, ITA, RA, GSV and LSV revealed a high degree of nonlinearity at in situ axial stretch (Figure 4.1(A)). CA was highly distensible up to the pressure range of 20-60 mmHg, after which it became extremely stiff; whereas other graft vessels were less distensible than CA at low pressures but remained relatively distensible even up to 200 mmHg. In baseline

conditions, the outer diameter of the ITA was larger than that of RA and GSV was larger than that of LSV. Force measurements taken during P-d tests indicated that the axial wall force increased with increasing axial stretch (Figure 4.1 (B)). Although the range of axial stretch ratios used for testing was different for various vessels, there were stretch ratios that overlapped in all groups. For each vessel tested, there was an in situ axial stretch ratio at which the force remains nearly constant with increased pressure. Compliances of various blood vessels were calculated at various pressures, showing that the blood vessel became less compliant with increasing pressure (Figure 4.1 (C)).



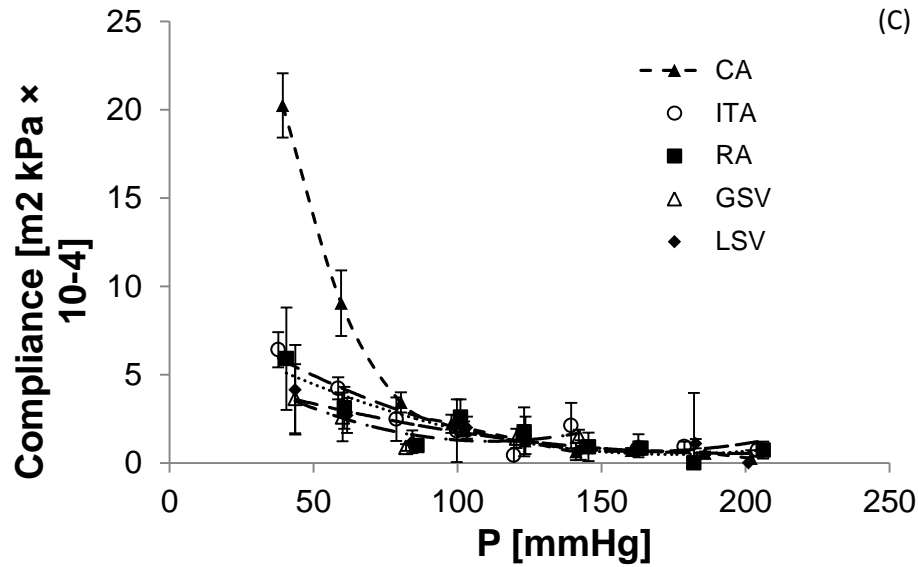


Figure 4.1. Representative plots of pressure-diameter (A), axial force-axial stretch (B) and compliance-pressure (C) relationships for CA, ITA, RA, GSV and LSV. Compliance calculated at 20 mmHg at the grafted axial stretch ratio.

Zero-stress configuration

The zero-stress configuration of the tested specimens was modeled as a circular sector characterized by an inner arc length, outer arc length, and wall thickness. The opening angle of each sector was calculated based on these measurements. The geometrical parameters characterizing the zero-stress configuration of the tested samples were reported in Table 4.1. It showed that outer and inner arc lengths of ITA were greater than that of RA. However, Thickness of RA was greater than that of ITA and LSV. No statistical difference in opening angle among these blood vessels was observed.

Table 4.1. Vessel geometry of stress-free configuration.

Sample	Outer arc-length(Lo) [mm]	Inner arc-length(Li) [mm]	Opening angle(OA) [°]	Thickness(H) [mm]
CA	13.77 ± 1.53	10.43 ± 1.45	70.14 ± 12.46	0.88 ± 0.11
RA	8.70 ± 1.63	4.65 ± 1.21	45.24 ± 26.42	0.87 ± 0.06
ITA	13.38 ± 0.9	10.82 ± 0.86	44.89 ± 18.22	0.55 ± 0.06
GSV	9.84 ± 2.32	6.06 ± 1.74	51.51 ± 25.03	0.84 ± 0.05
LSV	12.00 ± 4.26	8.65 ± 4.35	67.81 ± 22.18	0.87 ± 0.15

Histology

From histological studies, it was shown that the media of CA and ITA contained high content, distinct lamellae of straight and wavy elastin, within which the wavy collagen and smooth muscles were aligned circumferentially, permitting further extension of the arterial wall. The media in the SV and RA were mostly comprised of highly circumferentially oriented smooth muscle with very little elastin. Some bundles of straight and circumferentially oriented smooth muscle were observed in the middle of media of LSV (Figure 4.2).

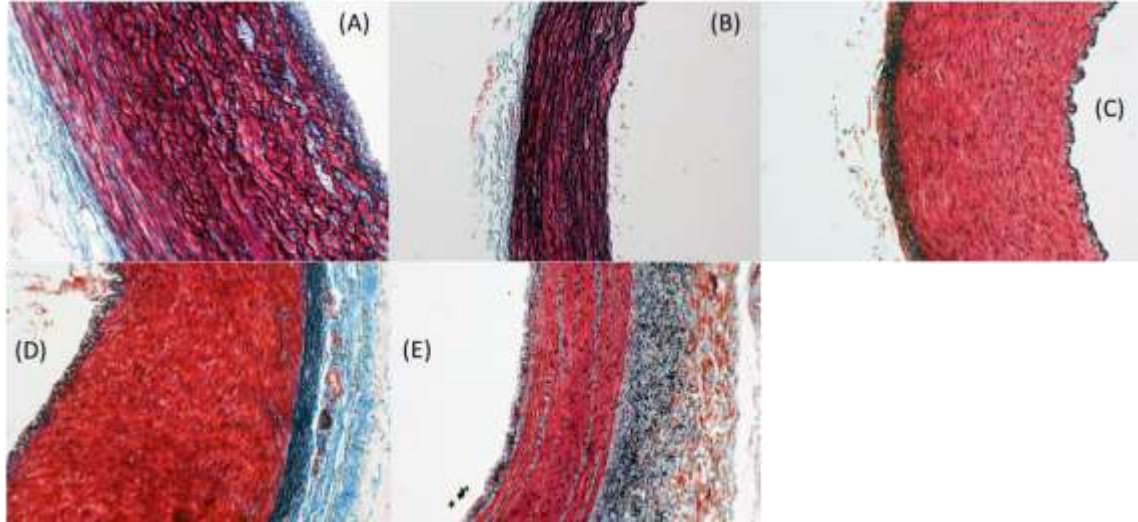


Figure 4.2. Histology of (A) CA, (B) ITA, (C) RA, (D) GSV and (E) LSV.

Parameter identification

The full range of mechanical behaviors in examined blood vessels was captured via proposed four-fiber constitutive model. Vascular tissue was modeled as anisotropic material with axial, circumferential and diagonal fibers embedded in an isotropic amorphous matrix. b represents the mechanical contribution of isotropic portion while b_1^k and b_2^k represent that of anisotropic fibers. The lower and upper limits of the parameters were prescribed as b and $b_1^k \in [0, 10^5]$, $b_2^k \in [0.1, 8]$, and $\alpha \in [0^\circ, 90^\circ]$. The values of error indicated reasonably good fits to experimental data. Results from parameter estimation showed ITA had significant higher b_1^1 than other vessels, indicating larger mechanical contribution from circumferential oriented collagen fiber family. There was significant difference in exponential term b_2^1 between ITA and LSV as well as between GSV and LSV implying different mechanical contribution of axially aligned collagen fibers. Meanwhile, a statistical difference was observed in b_3^1 between radial artery and LSV, which represents the mechanical contribution of the diagonally oriented collagen

fibers (Table 4.2). Obtained parameters were then used to calculate circumferential stress distribution across the vessel wall under various pressures. It showed that under same biaxial mechanical loads, the level of circumferential stress distribution of ITA was most similar to that of CA and significant higher than other blood vessels (Figure 4.3).

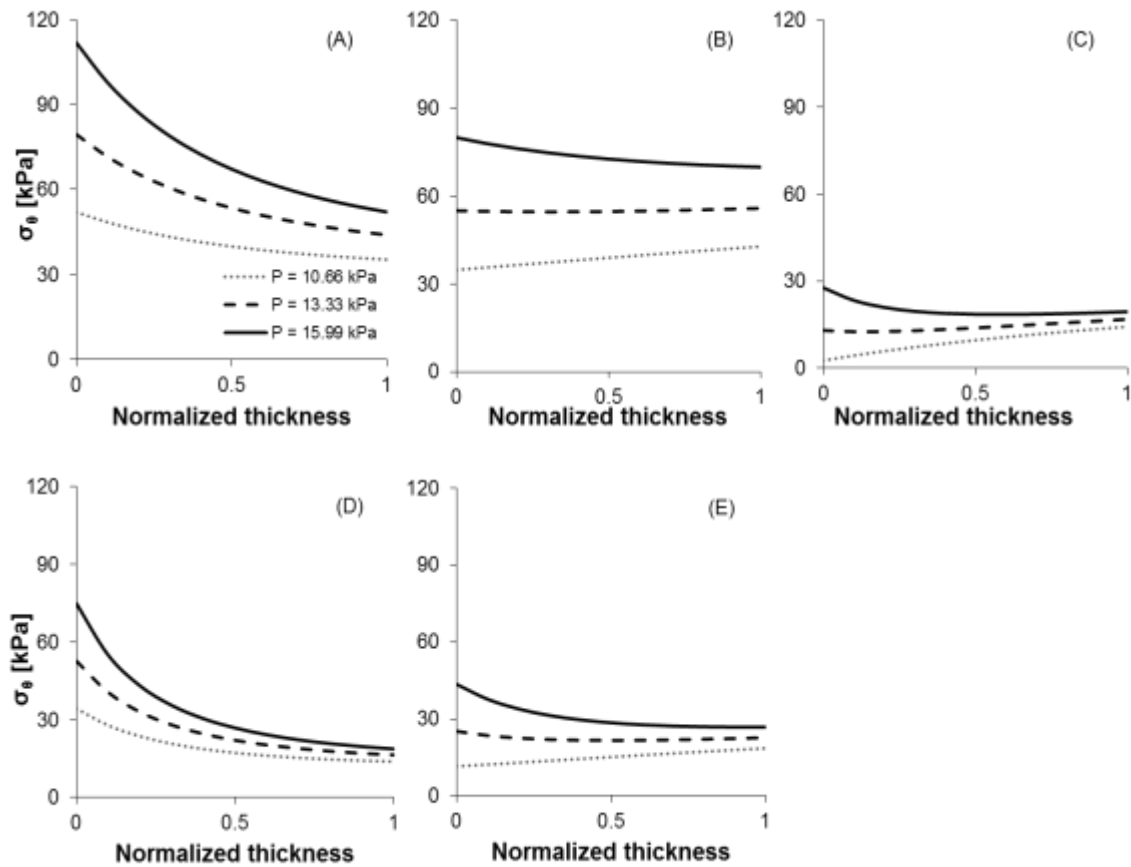


Figure 4.3. Circumferential stress distribution across the vessel wall of (A) CA, (B) ITA, (C) RA, (D) GSV and (E) LSV under physiological loading conditions of coronary artery.

Table 4.2. Material parameters for CA, ITA, RA, GSV and LSV obtained for a four-fiber constitutive model.

Sample	b_0 [kPa]	b_{11} [kPa]	b_{12}	b_{21} [kPa]	b_{22}	b_{31} [kPa]	b_{32}	α [°]	Residual
CA	3.5 ± 2.8	18.7 ± 12.7	1.8 ± 2.9	1.96 ± 1.88	3.15 ± 2.08	7.51 ± 10.77	3.98 ± 1.4	40.49 ± 10.01	0.73 ± 0.34
RA	5.2 ± 8.2	7.9 ± 11.3	0.6 ± 0.78	17.79 ± 10.84	4.19 ± 2.02	17.81 ± 27.61	3.73 ± 2.82	35.25 ± 4.98	0.52 ± 0.12
ITA	17.5 ± 16.9	17.2 ± 5.7	0.34 ± 0.1	4.52 ± 3.7	3.38 ± 2.42	22.69 ± 30.59	4.05 ± 2.26	34.13 ± 13.22	0.52 ± 0.15
GSV	4.4 ± 5.85	6.9 ± 4.98	1.75 ± 2.9	14.01 ± 10.57	3.93 ± 3.16	24.35 ± 33.62	4.46 ± 2.55	37.68 ± 14.34	0.74 ± 0.23
LSV	5.5 ± 8.25	4.7 ± 4.03	0.63 ± 0.6	0.91 ± 1.31	2.83 ± 3.09	2.62 ± 3.23	4.02 ± 2.97	41.94 ± 14.91	0.43 ± 0.23

Structural properties of various blood vessels under grafted loading conditions were shown in Table 4.3, demonstrating significant lower compliance of RA than other vessels. The overall normalized comparison in the mechanical and structural properties between graft and host artery were shown in 4.4 (A). Averaged circumferential and axial stresses of various vascular wall under homeostatic and grafted mechanical states were calculated and their difference were normalized as shown in Figure 4.4 (B) and Table 4.4. Normalized comparison in compliance between the graft and host artery under grafted loading conditions were shown in Figure 4.4 (C). Normalized comparison in inner radius between the graft and host artery under grafted loading conditions were shown in Figure 4.4 (D).

Table 4.3. Vessel structural properties at representative graft loading conditions ($\lambda_z = 1.2$, $P = 100$ mmHg)

Vessel	Deformed inner radius [mm]	Compliance [$m^2 \text{ kPa} \times 10^{-4}$]
CA	2.3 ± 0.34	3.49 ± 1.39
ITA	2.01 ± 0.14	4.1 ± 1.4
RA	0.94 ± 0.12	0.7 ± 0.3
GSV	1.07 ± 0.23	1.3 ± 0.3
LSV	2.05 ± 0.74	2.3 ± 0.6

Table 4.4. Vessel mechanical properties at homeostatic and graft loading conditions

Vessel	P [*] [mmHg]	Homeostatic conditions			Grafted conditions $\lambda_z = 1.2, P = 100$ mmHg		Remodeling stimulus	
		λ_z^*	$\langle \sigma_\theta^* \rangle$ [kPa]	$\langle \sigma_z^* \rangle$ [kPa]	$\langle \sigma_\theta^G \rangle$ [kPa]	$\langle \sigma_z^G \rangle$ [kPa]	$ \sigma_\theta^G - \sigma_\theta^* $	$ \sigma_z^G - \sigma_z^* $
ITA	100	1.2 ± 0.1	70.92 ± 17.5	73.81 ± 17.42	68 ± 12.84	57.45 ± 30.3	2.92 ± 5.82	16.36 ± 29.06
RA	80	1.17 ± 0.1	13.06 ± 3	84.97 ± 96.11	20.54 ± 3.54	101.44 ± 52.4	7.73 ± 5.19	87.29 ± 74.12
GSV	20	1.22 ± 0.1	3.09 ± 1.01	72.57 ± 109.1	20.6 ± 2.8	89.39 ± 119.5	15.29 ± 6.34	98.94 ± 116.6
LSV	20	1.34 ± 0.2	6.89 ± 3.66	30.42 ± 22.44	48.96 ± 16.3	24.57 ± 20.7	34.9 ± 18.5	31.63 ± 19.03

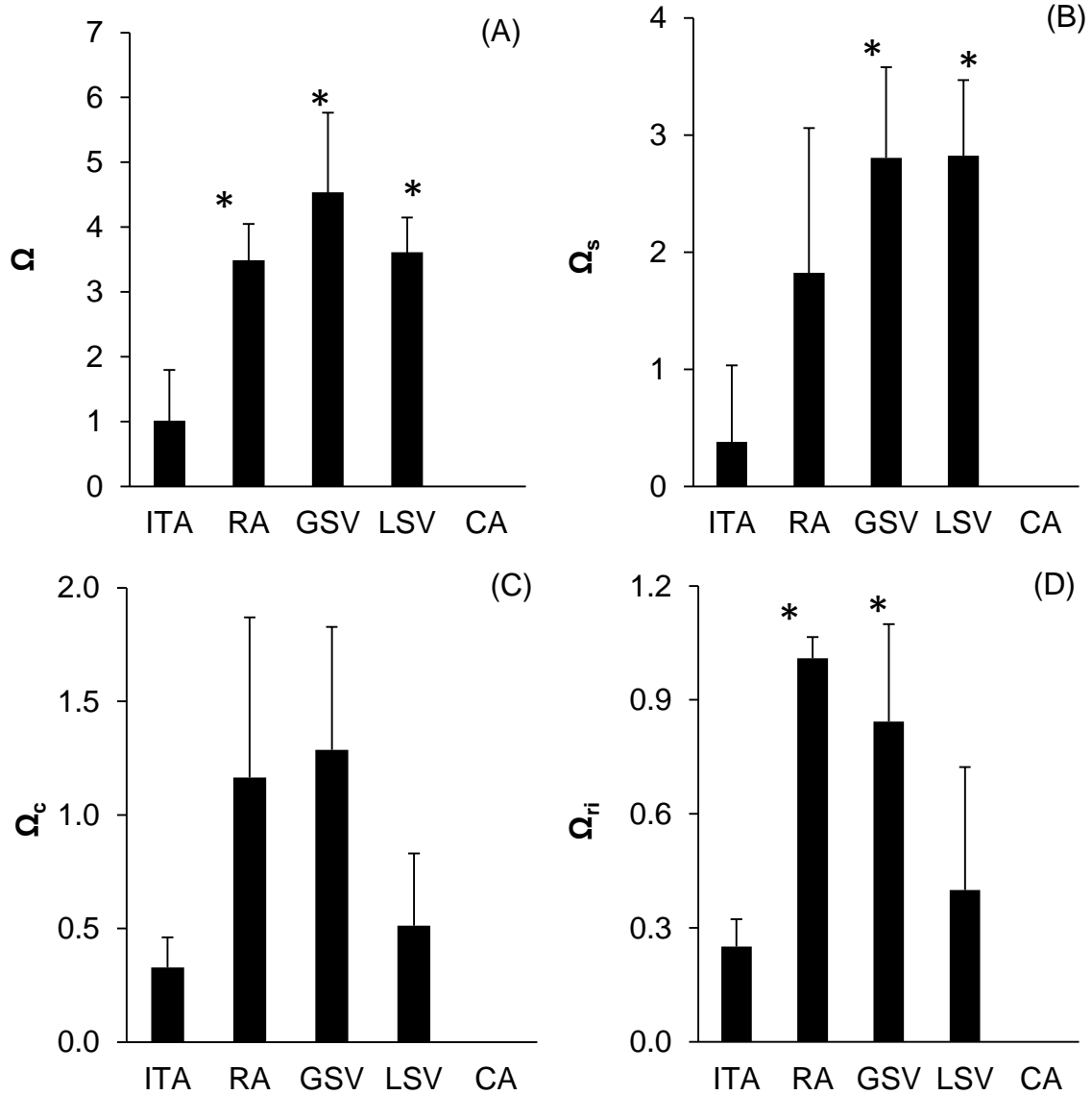


Figure 4.4. Comparison of normalized difference in comprehensive mechanical properties (A), in stresses between homeostatic and grafted loading states (B), in compliance under grafted loading conditions (C), internal radius under grafted loading conditions (D) of RA, ITA, GSV and LSV(mean \pm SD, n=5 for each group) among

different groups. (*) $p < 0.05$ represents a significant statistical difference compared with internal thoracic artery.

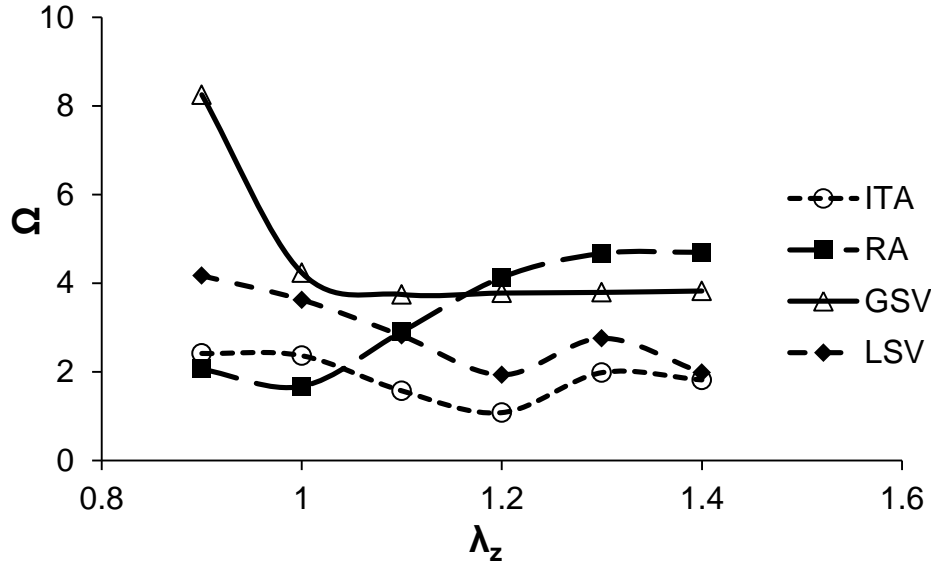


Figure 4.5. Vessel normalized difference in overall mechanical properties as a function of axial stretch ratio.

4.5 DISCUSSION

The goal of this study was to develop a methodology to evaluate mechanical compatibility of ITA, RA, GSV and LSV as autologous coronary artery grafts. The obtained descriptive results were illustrated in terms of the luminal pressure-deformed outer diameter and luminal pressure-axial force relationships at various degree of axial stretch. A structure-motivated constitutive model was validated to solve boundary-value problems, predicting mechanical responses and stress distribution of vascular wall under various loading scenarios. The differences of mean wall stresses, compliance, and inner radius between the coronary artery and graft were normalized and compared.

Most of the data obtained from the mechanical testing are within the range of results of other porcine blood vessels from previous work. Nonlinear pressure-deformed outer diameter relationships as well as phenomenon of decent in compliance as a function of pressure were attributed to nonlinear mechanical properties of elastin and stiffening effect from the collagen fibers as they were gradually recruited and bear the load with increasing higher pressure. The character of axial force – axial stretch response is in qualitatively agreement with previous published data on large conduit arteries [107, 137]. The values of opening angle which characterize the stress-free configuration of various vascular conduits are similar to results reported in other studies [138, 139]. The morphological results showed that thickness of RA and GSV were approximately as same as CA, indicating their suitability for both coronary artery and aortic anastomoses [18]. Under the same pressure, the mean circumferential stress is proportional to r/t (vessel inner radius/vessel wall thickness). The ITA endowed with larger diameter and thin wall may bear a much higher internal circumferential stress (σ_θ) than RA and LSV ($\sigma_\theta = \frac{\Delta Pr}{t}$). Therefore, it is more likely to induce vascular smooth muscle proliferation in ITA due to higher circumferential stress under grafted loading conditions.

Histological results revealed the organization of structural constituents within the vascular wall. The pressure-deformed diameter curve of the grafts did not exhibit the same degree of dispensability over the range of low pressures as that of CA. These differences in passive mechanical responses may be because of higher content of wavy circumferentially oriented elastin within the arterial wall of CA than SV and RA. However, endowed with high amount but less wavy elastin in the media, ITA was not as distensible as CA at low pressures. As typical muscular blood vessels, SV and RA are

mostly consisted of smooth muscle cells within the media. The orientation of smooth muscle is of great importance since its extension may induce smooth muscle proliferation and trigger hyperplasia [140-143].

Post-implantation of grafts may mechanically induce vascular remodeling as cells sense and adapt to their epicardial mechanical environment. These adaptation or maladaptation, such as restenosis of vascular grafts, could affect the outcomes of clinical interventions. Quantification of the mechanobiological response of cells to the fluctuation in local mechanical environment requires a constitutive model with adequate predictive capability. Since elastin and collagen fibers are major structural constituents of vascular remodeling, we used a structure-motivated constitutive model with the capability of predicting stress distribution across the vascular wall under certain mechanical loads. It showed that the vascular cells in the ITA experienced similar mechanical environment as that of coronary artery under grafted loading conditions, implying that ITA requires less remodeling than other grafts and corroborating the results from other studies that ITA has better long-term patency than SV and RA.

Structural incongruities between graft and target artery play a major part in determining the graft patency. Mismatch of compliance between the host and graft vessels may result in internal hyperplasia at the anastomosis [144]. Mismatched deformed inner radius may give rise to competitive blood flow, inducing abnormal low shear stress on the endothelial cells [145]. Normalized comparisons in compliance and deformed inner radii obtained from our results indicated that ITA was the most compatible graft for coronary artery. This speculation is also indirectly supported by the least deviation in circumferential stress distribution between ITA and CA under physiological conditions of

CA, suggesting ITA was most mechanically similar to coronary artery and requires the least remodeling among various grafts which corroborated results from previous clinical studies that ITA has the lowest failure rates [18, 146-148].

Mechanical compatibility of various grafts varies significantly with their axial stretch. In vivo mechanical stability of the vascular tissue is partially maintained by longitudinally extension of the vascular wall so that the magnitude of resultant axial stress is virtually independent with periodic pressure [98, 149, 150]. Abnormal high axial stress at the anastomoses between the graft and host artery may increase the risk of hemorrhaging with vascular remodeling ensued [151, 152]. Differences in axial stretch for optimal mechanical compatibility of various grafted vessels provide reference information to cardiovascular surgeons and suggest them consider varying axial stretch ratios of grafts based on the type of vessel to obtain best clinical outcomes.

4.6 STUDY LIMITATIONS

There are several limitations to this approach. First, mean Cauchy circumferential stress vs. mid-wall stretch and stress distribution analysis were conducted under the assumption that tissue is homogenous. However, there is evidence of the existence of heterogeneity in the media and adventitia of vascular soft tissues. Further studies should incorporate the two-layer heterogeneous constitutive model to capture the mechanical behaviors of media and adventitia in grafted blood vessels respectively. Secondly, we only assessed the passive mechanical response of various vascular grafts without concerning the effect of VSMCs basal tone. The contractile states of VSMCs within the arterial wall significantly affect the structural properties such as compliance of vascular wall. Further studies that quantify the microstructure and constitutive coupled with

contractile states of vascular smooth muscle cells will help us comprehend the overall mechanical properties of vascular grafts.

4.7 CONCLUSION

In conclusion, the present study quantified passive mechanical responses of porcine CA, ITA, RA, GSV and LSV. Most notably, this is the first study to our knowledge to investigate the mechanical properties of various autologous coronary artery grafts which are critical factors in determining graft patency. The ideal to be aimed at is to weigh against their advantages and disadvantages so as to select a graft that could restore blood flow without disturbing the normal mechanical environment of the host artery and correspondingly reduce the rate of intimal hyperplasia. The optimal selection of grafts can reduce the risk of early complication and progressive deterioration of graft function, providing a framework for cardiovascular surgeons to deliver better clinical outcomes.

4.8 STUDY TRANSITION

In the previous study, we have compared the mechanical properties of various vascular grafts and evaluated their suitability and potential long-term patency. The next question is what we would do if native vein or artery is not available because of previous harvest, anatomical limitations, or disease progression. Synthetic materials have demonstrated greater success in large diameter vascular prostheses yet poor performance for small ones. To solve this problem, novel tissue-engineered vascular constructs were fabricated and following mechanical characterization of this material was conducted to evaluate its clinical feasibility.

CHAPTER 5

MECHANICAL CHARACTERIZATION OF TISSUE-ENGINEERED VASCULAR CONSTRUCTS

5.1 ABSTRACT

To meet demands of vascular reconstruction, there is a need for prosthetic alternatives to natural blood vessels. Here we explored a new conduit fabrication approach. Macroporous, gelatin microcarriers laden with human umbilical vein endothelial cells and aortic smooth muscle cells were dispensed into tubular agarose molds and found to adhere to form living tubular tissues. The tubular tissues behaved as elastic solids, with a uniaxial mechanical response that is qualitatively similar to that of native vascular tissues and consistent with their elastin and collagen composition. Linearized measures of the mechanical response of the fabricated tubular tissues at both low and high strains were observed to increase with duration of static culture, with no significant loss of stiffness following decellularization. The geometry and mechanical properties of circumferential stretched samples showed no statistical difference compared to the specimens cultured in agarose molds. Tubular tissues were then stacked and cultured to form vascular substitutes. The mechanical properties of these tubes were

assessed via burst pressure and suture retention strength tests, with comparatively lower values due to poor cross-linking elastin and collagen. The findings highlight the utility of cellularized macroporous gelatin microcarriers as self-adhering building blocks for the fabrication of living tubular structures.

5.2 INTRODUCTION

Availability of suitable autologous vascular conduits derived from a patient's body was limited for vascular replacement surgical procedures [153]. A variety of approaches have been developed to fabricate blood vessels [26, 30, 154-157]. These include the use of tubular scaffolds manufactured from natural and synthetic biomaterials that are subsequently seeded with vascular cells to create living prostheses [26-29]. We were motivated to explore alternative approaches that would facilitate cell-based fabrication of conduits comprised of vascular cells and extracellular matrix (ECM) constituents that they synthesize.

Microcarrier beads are 100-300 μm diameter spherical particles that allow attachment and growth of anchorage-dependent cells while in suspension culture [158-160]. Microcarrier beads are manufactured from natural and synthetic materials, including gelatin, collagen, etc. variant forms of microcarrier beads are macroporous, having large pore of ten of micrometers that provide additional areas for cells to attach and grow [161, 162]. Microcarriers have been used for suspension tissue culture to produce high yields of anchorage-dependent cells and their secreted products, but in recent years their utility in tissue regeneration and tissue engineering has emerged.

Quantification of the mechanical properties of vascular tissue is essential for understanding the physiological function of arteries and for the design and fabrication of arterial substitutes to replace diseased vessels. Focusing on the development of tissue engineered arteries, it is important to obtain reliable and useful preliminary information about mechanical properties of tissue constructs immediately after fabrication and following mechanical preconditioning in bioreactors. Moreover, because vascular cells are mechanosensitive and the process of neo-artery formation is governed by the local stresses existing in the wall of the tissue engineered artery, there is pressing need to calculate the wall stress distribution across the vessel wall with appropriate predictive mathematical models. Proposing such models necessitates a constitutive formulation of arterial tissue in a framework of soft tissue biomechanics. The first step is to perform relatively simple mechanical experiments to quantify the material properties, while minimizing errors and artifacts, and to process the recorded data towards formulation of reliable constitutive equations.

Uniaxial tensile experiment is among the simplest mechanical tests that can be performed on a specimen made of a solid material. It is shown that uniaxial experiments performed on materials that undergo finite (large) deformations, such as soft tissues and tissue engineered constructs, are in general not sufficient to identify the constitutive stress-strain relationships. However, uniaxial experiments on these materials can reveal descriptive and useful mechanical information, provided the recorded experimental data are correctly processed and analyzed.

Focusing on blood vessels and tissue engineered vascular constructs, uniaxial experiments are done using specific shaped specimens; rings, dumbbell-shaped

specimens or specimens with helically-oriented fibres excised from tubular samples are commonly used [15, 163-166]. Since most soft tissues, including vascular tissue, are mechanically anisotropic, their mechanical properties depend upon the direction of the applied forces. Therefore careful specimen preparation for mechanical testing is necessary since the tissue excision may influence the results obtained. For example, the anisotropy introduced by collagen fibers in the arterial wall produces disparate results in uniaxial tests depending on whether the excised specimens are orientated longitudinally or circumferentially relative to the vessel axis [167].

Tissue engineered blood vessels (TEBV) to function properly and successfully must meet clinically-specific mechanical requirements such as burst pressure strength and suture retention strength (SRS). Appropriate burst pressure in TEBV is critical since graft failure may cause aneurysms, hemorrhage while internal hyperplasia induced by compliance mismatch may cause graft occlusion. Autologous grafts such as saphenous vein (SV) and internal mammary artery (ITA) show burst pressure of roughly 2000 mmHg [168, 169]. Meanwhile, the SRS of TEBV regarded as an indicator of mechanical strength in anastomosis, are of great importance to vascular surgeons. Studies showed that burst pressure and suture retention strength tests are adequate gauge of mechanical properties of vascular tissue constructs [170-172].

Here we utilized vascular cell-containing macroporous gelatin microcarriers (Cultispheres) in conjunction with agarose molds to facilitate 3D tissue engineering of living tubular constructs and evaluated their mechanical properties for clinical feasibility. Uniaxial tensile testing as well as burst pressure and suture retention strength tests were conducted. A particular focus is paid to the use of particle tracking techniques to identify

the sample region in which the tissue experiences homogeneous deformation. The results obtained from this study will provide a demonstration of the potentialities for improving the manufacturing procedure of this material.

5.3 MATERIALS AND METHODS

Ring constructs culture

Microcarrier beads laden with co-cultured human umbilical vein endothelial cells (HUVECs) and human aortic smooth muscle cells (HASMCs) were dispensed into tubular agarose molds, which after 7 days in culture yielded fused ring constructs of 4 mm outer diameter, 2 mm inner diameter, and 2.5 mm length (Figure 5.1). In a parallel set of studies, ring constructs were decellularized prior to mechanical testing. The constructs were washed in deionized (DI) water for 30 min, stirred continuously in PBS containing 1.0% sodium dodecyl sulfate (SDS) for 60-65h, and rinsed overnight in DI water. They were then rinsed one more time for 30 min, and finally stored in fresh DI water.

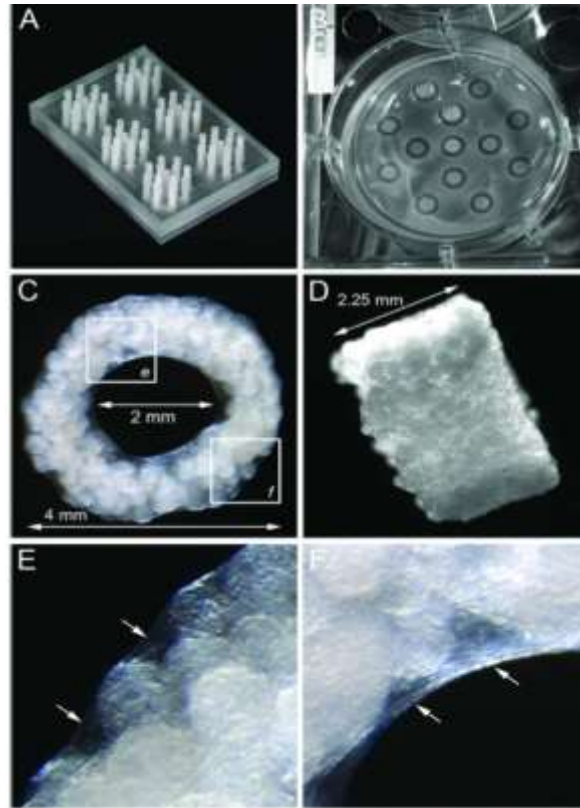


Figure 5.1. Fabricated Tubular Constructs. A, B, C, and D show different views of an elongated tubular construct that has been cultured for 17 days, E and F show the spherical microcarriers.

Static stretch of ring-shaped samples

Focusing on the effects of static internal circumferential stretch on the mechanical properties of fabricated tissue constructs, customized bio-inert vertical posts made from polylactic acid (PLA) were used to stretch the samples (Figure 5.2). Cellularized ring specimens removed from 2 mm agarose posts in molds were placed on PLA posts of 2 mm and 3 mm and cultivated for 12 days while cellularized samples cultured in 2 mm agarose molds were chosen as control group (Figure 5.3). Prior to mechanical experiments, Geometry of each specimen was measured after being removed from the posts. At least one minute of relaxation time was required to let the specimen reach resting state after removal, during which dot pattern can be applied on the sample.

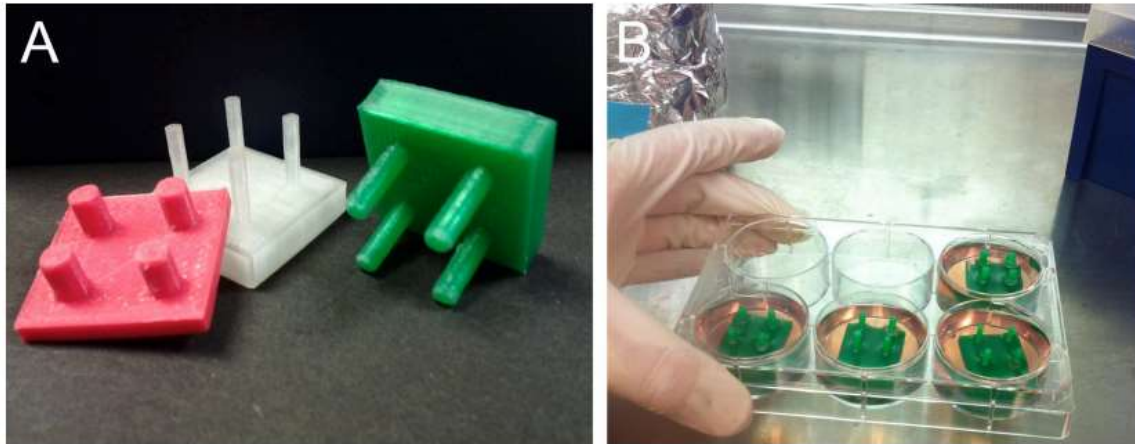


Figure 5.2. (A) bio-inert posts made of PLA, (B) posts placed in the molds.

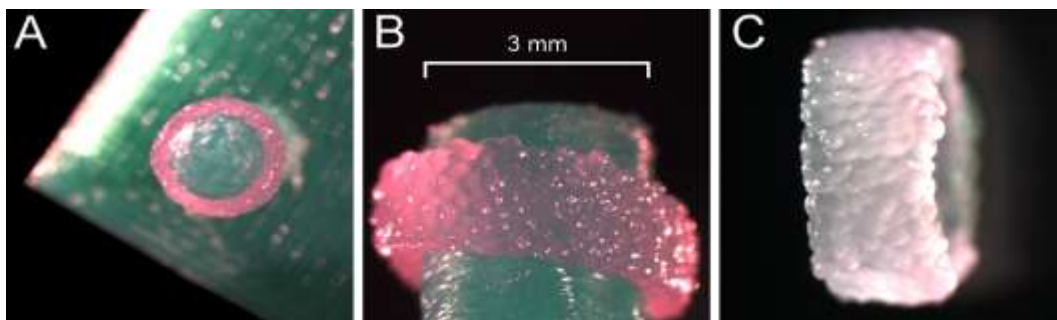


Figure 5.3. (A) torroids on the post of 2mm. (B) torroids placed on the 3mm post. (C) sideview of stretched torroids.

Stacked tube culture

After 5 days in agarose molds, tubular constructs were removed and stacked onto 2 mm diameter stainless steel center post guides mounted on an acrylic base plate in wells of 6-well plates. The stack tubes were submerged in 1:1 mixture of EGM-2 and SMGM and cultured for varying periods of time (Figure 5.4).

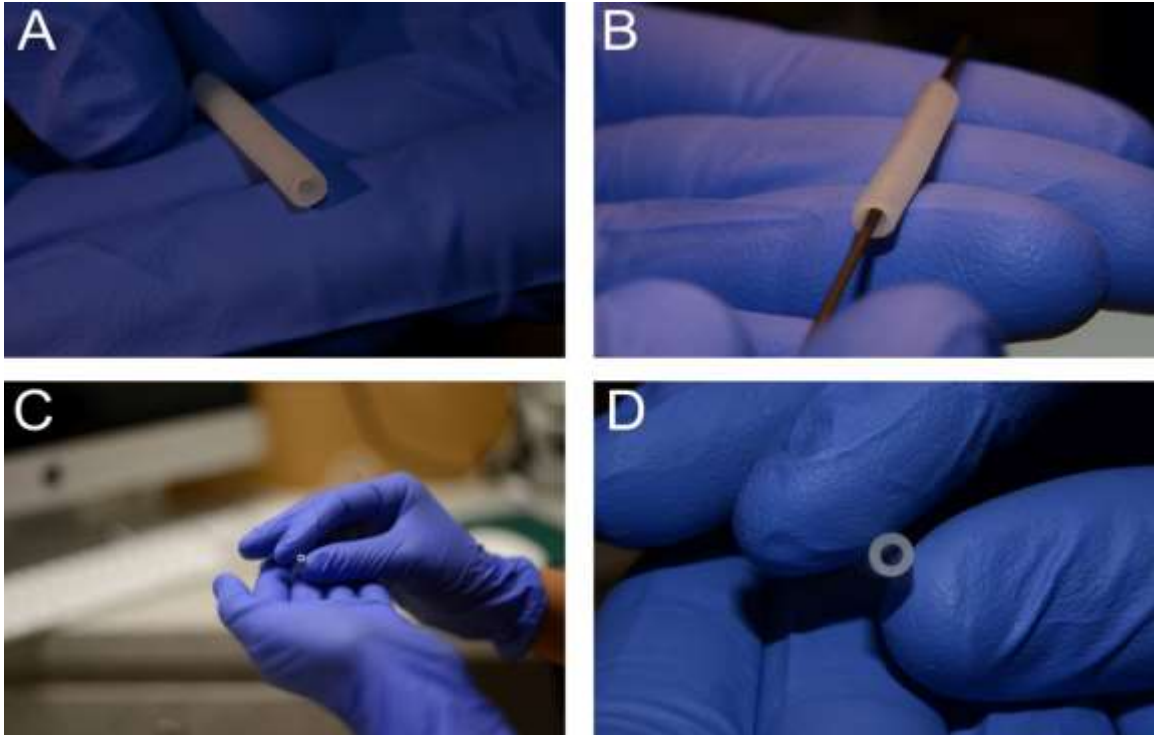


Figure 5.4. A, B, C and D display different view of stacked tube.

Uniaxial tensile testing

Five ring-shaped samples (outer diameter 4.00-4.17 mm, wall thickness 1.04-1.12 mm, wall height 2.21-2.25 mm) were prepared as described above and matured for 7 to 17 days prior to mechanical testing. To initiate mechanical testing, samples were removed from media and immediately secured onto horizontally-oriented 25 gauge cannulas mounted to the upper and lower arms of a uniaxial mechanical tester (Bose Enduratec 3200) (Figure 5.5). Samples were kept hydrated with culture medium while being mechanically preconditioned with four tensile displacement cycles up to 1.2 mm (20-25% strain) at a displacement rate of 0.01 mm/s. An identical fifth cycle was then immediately performed, during which load data (50 points/s) was recorded by system software (Bose, Wintest). An image-based technique was used to measure the local strain in the middle section of each sample. Blue tissue marking dye was applied to the sample

by a fine tip applicator to create a dot pattern. Images were captured using a Nikon SMZ-U light microscope and a Q- Imaging camera. Using Image Pro 5.1 to spatially calibrate the image, the vertical distance between the dots was used to calculate local strain (Figure 5.6).

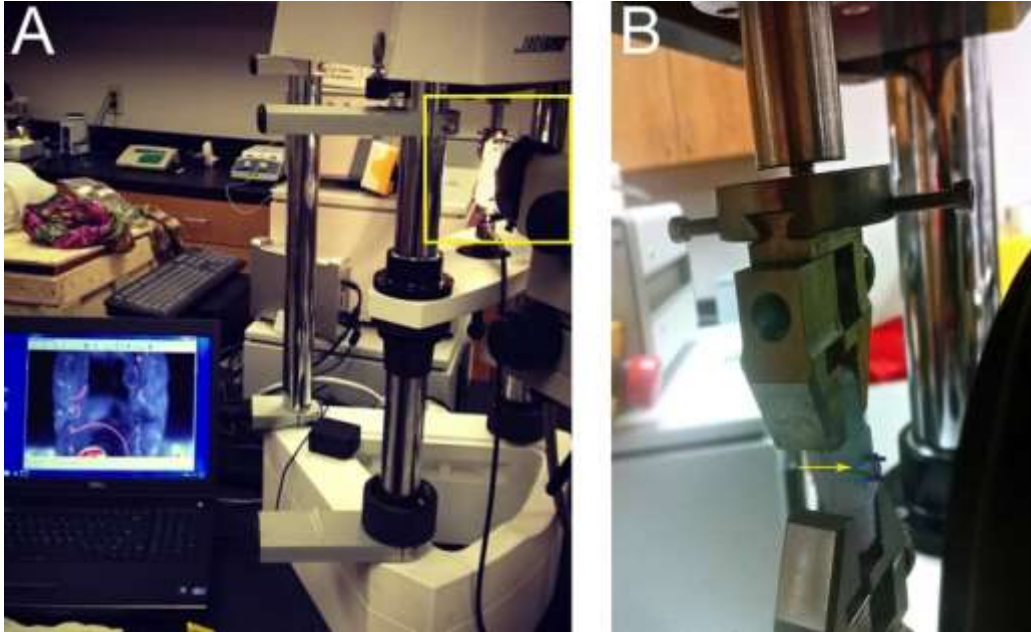


Figure 5.5. (A) Experimental Setup of Uniaxial Tensile Testing. (B) Close view of samples. Arrow pointing at the Toroid undergoing displacement.

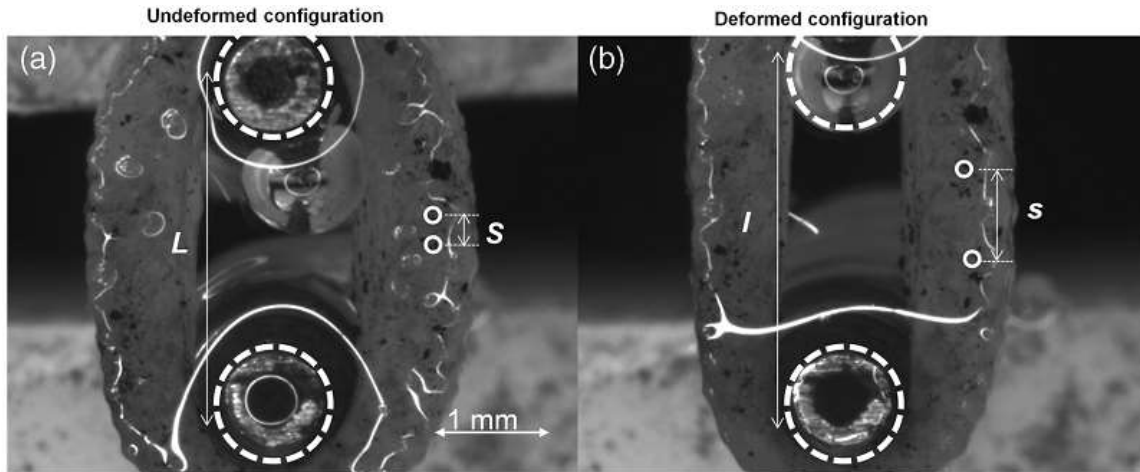


Figure 5.6. Acquired images from a uniaxial ring experiment on an engineering vascular construct. The distance between markers contained within the central region of the sample longitudinal axis was measured in the undeformed (a) and deformed (b) states to facilitate calculation of a local stretch ratio. The scale bar refers to both images.

Burst Pressure Testing

The tissue-engineered tube was fabricated and transported from Medical University of South Carolina. When it was arrived, agarose surrounding the tube was carefully removed using sterilized scalpel. The distal portion of the tube was then gently cannulated onto the 25-gauge plastic cannula and sutured using 4-0 silk suture. It was then mounted to the testing machine (Bose 5100 Biodynamic) (Figure 5.8). Burst pressure testing was performed by increasing the pressure from 10-200mmhg at a rate of 0.2 mmHg/s until failure. A Micro-tip catheter based pressure transducer (MPC-500, Millar) was placed into the inlet and used to measure the luminal pressure at a sampling rate of 3 Hz. Data was collected using data acquisition system (Wintest 7, Bose) at a rate of 3 Hz. In all cases, rupture occurred at a location away from the cannulation site.

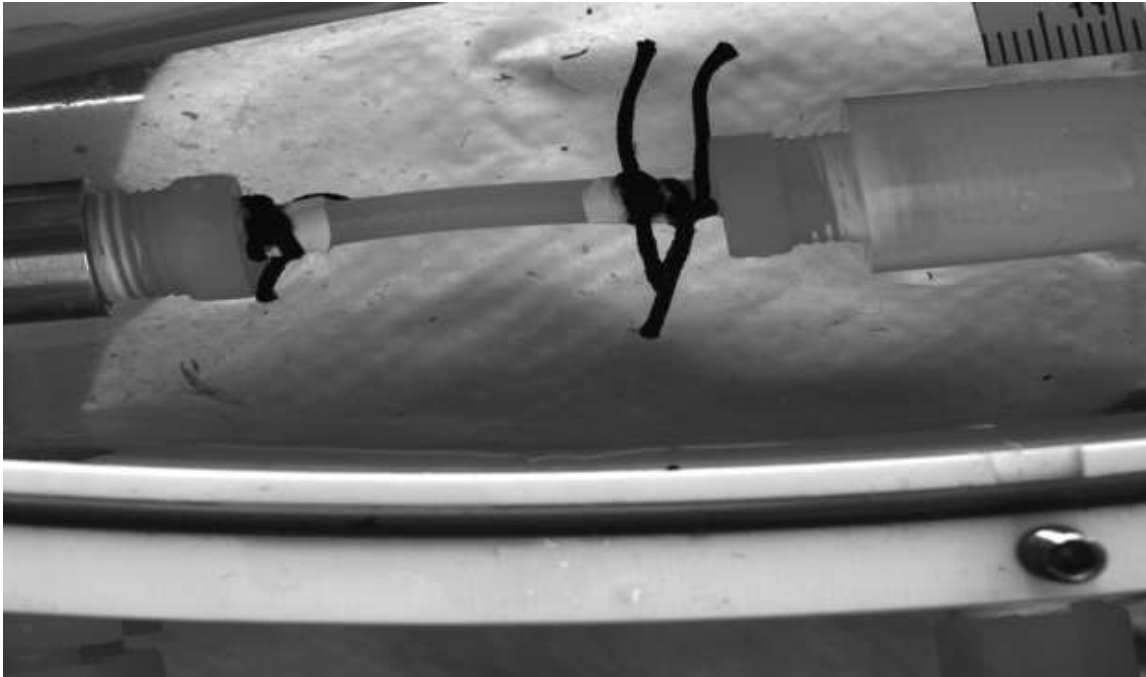


Figure 5.7. Experimental setup of burst pressure on the fabricated tube.

Following burst pressure testing a suture retention strength test was performed (Figure 5.8). A cut was made with a scalpel to the intact tube construct at a 45-degree angle to the long axis, as specified in the ANSI 7198 requirements. The elbow adapter nozzle with the attached loop gradually pulled the suture thread through the construct by increasing its displacement at a rate of 50 mm/min until the suture completely tore through the vessel wall. The maximum force required pulling the suture through the vessel was then recorded as the suture retention strength. The test was then repeated twice on the same sample at locations 120 degrees apart to obtain a total of three values for each vessel test segment, as specified in the oblique procedure in the ANSI 7198 Cardiovascular implant requirements.

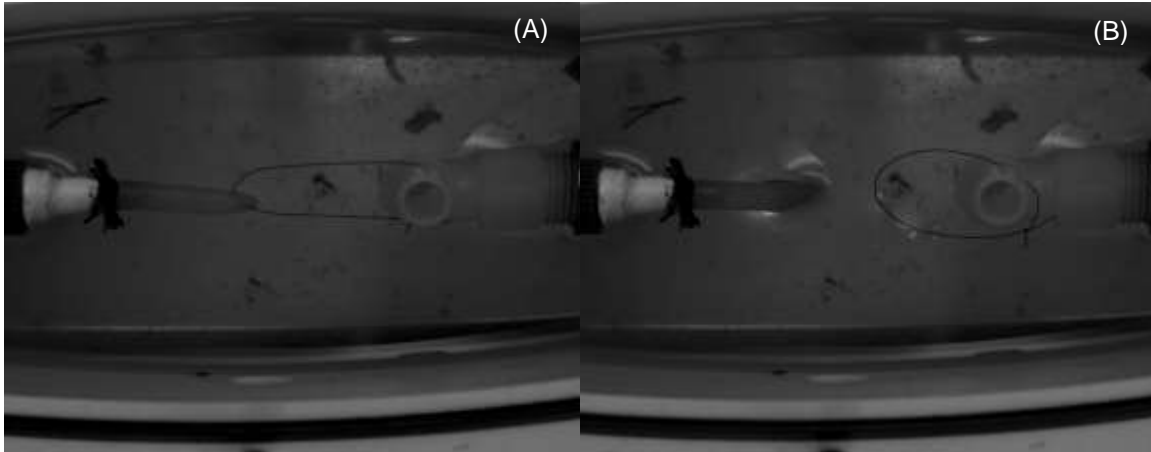


Figure 5.8. (A) Suture Retention Strength Test Set-up, The picture above shows the construct sutured to the plastic cannula mandrel on left, with the moveable post on the right (B) pulling the suture through the vessel wall.

5.4 RESULTS

Uniaxial mechanical response

The uniaxial mechanical response of Cultispher tubes was highly repeatable among the test samples ($n = 5$; outer diameter 4.00-4.17 mm, wall thickness 1.04-1.12 mm, wall height 2.21-2.25 mm) and exhibited a high degree of nonlinearity in the examined range (Figure 5.9 (a)). A representative plot of sample deformation showed a nonlinear elastic mechanical response. The sample was elongated to a stretch ratio of 1.18, which corresponds to 18% increase in length. The stress was increased nonlinearly with stretch ratio (Figure 5.9 (b)).

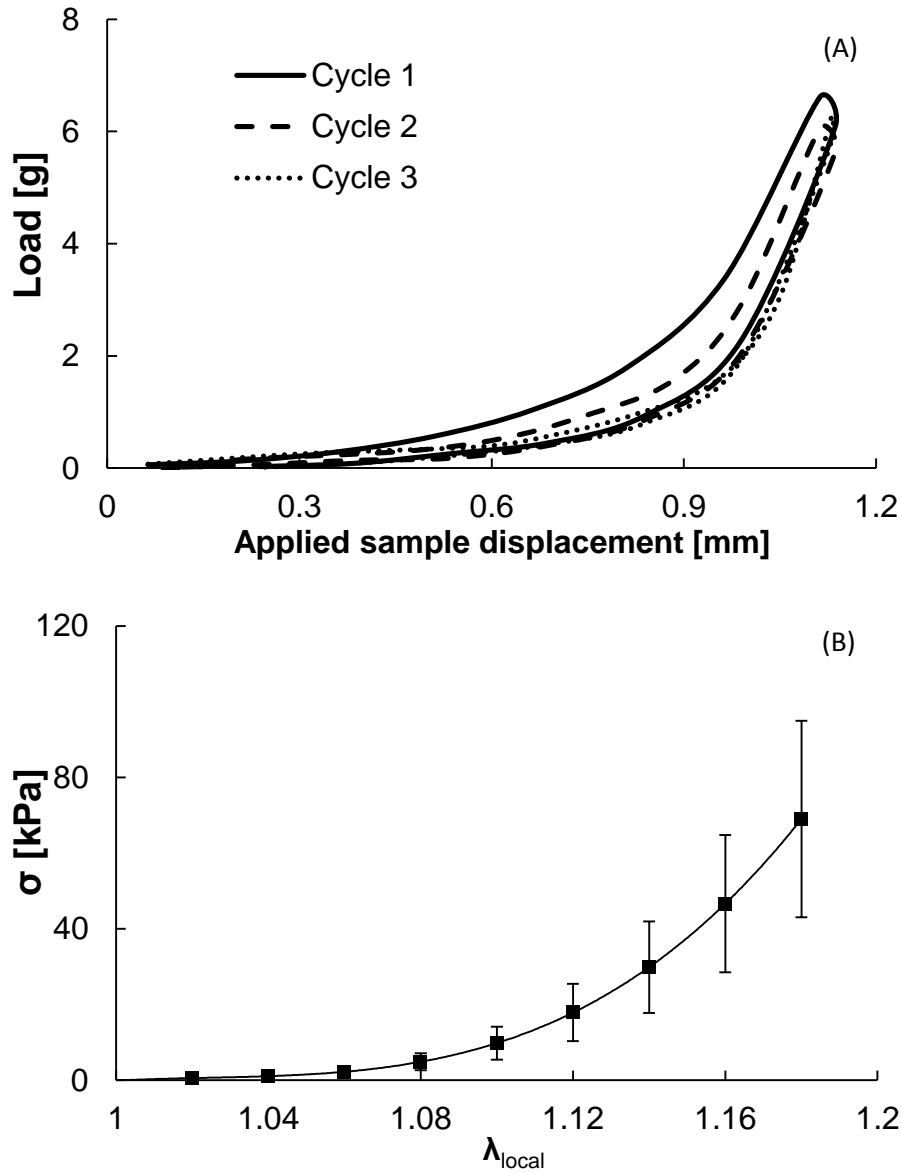


Figure 5.9. Experimental preconditioning and data obtained from uniaxial ring test. (A) Ring constructs were preconditioned via three loading-unloading cycles to obtain a reproducible elastic response. (B) Immediately following preconditioning, an identical fourth cycle was performed, and loading data processed to develop stress-stretch relations. Error bars represent the standard deviation of measurements made on four samples.

Cauchy stress-stretch relationship of cellularized constructs with various culture times was plotted as shown in Figure 5.10 (A). The comparison of mechanical properties

between cellularized and decellularized samples cultured for 17 days was shown in Figure 5.10 (B).

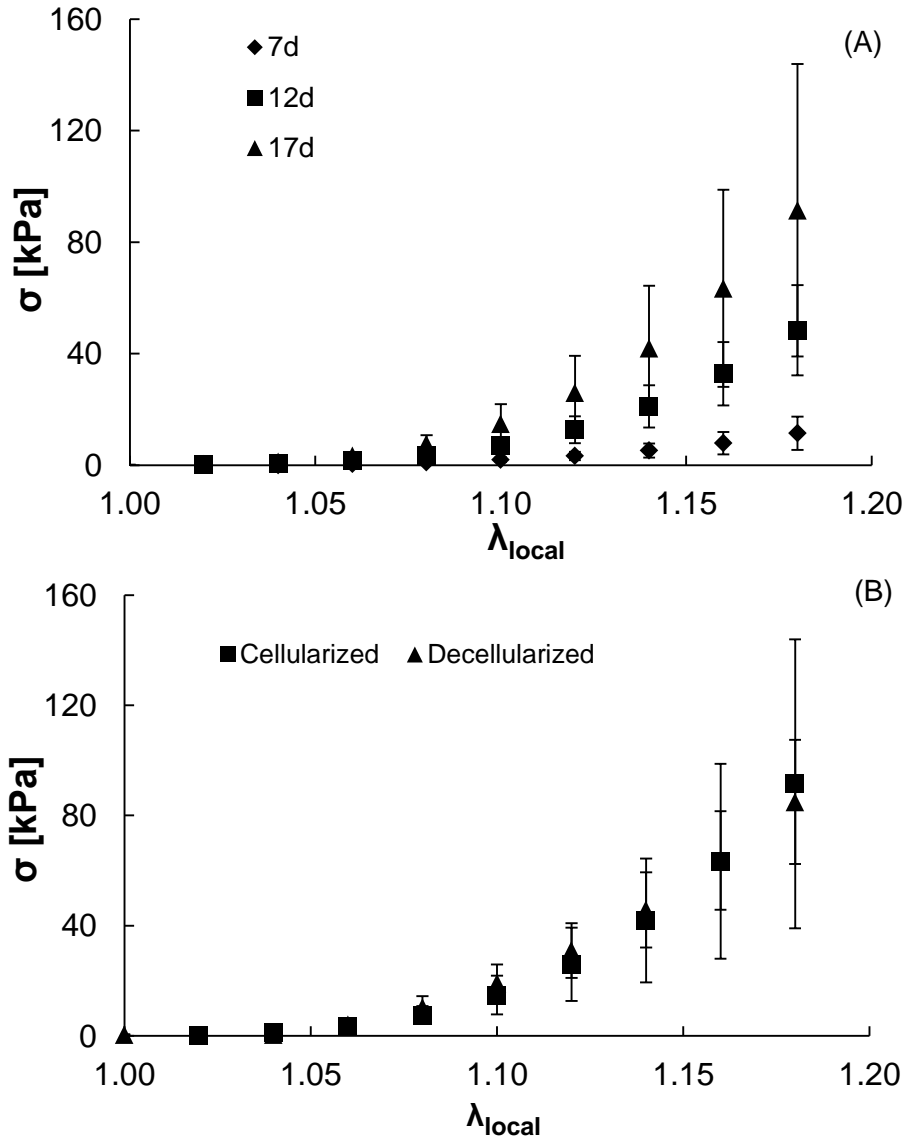


Figure 5.10. (A), Experimental stretch-stress responses (means \pm SE) of cellularized tissue constructs (n=5 tissue constructs from each culture period) and (B), Comparison of experimental stretch-stress responses (means \pm SE) of cellularized and decellularized 17 day constructs (n=5 for each)

It has been shown that native vascular tissues exhibit biphasic mechanical responses over the physiological loading range [173]. The elastin plays an important part in the mechanical response over low strain while collagen fibers make a significant contribution as they are gradually recruited with increasing strain [32, 174]. Focusing on the comparison in mechanical properties between native and synthetic soft tissue constructs, the elastic moduli of the low and high strain regions of the fabricated tissue constructs we tested were calculated separately. The Cauchy stress-stretch curves were divided into three regions: elastin-dominant and collagen-dominant phases between which is the transition region, of which the incremental elastic moduli were determined by linearizing the stress-stretch curves over the low and high strain regions respectively as shown in Figure 5.12. The calculated elastic moduli of elastin and collagen for both cellularized and decellularized tissue constructs range from approximately 10 to 1500 kPa (Table 5.2 and Figure 5.13). Statistical analysis is conducted to characterize the mechanical property dependence on culture time and decellularization process. The stiffness of the cellularized constructs was significantly increased with culture time. It showed that there was no significant difference between cellularized and decellularized constructs cultured for 17 days.

Ultimate tensile strength (UTS) was determined by recording the failure load as we increased the strain. It can be seen that the mean ultimate tensile strength of the cellularized samples increased significantly with culture time. A significant increase in ultimate tensile strength of decellularized samples between 7 and 17 days was observed yet insignificant difference between decellularized ones between 12 and 17 days (Figure 5.11).

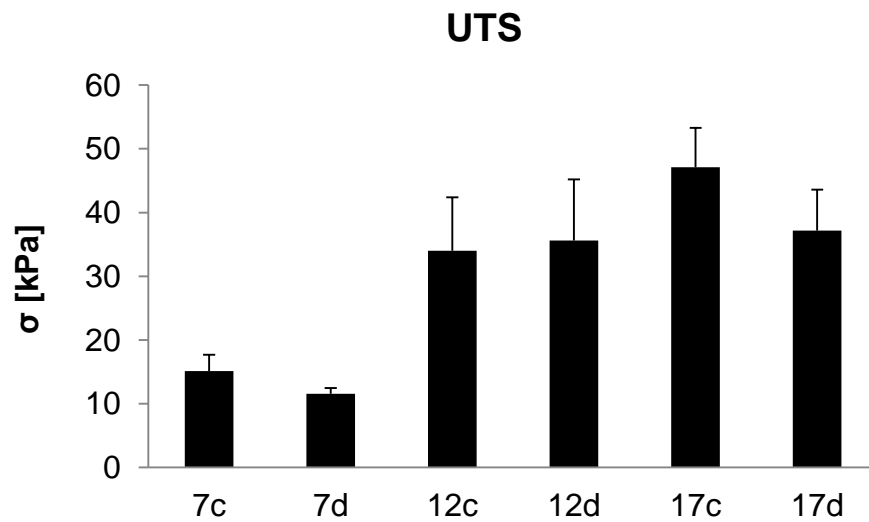


Figure 5.11. Comparison of ultimate tensile strength of cellularized and decellularized constructs.

Table 5.1. Incremental elastic moduli of cellularized and decellularized constructs.

Culture time	Cellularized		Decellularized	
	E(elastin) [kPa]	E(collagen) [kPa]	E(elastin) [kPa]	E(collagen) [kPa]
7 days	13.32 ± 8.09	38.52 ± 35.46	21.99 ± 12.89	151.62 ± 99.87
12 days	21.26 ± 16.99	289.03 ± 116.32	13.32 ± 8.09	38.52 ± 35.46
17 days	35.71 ± 15.43	873.35 ± 1143.86	59.57 ± 38.19	1442.13 ± 1318.97

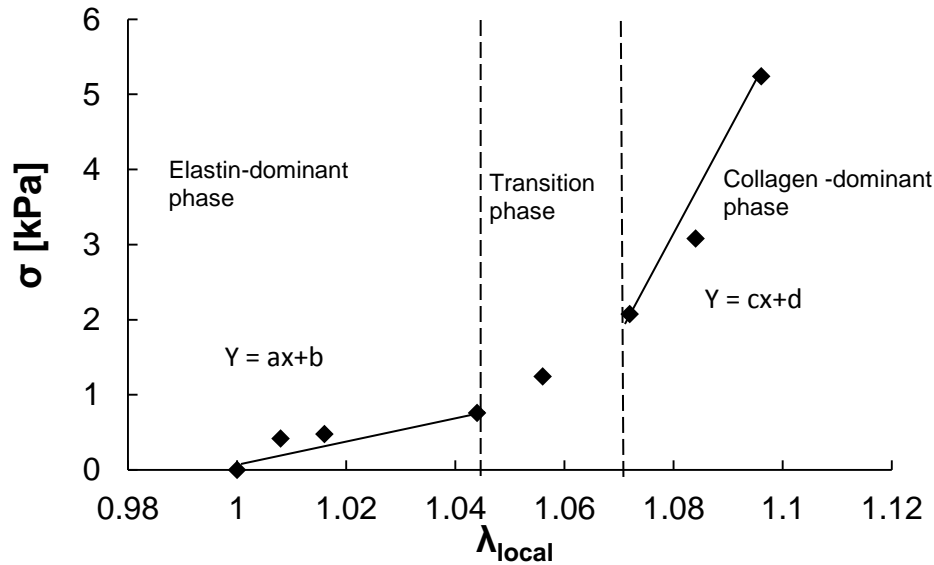


Figure 5.12. Cauchy stress-stretch consisting of elastin dominant, transition and collagen dominant phases of tissue constructs.

Day 12 cellularized ring samples on both 2 mm agarose posts in molds and PLA vertical posts of 2mm and 3 mm were compared to see whether circumferential conditioning affects the geometrical or mechanical properties of these constructs. The effects of culture environment and boundary conditions were examined by comparing specimens cultured on 2 mm PLA post with ones on 2 mm agarose molds, while influence of circumferential strain was tested by comparing the samples cultured on 3mm PLA posts with ones on 2 mm agarose molds and PLA posts. It showed that there was no significant statistical difference in geometry among different culture environments (Table 5.2 and Figure 5.13). Mechanical testing of statically stretched ring constructs and controls was conducted as mentioned in previous section. Linearized elastic moduli of elastin and collagen as well as ultimate tensile strength were shown in Table 5.3 and Figure 5.14.

Table 5.2. Geometric parameters of statically stretched specimens.

Material conditions	Outer diameter [mm]	Inner diameter [mm]	Thickness [mm]
2 mm agarose post	3.81 ± 0.17	2.37 ± 0.26	0.72 ± 0.09
2 mm PLA post	3.83 ± 0.22	1.89 ± 0.35	0.97 ± 0.19
3 mm PLA post	4.19 ± 0.3	2.42 ± 0.43	0.89 ± 0.22

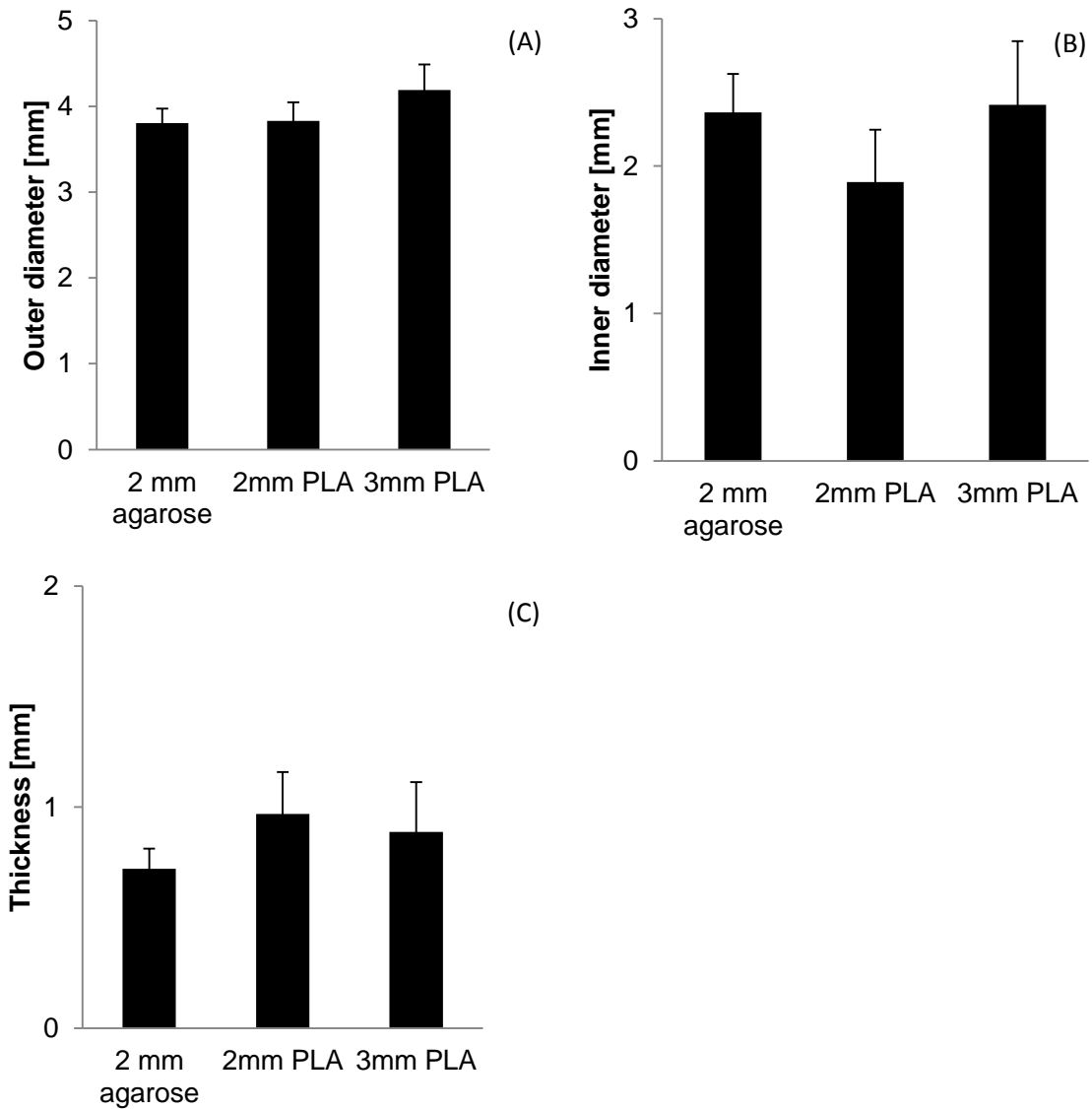


Figure 5.13. Comparison of outer diameter (A), inner diameter (B) and thickness (C) among different vascular constructs.

Table 5.3. Incremental Elastic moduli of elastin and collagen of unstretched and stretched cellularized constructs.

Material conditions	E (elastin) [kPa]	E (collagen) [kPa]	# of samples
Agarose 2 mm	21.26 ± 16.99	289.03 ± 116.32	5
Pre-stretched 2 mm	34.19 ± 23.46	223.94 ± 146.96	9
Pre-stretched 2.5 mm	34.1 ± 13.49	368.48 ± 155.22	6
Pre-stretched 3 mm	32.28 ± 10.81	395.67 ± 41.86	8

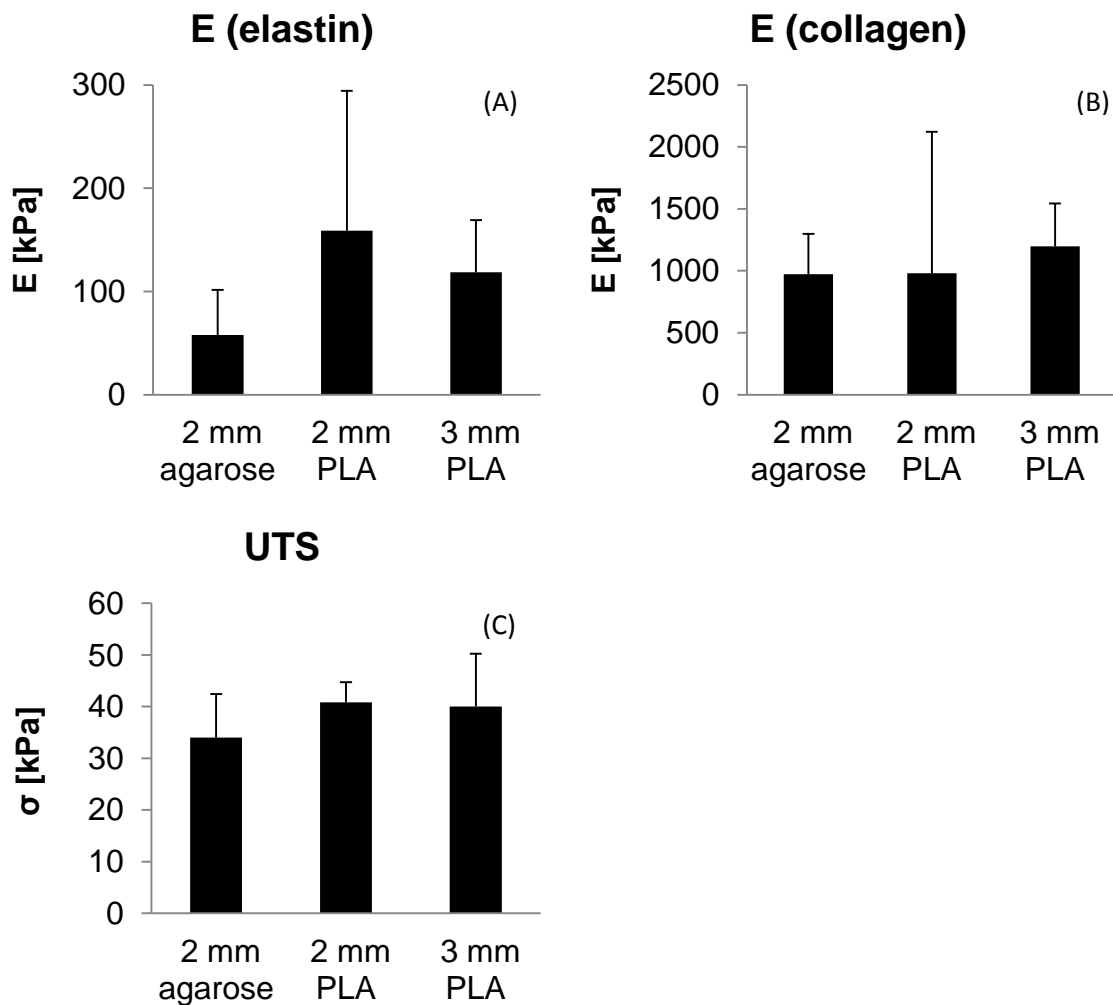


Figure 5.14. Comparison of incremental elastic moduli of elastin (A) and collagen (B) as well as comparison of ultimate tensile strength between agarose molds and stretched samples (C) among various fabricated constructs.

Burst pressure and geometry for all tissue engineered tube constructs are included in Table 5.4. The suture retention strength of our constructs had averaged to $1.89 \pm 0.01\text{N}$ (n=1, three tests per specimen).

Table 5.4. Burst pressure and geometry of tube.

Sample #	Burst pressure [mmHg]	Thickness [mm]	Outer diameter [mm]	Inner diameter [mm]	Length [mm]
1	64.30	1.30	4.10	1.50	25.50
2	76.50	0.90	2.64	0.82	14.18
3	62.40	1.10	3.66	1.40	15.76
4	66.80	1.05	4.29	2.19	18.12
5	28.90	1.14	4.42	2.14	18.19
AVG	59.78	1.10	3.82	1.61	18.35
STD	18.09	0.14	0.72	0.57	4.34

5.5 DISCUSSION

Here we demonstrate that cellularized gelatin macroporous microcarriers ('Cultispheres') can be used as self-adhering building blocks for the fabrication of tubular structures. The ability of cellularized Cultispheres to adhere to one another involved the formation of both cellular and extracellular matrix (ECM) bridging between microcarrier beads. Cellular bridges included cells occupying the inter-bead spaces as well as epithelium-like cell layers lining the luminal and abluminal surfaces of the tubular constructs.

A potential application of the cellularized microcarrier-based fabrication approach described here is in the manufacture of replacement blood vessels or other types of tubular structures damaged by injury or disease. Each year, hundreds of thousands of people undergo vein or artery replacement therapy; however, systemic vascular disease

often means that autologous replacement blood vessels are not available. Various approaches have been carried out to fabricate blood vessels [175-179]. One way is to use tubular scaffolds manufactured from natural and synthetic biomaterials seeded with vascular cells [178, 180-182]. Cellularized microcarrier-based fabrication is a cell-based approach to blood vessel construction that might permit synthesis of living prostheses having cellular composition and mechanical properties comparable to the walls of native blood vessels. In addition to the possibility of using the living microcarrier-based constructs directly, removal of cells from constructs may permit generation of acellular ECM scaffolds that could be used as biomaterials (e.g., off the-shelf tissue-engineered vascular scaffolds). The clinical applicability of microcarrier-based fabrication of living tubular constructs or vascular scaffolds will require that the cellular components be derived from a patient's own tissues.

The current study showed that uniaxial mechanical tests revealed evolving material properties of cellularized and decellularized tissue constructs. The findings indicate that construct stiffness increases with static culture time, and that the process of decellularization does not compromise the construct's mechanical properties. These findings suggest that manipulation of culture time is an effective constraint for achieving specific, desired mechanical properties for different applications. It also suggests that the decellularization process yielded an "off-the-shelf" tissue-engineered scaffold which can be stored at certain conditions for a period of time prior to implantation. Further studies that quantify the microstructure and constitutive modeling with appropriate models will provide a link between the microstructure and mechanics of tissue constructs.

The effect of static circumferential stretch was evaluated and it showed there was no significant difference in geometry and mechanical properties due to static inner circumferential strain. A few studies showed that tissue engineered vascular graft under dynamic flow conditions with better outcome in terms of cell proliferation and extracellular matrix production compared with static culture group [183-185]. Therefore, Additional research is needed to determine if biomechanical and biochemical properties of Cultispher tubes can be modified e.g., through application of cyclical strain or flow.

Engineered replacement blood vessels need to display strength and resiliency necessary to sustain mechanical integrity required for physiological levels of blood flow and vasoreactivity. In native arterial blood vessels collagens and elastin provide these properties [186-188]. Biomechanical testing of the rings generated from cellularized Cultisphers demonstrated mechanical behavior consistent with that of an isotropic, incompressible, homogeneous, elastic material, with a modulus of 52.2 ± 12.7 kPa in the steeper portion of the stress-strain curve. Through analysis of isolated insoluble elastin and elastin-rich tissues (e.g., bovine nuchal ligament), elastin has been shown to behave as a nearly linear elastic material with Young's modulus of roughly 400-800 kPa, depending on the tissue source and isolation procedures [189-192]. Biomaterials produced by cross-linking recombinant elastin polypeptides show similar behavior with a lower modulus of about 250 kPa [193]. More recent studies [194] suggest that aortic elastin shows some anisotropy in its material behavior, with axial stiffness being less than circumferential stiffness. The modulus of the Cultispher ring constructs is consistent with the lower end of the range reported by Zou and Zhang [188] for the axial tangent modulus of isolated aortic elastin at low strains. The relatively low stiffness of the

Cultispher rings suggests that the elastin present may not be highly cross-linked at the 7-day time point and that there is not a significant amount of mature cross-linked collagen.

Burst pressure and suture retention strength are key parameters determining a vessel's clinical feasibility for implantation. Several groups have reported results of TEBVs burst pressure up to 2000 mmHg [195-198]. The relatively low burst pressure showed in our study may attribute to the poorly cross-linked elastin in the constructs. It has been shown that the production of elastin and mechanical properties of tissue constructs depends largely on the pore size of the microcarriers [199]. The geometry of the test specimens in terms of inner diameter, thickness and length must also be considered. Due to Laplace's law, burst pressure increases linearly with decreasing diameter at constant thickness. Meanwhile, test specimen length may also play an important part in evaluating the burst pressure. Variation in mechanical strength throughout the length of a TEBV for clinical use may not be reflected from a 2 cm long segment. Several factors such as bite depth, suture thickness and the number of sutures will affect the suture retention strength.

5.6 STUDY LIMITATIONS

Simplifying assumptions are made to completely describe the mechanical properties of fabricated tissue engineered constructs. Firstly, constructs are regarded as elastic materials under physiological loads, although they are probably viscoelastic. There is need to conduct stress-relaxation tests on the samples to investigate the viscoelastic mechanical behaviors of constructs. Secondly, assumption of material homogeneity was introduced to facilitate modeling mechanical properties of fabricated tissue engineered constructs, but local variations of compositions may grant the material with certain

degree of inhomogeneity. Further experimental studies are required to quantify the extent of orthotropic inhomogeneity.

5.7 CONCLUSIONS

Fabricated vascular tissue constructs has the potential for autologous transplants. In this work ring shaped constructs formed by self-adhering microcarrier beads seeded with human umbilical vein endothelial cells and vascular smooth muscle cells were characterized via the uniaxial tensile test while stacked tubes were mechanically quantified via burst pressure and suture retention tests, providing a basis for future rational design of vascular tissue constructs. Cauchy stress-stretch relationship of ring-shaped Cultispher constructs generated from experimental data in the uniaxial tensile test exhibits nonlinear elastic mechanical behavior, with progressive stiffening at higher stretch ratios. Incremental elastic moduli of low and high strain regions were determined by biphasically analyzing the Cauchy stress-stretch curves, demonstrating that the stiffness of both elastin and collagen increased with culture time. By comparing the mechanical properties of cellularized and decellularized constructs cultured for 17 days, it showed that decellularization process does not compromise material mechanical integrity, suggesting potential application of “off the shelf” tissue constructs. Preliminary results of burst pressure and suture retention strength of stacked tube cultured for 27 days showed the potentiality of this novel fabrication approach. Mechanical information from this study will help us improve the graft development and facilitate structure design and analysis to meet specific requirements of clinical use.

CHAPTER 6

CONCLUSION

6.1 DISSERTATION SUMMARY

The overall goal of this study was to investigate the mechanical properties of native and fabricated vascular tissues which can help select the optimal autologous vascular grafts and improve the manufacturing process of engineering vascular substitutes.

With regard to the native vascular tissues the specific aim was to quantify the contribution of the passive structural components to the mechanical behavior of the primary renal artery. The findings of this study can be summarized as follows:

The primary renal artery exhibits a canonical nonlinear elastic mechanical response within the range of physiological loads.

A four-fiber family structure-motivated strain energy function was able to model the mechanical behavior of the primary renal artery. This model was used to predict the circumferential stress distribution across the vessel wall under physiological loading conditions.

With regard to the vasoactivity of the native vascular tissue the specific aim was to characterize the biaxial mechanical effects of smooth muscle cell contraction within the renal arterial wall. The findings of this study can be summarized as follows

The mechanical response of the primary renal artery is qualitatively and quantitatively different between maximally contracted and fully relaxed VSMCs states. The VSMCs contraction significantly increased the stiffness of primary renal artery.

The proposed analytical expressions incorporating biaxial VSMCs contraction were able to accurately model the derived active circumferential and axial stress-strain relationships.

The mechanical properties of candidate vessels and tissue engineering vascular substitutes were investigated in the context of vascular graft application.

The specific aim of this study with respect to autologous vascular grafts was to investigate the passive mechanical and structural properties of various blood vessels and predict their mechanical compatibility in the context of forming end-to-end vascular grafts in the coronary artery. The findings of this study are as follows:

ITA was shown to be the most mechanically compatible autologous vascular graft for coronary artery based on the normalized comparison of compliance, deformed inner radius and vessel wall stresses between graft and host artery under grafted loading conditions.

Plausible alteration of the axial stretch of an autologous vascular graft significantly impacts its mechanical compatibility and there is an optimal value for each kind of grafted vessel.

With respect to tissue engineered vascular substitutes the specific aim was to quantify the mechanical response of fabricated vascular tissue constructs in a uniaxial tensile as well as burst pressure and suture retention experiments. The main findings of this study in this context are as follows:

Mechanical responses of fabricated vascular tissue constructs were nonlinear and the mechanical properties attributed to the loading-bearing structural constituents increased with culture time.

Detergent-based decellularization process did not compromise the mechanical integrity of fabricated vascular constructs.

Current limitations in the treatments of CVD provide impetus for the development of tissue engineered constructs to replace compromised vascular tissues. Because vascular cells sense and respond to the local mechanical environment, promoting normal phenotype within engineered constructs will depend on the extent to which these mimic native arterial behavior in the regime defined by physiological loads. Logically, knowledge of baseline native vascular mechanics, particularly the stresses experienced by vascular cells, is required to develop tissue engineered constructs that recapitulate the mechanical environment within the healthy arterial wall.

6.2 FUTURE STUDIES

Prediction of stress-induced remodeling of grafted vessels

Based on the comparisons in mechanical properties between grafted vessel and host artery, it will be interesting to investigate how to reduce their mechanical discrepancy so as to increase the patency of grafts. One possible solution is to culture the potential graft under specific mechanical conditions prior to implantation for a certain period of time, inducing tissue growth and remodeling in terms of smooth muscle proliferation and extracellular matrix production. Direct boundary value problem can be solved using parameters associated with structure-based constitutive models, initial stress-free configuration, dry mass fraction of elastin, collagen and vascular smooth

muscle cells, results of which can predict ultimate outcomes from stress-induced growth and remodeling.

Inverse and direct boundary value approach for characterizing tissue engineered vascular grafts

For some mechanically isotropic materials, data from the uniaxial tensile experiment can be processed to identify the constitutive stress-strain relationships in terms of strain energy function (SEF), the parameters of which can be used to predict a three-dimensional response of an internally pressurized thick-walled tube fabricated from this material. Verification of the proposed SEF can be achieved through comparison of the predicted and experimental pressure-diameter response of the fabricated tube. Preliminary results showed the predictability of single-invariant constitutive model on the biaxial mechanical response of cellularized constructs with various culture time (Figure 7.1). Given adherent endothelial cells and smooth muscle cells within Cultispheres are mechanically sensitive, knowledge of the SEF and constitutive equations for this material will facilitate calculating stress-strain relationship of arterial substitutes under physiological loads and evaluating its performance.

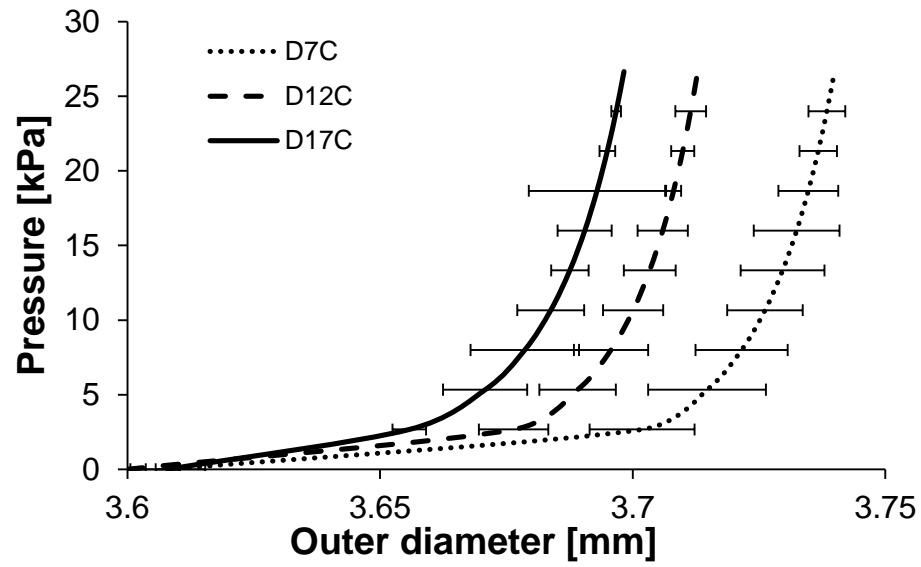


Figure 7.1. Predicted pressure-outer diameter relationships of cellularized constructs at various culture time.

BIBLIOGRAPHY

1. O'Gara, P.T., et al., *2013 ACCF/AHA Guideline for the Management of ST-Elevation Myocardial Infarction A Report of the American College of Cardiology Foundation/American Heart Association Task Force on Practice Guidelines*. Journal of the American College of Cardiology, 2013. **61**(4): p. e78-e140.
2. London, G.M., et al., *Arterial structure and function in end-stage renal disease*. Nephrology Dialysis Transplantation, 2002. **17**(10): p. 1713-1724.
3. Jensen, G., et al., *[Renal artery stenosis--an underestimated cause of hypertension and renal failure?]*. Lakartidningen, 1998. **95**(38): p. 4068, 4071-4.
4. *What is atherosclerosis*. 2011; Available from: <http://www.nhlbi.nih.gov/health/health-topics/topics/atherosclerosis/>.
5. Cheung, C.M., J. Hegarty, and P.A. Kalra, *Dilemmas in the management of renal artery stenosis*. British Medical Bulletin, 2005. **73-74**(1): p. 35-55.
6. Cioni, R., et al., *Renal artery stenting in patients with a solitary functioning kidney*. Cardiovasc Intervent Radiol, 2001. **24**(6): p. 372-7.
7. Cooper, C.J., et al., *Stent revascularization for the prevention of cardiovascular and renal events among patients with renal artery stenosis and systolic hypertension: rationale and design of the CORAL trial*. Am Heart J, 2006. **152**(1): p. 59-66.
8. Harden, P.N., et al., *Effect of renal-artery stenting on progression of renovascular renal failure*. Lancet, 1997. **349**(9059): p. 1133-6.
9. Jensen, G., et al., *Treatment of renovascular hypertension: one year results of renal angioplasty*. Kidney Int, 1995. **48**(6): p. 1936-45.
10. Joffre, F., et al., *[Usefulness of a percutaneous endoprosthesis in the treatment of renal artery stenoses]*. Arch Mal Coeur Vaiss, 1989. **82**(7): p. 1199-204.
11. Gruntzig, A., et al., *Treatment of renovascular hypertension with percutaneous transluminal dilatation of a renal-artery stenosis*. Lancet, 1978. **1**(8068): p. 801-2.
12. Leertouwer, T.C., et al., *Stent placement for renal arterial stenosis: where do we stand? A meta-analysis*. Radiology, 2000. **216**(1): p. 78-85.
13. *Arterial and venous conduits for coronary artery bypass. A current review*. European Journal of Cardio-Thoracic Surgery, 1996. **10**(2): p. 129-140.
14. Chamiot-Clerc, P., et al., *Comparative reactivity and mechanical properties of human isolated internal mammary and radial arteries*. Cardiovasc Res, 1998. **37**(3): p. 811-9.
15. Dignan, R.J., et al., *The influence of age and sex on human internal mammary artery size and reactivity*. Ann Thorac Surg, 1992. **53**(5): p. 792-7.
16. Lytle, B.W., et al., *Long-term (5 to 12 years) serial studies of internal mammary artery and saphenous vein coronary bypass grafts*. J Thorac Cardiovasc Surg, 1985. **89**(2): p. 248-58.
17. van der Meer, J., et al., *A comparison of internal mammary artery and saphenous vein grafts after coronary artery bypass surgery. No difference in 1-year occlusion rates and clinical outcome. CABADAS Research Group of the Interuniversity Cardiology Institute of The Netherlands*. Circulation, 1994. **90**(5): p. 2367-74.

18. Al-Sabti, H.A., et al., *Saphenous vein graft vs. radial artery graft searching for the best second coronary artery bypass graft*. Journal of the Saudi Heart Association, 2013. **25**(4): p. 247-254.9. Shapira, O.M., et al., *Enhanced Nitric Oxide-Mediated Vascular Relaxation in Radial Artery Compared With Internal Mammary Artery or Saphenous Vein*. Circulation, 1999. **100**(suppl 2): p. II-322-Ii-327.
20. *Bypass surgery*. Available from: http://my.clevelandclinic.org/services/heart/disorders/treatment_heart surg.
21. Chuong, C.J. and Y.C. Fung, *On residual stresses in arteries*. J Biomech Eng, 1986. **108**(2): p. 189-92.
22. Cox, R.H., *Anisotropic properties of the canine carotid artery in vitro*. Journal of Biomechanics. **8**(5): p. 293-300.
23. Davis, R.P., et al., *Atherosclerotic renovascular disease among hypertensive adults*. J Vasc Surg, 2009. **50**(3): p. 564-570, 571.e1-3; discussion 571.
24. Edwards, M.S. and M.A. Corriere, *Contemporary management of atherosclerotic renovascular disease*. J Vasc Surg, 2009. **50**(5): p. 1197-210.
25. FISCHER, G.M. and J.G. LLAURADO, *Collagen and Elastin Content in Canine Arteries Selected from Functionally Different Vascular Beds*. Circulation Research, 1966. **19**(2): p. 394-399.
26. Naito, Y., et al., *Vascular tissue engineering: towards the next generation vascular grafts*. Adv Drug Deliv Rev, 2011. **63**(4-5): p. 312-23.
27. Swartz, D.D., J.A. Russell, and S.T. Andreadis, *Engineering of fibrin-based functional and implantable small-diameter blood vessels*. Am J Physiol Heart Circ Physiol, 2005. **288**(3): p. H1451-60.
28. Hibino, N., et al., *Late-term results of tissue-engineered vascular grafts in humans*. J Thorac Cardiovasc Surg, 2010. **139**(2): p. 431-6, 436.e1-2.
29. Buttafoco, L., et al., *Physical characterization of vascular grafts cultured in a bioreactor*. Biomaterials, 2006. **27**(11): p. 2380-9.
30. KIELTY, C.M., et al., *Applying elastic fibre biology in vascular tissue engineering*. Philos Trans R Soc Lond B Biol Sci, 2007. **362**(1484): p. 1293-312.
31. *TEBV*. Available from: http://openwetware.org/wiki/Tissue_Engineered_Vascular_Grafts_by_Tyler_Vlass_and_Emily_Brackett.
32. Roach, M.R. and A.C. Burton, *The reason for the shape of the distensibility curves of arteries*. Can J Biochem Physiol, 1957. **35**(8): p. 681-90.
33. Liu, S.Q. and Y.C. Fung, *Relationship between hypertension, hypertrophy, and opening angle of zero-stress state of arteries following aortic constriction*. J Biomech Eng, 1989. **111**(4): p. 325-35.
34. Vito, R.P. and S.A. Dixon, *Blood vessel constitutive models-1995-2002*. Annu Rev Biomed Eng, 2003. **5**: p. 413-39.
35. Matsumoto, T. and K. Hayashi, *Stress and strain distribution in hypertensive and normotensive rat aorta considering residual strain*. J Biomech Eng, 1996. **118**(1): p. 62-73.
36. Wright, J.R., et al., *Progression of cardiac dysfunction in patients with atherosclerotic renovascular disease*. QJM, 2009. **102**(10): p. 695-704.
37. Cox, R.H., *Arterial wall mechanics and composition and the effects of smooth muscle activation*. Am J Physiol, 1975. **229**(3): p. 807-12.
38. Cox, R.H., *Regional variation of series elasticity in canine arterial smooth muscles*. Am J Physiol, 1978. **234**(5): p. H542-51.
39. Dobrin, P.B. and J.M. Doyle, *Vascular smooth muscle and the anisotropy of dog carotid artery*. Circ Res, 1970. **27**(1): p. 105-19.

40. Dobrin, P.B. and A.A. Rovick, *Influence of vascular smooth muscle on contractile mechanics and elasticity of arteries*. Am J Physiol, 1969. **217**(6): p. 1644-51.
41. Dobrin, P.B., *Isometric and isobaric contraction of carotid arterial smooth muscle*. Am J Physiol, 1973. **225**(3): p. 659-63.
42. Dobrin, P.B., *Vascular muscle series elastic element stiffness during isometric contraction*. Circ Res, 1974. **34**(2): p. 242-50.
43. Dajnowiec, D. and B.L. Langille, *Arterial adaptations to chronic changes in haemodynamic function: coupling vasomotor tone to structural remodelling*. Clin Sci (Lond), 2007. **113**(1): p. 15-23.
44. Fridez, P., et al., *Adaptation of conduit artery vascular smooth muscle tone to induced hypertension*. Ann Biomed Eng, 2002. **30**(7): p. 905-16.
45. Fridez, P., et al., *Short-Term biomechanical adaptation of the rat carotid to acute hypertension: contribution of smooth muscle*. Ann Biomed Eng, 2001. **29**(1): p. 26-34.
46. Fridez, P., et al., *Model of geometrical and smooth muscle tone adaptation of carotid artery subject to step change in pressure*. Am J Physiol Heart Circ Physiol, 2001. **280**(6): p. H2752-60.
47. Zulliger, M.A., A. Rachev, and N. Stergiopoulos, *A constitutive formulation of arterial mechanics including vascular smooth muscle tone*. Am J Physiol Heart Circ Physiol, 2004. **287**(3): p. H1335-43.
48. Rachev, A. and S.E. Greenwald, *Residual strains in conduit arteries*. J Biomech, 2003. **36**(5): p. 661-70.
49. Hillege, H., et al., *Renal function as a predictor of prognosis in chronic heart failure*. Heart Fail Monit, 2002. **2**(3): p. 78-84.
50. Kamiya, A. and T. Togawa, *Adaptive regulation of wall shear stress to flow change in the canine carotid artery*. Am J Physiol, 1980. **239**(1): p. H14-21.
51. Rachev, A., *Remodeling of Arteries in Response to Changes in their Mechanical Environment*, in *Biomechanics of Soft Tissue in Cardiovascular Systems*, G. Holzapfel and R. Ogden, Editors. 2003, Springer Vienna. p. 221-271.
52. Gleason, R.L. and J.D. Humphrey, *A mixture model of arterial growth and remodeling in hypertension: altered muscle tone and tissue turnover*. J Vasc Res, 2004. **41**(4): p. 352-63.
53. PETERSON, L.H., R.E. JENSEN, and J. PARNELL, *Mechanical Properties of Arteries in Vivo*. Circulation Research, 1960. **8**(3): p. 622-639.
54. Adamczak, M. and A. Wiecek, *The management of atherosclerotic renovascular disease*. Kidney Blood Press Res, 2011. **34**(4): p. 277-83.
55. Carboni, M., G.W. Desch, and H.W. Weizsäcker, *Passive mechanical properties of porcine left circumflex artery and its mathematical description*. Medical Engineering & Physics, 2007. **29**(1): p. 8-16.
56. Cheung, C.M., et al., *Epidemiology of renal dysfunction and patient outcome in atherosclerotic renal artery occlusion*. J Am Soc Nephrol, 2002. **13**(1): p. 149-57.
57. Chrysochou, C. and P.A. Kalra, *Current management of atherosclerotic renovascular disease--what have we learned from ASTRAL?* Nephron Clin Pract, 2010. **115**(1): p. c73-81.
58. Gandle, R.E., et al., *Intrinsic tone and passive mechanics of isolated renal arteries from virgin and late-pregnant rats*. Am J Physiol, 1997. **273**(1 Pt 2): p. R22-7.
59. Garcia, A., et al., *Experimental study and constitutive modelling of the passive mechanical properties of the porcine carotid artery and its relation to histological analysis: Implications in animal cardiovascular device trials*. Med Eng Phys, 2011. **33**(6): p. 665-76.
60. Holzapfel, G., T. Gasser, and R. Ogden, *A New Constitutive Framework for Arterial Wall Mechanics and a Comparative Study of Material Models*. Journal of elasticity and the physical science of solids, 2000. **61**(1-3): p. 1-48.

61. Valentin, A. and J.D. Humphrey, *Modeling effects of axial extension on arterial growth and remodeling*. Med Biol Eng Comput, 2009. **47**(9): p. 979-87.
62. Humphrey, J.D., et al., *Fundamental role of axial stress in compensatory adaptations by arteries*. J Biomech, 2009. **42**(1): p. 1-8.
63. Zulliger, M.A., G. Montorzi, and N. Stergiopoulos, *Biomechanical adaptation of porcine carotid vascular smooth muscle to hypo and hypertension in vitro*. J Biomech, 2002. **35**(6): p. 757-65.
64. Humphrey, J.D., *Vascular Mechanics, Mechanobiology, and Remodeling*. J Mech Med Biol, 2009. **9**(2): p. 243-257.
65. Tsamis, A., A. Rachev, and N. Stergiopoulos, *A constituent-based model of age-related changes in conduit arteries*. Am J Physiol Heart Circ Physiol. **301**(4): p. H1286-301.
66. Wayman, B.H., et al., *Arteries respond to independent control of circumferential and shear stress in organ culture*. Ann Biomed Eng, 2008. **36**(5): p. 673-84.
67. Steelman, S.M. and J.D. Humphrey, *Differential remodeling responses of cerebral and skeletal muscle arterioles in a novel organ culture system*. Med Biol Eng Comput. **49**(9): p. 1015-23.
68. Tian, L., et al., *Linked opening angle and histological and mechanical aspects of the proximal pulmonary arteries of healthy and pulmonary hypertensive rats and calves*. Am J Physiol Heart Circ Physiol. **301**(5): p. H1810-8.
69. Stapleton, P.A., et al., *Differential impact of familial hypercholesterolemia and combined hyperlipidemia on vascular wall and network remodeling in mice*. Microcirculation. **17**(1): p. 47-58.
70. Rizzoni, D., et al., *Vascular remodeling, macro- and microvessels: therapeutic implications*. Blood Press, 2009. **18**(5): p. 242-6.
71. Mekkaoui, C., et al., *Simultaneous measurements of arterial diameter and blood pressure to determine the arterial compliance, wall mechanics and stresses in vivo*. Eur J Vasc Endovasc Surg, 2001. **21**(3): p. 208-13.
72. Martin, C., T. Pham, and W. Sun, *Significant differences in the material properties between aged human and porcine aortic tissues*. Eur J Cardiothorac Surg, 2011. **40**(1): p. 28-34.
73. Humphrey, J.D., *Cardiovascular Solid Mechanics: Cells, Tissues, and Organs*. 2002: Lightning Source, UK Ltd.
74. Langille, B.L., *Blood Flow-Induced Remodeling of the Artery Wall*, in *Flow-Dependent Regulation of Vascular Function*, J. Bevan, G. Kaley, and G. Rubanyi, Editors. 1995, Springer New York. p. 277-299.
75. Hull, S.S., Jr., et al., *Endothelium-dependent flow-induced dilation of canine femoral and saphenous arteries*. Blood Vessels, 1986. **23**(4-5): p. 183-98.
76. Moncada, S., R.M. Palmer, and E.A. Higgs, *Nitric oxide: physiology, pathophysiology, and pharmacology*. Pharmacol Rev, 1991. **43**(2): p. 109-42.
77. Silverthorn, D.U.J.B.R., *Human physiology : an integrated approach*. 2010, San Francisco: Pearson/Benjamin Cummings.
78. Stalhand, J., A. Klarbring, and G.A. Holzapfel, *A mechanochemical 3D continuum model for smooth muscle contraction under finite strains*. J Theor Biol, 2011. **268**(1): p. 120-30.
79. Gaballa, M.A., et al., *Large artery remodeling during aging: biaxial passive and active stiffness*. Hypertension, 1998. **32**(3): p. 437-43.
80. Dobrin, P.B., *Influence of initial length on length-tension relationship of vascular smooth muscle*. Am J Physiol, 1973. **225**(3): p. 664-70.
81. Dobrin, P.B., *Mechanical behavior of vascular smooth muscle in cylindrical segments of arteries in vitro*. Ann Biomed Eng, 1984. **12**(5): p. 497-510.

82. Rachev, A. and K. Hayashi, *Theoretical study of the effects of vascular smooth muscle contraction on strain and stress distributions in arteries*. Ann Biomed Eng, 1999. **27**(4): p. 459-68.
83. Huo, Y., et al., *Biaxial vasoactivity of porcine coronary artery*. Am J Physiol Heart Circ Physiol, 2012. **302**(10): p. H2058-63.
84. Huo, Y., et al., *Two-layer model of coronary artery vasoactivity*. J Appl Physiol (1985), 2013. **114**(10): p. 1451-9.
85. Kroon, M., *A constitutive model for smooth muscle including active tone and passive viscoelastic behaviour*. Math Med Biol, 2010. **27**(2): p. 129-55.
86. Humphrey, J.D. and E. Wilson, *A potential role of smooth muscle tone in early hypertension: a theoretical study*. J Biomech, 2003. **36**(11): p. 1595-601.
87. Valentin, A., et al., *Complementary vasoactivity and matrix remodelling in arterial adaptations to altered flow and pressure*. J R Soc Interface, 2009. **6**(32): p. 293-306.
88. Wagner, H.P. and J.D. Humphrey, *Differential passive and active biaxial mechanical behaviors of muscular and elastic arteries: basilar versus common carotid*. J Biomech Eng, 2011. **133**(5): p. 051009.
89. Agianniotis, A., A. Rachev, and N. Stergiopoulos, *Active axial stress in mouse aorta*. J Biomech, 2012. **45**(11): p. 1924-7.
90. Takamizawa, K., K. Hayashi, and T. Matsuda, *Isometric biaxial tension of smooth muscle in isolated cylindrical segments of rabbit arteries*. Am J Physiol, 1992. **263**(1 Pt 2): p. H30-4.
91. Cox, R.H., *Mechanics of canine iliac artery smooth muscle in vitro*. Am J Physiol, 1976. **230**(2): p. 462-70.
92. Pascale, K. and H.W. Weizsacker, *In situ study of active and passive mechanical properties of rat tail artery*. Basic Res Cardiol, 1987. **82**(1): p. 66-73.
93. Matsumoto, T., M. Tsuchida, and M. Sato, *Change in intramural strain distribution in rat aorta due to smooth muscle contraction and relaxation*. Am J Physiol, 1996. **271**(4 Pt 2): p. H1711-6.
94. Cardamone, L., et al., *Origin of axial prestretch and residual stress in arteries*. Biomech Model Mechanobiol, 2009. **8**(6): p. 431-46.
95. Toda, N., Y. Hatano, and S. Hayashi, *Modifications by stretches of the mechanical response of isolated cerebral and extracerebral arteries to vasoactive agents*. Pflugers Arch, 1978. **374**(1): p. 73-7.
96. Sparks, H.V. and D.F. Bohr, *Effect of stretch on passive tension and contractility of isolated vascular smooth muscle*. Vol. 202. 1962. 835-840.
97. Diamond, S.L., et al., *Tissue plasminogen activator messenger RNA levels increase in cultured human endothelial cells exposed to laminar shear stress*. J Cell Physiol, 1990. **143**(2): p. 364-71.
98. Humphrey, J.D., *Cardiovascular solid mechanics : cells, tissues, and organs*. 2002, New York: Springer. xvi, 757 p.
99. Wan, W., H. Yanagisawa, and R.L. Gleason, Jr., *Biomechanical and microstructural properties of common carotid arteries from fibulin-5 null mice*. Ann Biomed Eng, 2010. **38**(12): p. 3605-17.
100. Valentin, A., J.D. Humphrey, and G.A. Holzapfel, *A multi-layered computational model of coupled elastin degradation, vasoactive dysfunction, and collagenous stiffening in aortic aging*. Ann Biomed Eng, 2011. **39**(7): p. 2027-45.
101. Briet, M., et al., *Arterial stiffness and pulse pressure in CKD and ESRD*. Kidney Int, 2012. **82**(4): p. 388-400.
102. Chen, H., et al., *Microstructural constitutive model of active coronary media*. Biomaterials, 2013. **34**(31): p. 7575-83.

103. Perera, G.B., et al., *Superiority of autogenous arteriovenous hemodialysis access: maintenance of function with fewer secondary interventions*. *Ann Vasc Surg*, 2004. **18**(1): p. 66-73.
104. Canver, C.C., *Conduit options in coronary artery bypass surgery*. *Chest*, 1995. **108**(4): p. 1150-5.
105. Members, W.C., et al., *2011 ACCF/AHA Guideline for Coronary Artery Bypass Graft Surgery: A Report of the American College of Cardiology Foundation/American Heart Association Task Force on Practice Guidelines*. *Circulation*, 2011. **124**(23): p. e652-e735.
106. Canham, P.B., H.M. Finlay, and D.R. Boughner, *Contrasting structure of the saphenous vein and internal mammary artery used as coronary bypass vessels*. *Cardiovascular Research*, 1997. **34**(3): p. 557-567.
107. Dobrin, P., et al., *Coronary artery bypass. The physiological basis for differences in flow with internal mammary artery and saphenous vein grafts*. *J Thorac Cardiovasc Surg*, 1977. **74**(3): p. 445-54.
108. van Son, J.A., et al., *Histological study of the internal mammary artery with emphasis on its suitability as a coronary artery bypass graft*. *Ann Thorac Surg*, 1993. **55**(1): p. 106-13.
109. Shapira, O.M., et al., *Enhanced nitric oxide-mediated vascular relaxation in radial artery compared with internal mammary artery or saphenous vein*. *Circulation*, 1999. **100**(19 Suppl): p. Ii322-7.
110. de Dios, S.T., et al., *Inhibitory Activity of Clinical Thiazolidinedione Peroxisome Proliferator Activating Receptor- γ Ligands Toward Internal Mammary Artery, Radial Artery, and Saphenous Vein Smooth Muscle Cell Proliferation*. *Circulation*, 2003. **107**(20): p. 2548-2550.
111. Carpentier, A., et al., *The aorta-to-coronary radial artery bypass graft. A technique avoiding pathological changes in grafts*. *Ann Thorac Surg*, 1973. **16**(2): p. 111-21.
112. Tranbaugh, R.F., et al., *Coronary Artery Bypass Grafting Using the Radial Artery: Clinical Outcomes, Patency, and Need for Reintervention*. *Circulation*, 2012. **126**(11 suppl 1): p. S170-S175.
113. Milroy, C.M., et al., *Histological appearances of the long saphenous vein*. *J Pathol*, 1989. **159**(4): p. 311-6.
114. Catalano, M., et al., *Elastic properties and structure of the radial artery in patients with type 2 diabetes*. *Diab Vasc Dis Res*, 2009. **6**(4): p. 244-8.
115. Laurent, S., et al., *Elastic modulus of the radial artery wall material is not increased in patients with essential hypertension*. *Arteriosclerosis, Thrombosis, and Vascular Biology*, 1994. **14**(7): p. 1223-31.
116. Burton, A.C., *Relation of Structure to Function of the Tissues of the Wall of Blood Vessels*. Vol. 34. 1954. 619-642.
117. Wolinsky, H. and S. Glagov, *STRUCTURAL BASIS FOR THE STATIC MECHANICAL PROPERTIES OF THE AORTIC MEDIA*. *Circ Res*, 1964. **14**: p. 400-13.
118. Cox, R.H., *Passive mechanics and connective tissue composition of canine arteries*. *Am J Physiol*, 1978. **234**(5): p. H533-41.
119. Gusic, R.J., et al., *Mechanical properties of native and ex vivo remodeled porcine saphenous veins*. *J Biomech*, 2005. **38**(9): p. 1770-9.
120. Mavrilas, D., et al., *DYNAMIC MECHANICAL PROPERTIES OF ARTERIAL AND VENOUS GRAFTS USED IN CORONARY BYPASS SURGERY*. *Journal of Mechanics in Medicine and Biology*, 2002. **02**(03n04): p. 329-337.
121. Abbott, W.M., et al., *Effect of compliance mismatch on vascular graft patency*. *J Vasc Surg*, 1987. **5**(2): p. 376-82.
122. Walden, R., et al., *Matched elastic properties and successful arterial grafting*. *Arch Surg*, 1980. **115**(10): p. 1166-9.

123. Salacinski, H.J., et al., *The mechanical behavior of vascular grafts: a review*. J Biomater Appl, 2001. **15**(3): p. 241-78.
124. Ku, D.N., et al., *Pulsatile flow and atherosclerosis in the human carotid bifurcation. Positive correlation between plaque location and low oscillating shear stress*. Arteriosclerosis, 1985. **5**(3): p. 293-302.
125. He, X. and D.N. Ku, *Pulsatile flow in the human left coronary artery bifurcation: average conditions*. J Biomech Eng, 1996. **118**(1): p. 74-82.
126. Weston, M.W., K. Rhee, and J.M. Tarbell, *Compliance and diameter mismatch affect the wall shear rate distribution near an end-to-end anastomosis*. J Biomech, 1996. **29**(2): p. 187-98.
127. Durrani, A., E.K. Sim, and R.T. Grignani, *Accurate length adjustment of aortocoronary saphenous vein bypass grafts*. Ann Thorac Surg, 1998. **66**(3): p. 966-7.
128. Rachev, A., S. Greenwald, and T. Shazly, *Are geometrical and structural variations along the length of the aorta governed by a principle of "optimal mechanical operation"?* J Biomech Eng, 2013. **135**(8): p. 81006.
129. Rachev, A., N. Stergiopoulos, and J.J. Meister, *A model for geometric and mechanical adaptation of arteries to sustained hypertension*. J Biomech Eng, 1998. **120**(1): p. 9-17.
130. Eberth, J.F., et al., *Importance of pulsatility in hypertensive carotid artery growth and remodeling*. J Hypertens, 2009. **27**(10): p. 2010-21.
131. Fung, Y.C., *What are the residual stresses doing in our blood vessels?* Ann Biomed Eng, 1991. **19**(3): p. 237-49.
132. van der Meer, J., et al., *A comparison of internal mammary artery and saphenous vein grafts after coronary artery bypass surgery. No difference in 1-year occlusion rates and clinical outcome*. CABADAS Research Group of the Interuniversity Cardiology Institute of The Netherlands. Circulation, 1994. **90**(5): p. 2367-74.
133. Grande, J.P., et al., *Effect of normolipemic and hyperlipemic serum on biosynthetic response to cyclic stretching of aortic smooth muscle cells*. Arteriosclerosis, 1989. **9**(4): p. 446-52.
134. Dartsch, P.C. and H. Hammerle, *Orientation response of arterial smooth muscle cells to mechanical stimulation*. Eur J Cell Biol, 1986. **41**(2): p. 339-46.
135. Einav, S., J. Avidor, and B. Vidne, *Haemodynamics of coronary artery-saphenous vein bypass*. J Biomed Eng, 1985. **7**(4): p. 305-9.
136. Klimach, O., et al., *An investigation into how the geometry of an end-to-side arterial anastomosis affects its function*. British Journal of Surgery, 1984. **71**(1): p. 43-45.
137. Wesly, R.L., et al., *Static linear and nonlinear elastic properties of normal and arterialized venous tissue in dog and man*. Circ Res, 1975. **37**(4): p. 509-20.
138. Han, H.C., S. Marita, and D.N. Ku, *Changes of opening angle in hypertensive and hypotensive arteries in 3-day organ culture*. J Biomech, 2006. **39**(13): p. 2410-8.
139. Vesely, J., et al., *The Influence of the Opening Angle on the Stress Distribution through the Saphenous Vein Wall*, in *6th European Conference of the International Federation for Medical and Biological Engineering*, I. Lacković and D. Vasic, Editors. 2015, Springer International Publishing. p. 399-402.
140. Lüscher, T.F., et al., *Implications of pulsatile stretch on growth of saphenous vein and mammary artery smooth muscle*. The Lancet, 1992. **340**(8824): p. 878-879.
141. Soyombo, A.A., G.D. Angelini, and A.C. Newby, *Neointima formation is promoted by surgical preparation and inhibited by cyclic nucleotides in human saphenous vein organ cultures*. The Journal of Thoracic and Cardiovascular Surgery, 1995. **109**(1): p. 2-12.
142. Kockx, M.M., et al., *Longitudinally oriented smooth muscle cells in rabbit arteries*. Virchows Arch A Pathol Anat Histopathol, 1993. **422**(4): p. 293-9.
143. Pietila, K. and T. Nikkari, *Role of the arterial smooth muscle cell in the pathogenesis of atherosclerosis*. Med Biol, 1983. **61**(1): p. 31-44.

144. Edwards, W.S., W.F. Holdefer, and M. Mohtashemi, *The importance of proper caliber of lumen in femoral-popliteal artery reconstruction*. Surg Gynecol Obstet, 1966. **122**(1): p. 37-40.
145. Binns, R.L., et al., *Optimal graft diameter: effect of wall shear stress on vascular healing*. J Vasc Surg, 1989. **10**(3): p. 326-37.
146. Cheng, A. and M.S. Slaughter, *How I choose conduits and configure grafts for my patients— rationales and practices*. Annals of Cardiothoracic Surgery, 2013. **2**(4): p. 527-532.
147. Parissis, H., B.C. Ramesh, and B. Al-Alao, *Which is the best graft for the right coronary artery?* Asian Cardiovascular and Thoracic Annals, 2014.
148. Raja, S.G., et al., *Saphenous Vein Grafts: To Use or Not to Use?* Heart, Lung and Circulation, 2004. **13**(4): p. 403-409.
149. Weizsacker, H.W. and T.D. Kampp, *Passive elastic properties of the rat aorta*. Biomed Tech (Berl), 1990. **35**(10): p. 224-34.
150. Rachev, A., *A theoretical study of mechanical stability of arteries*. J Biomech Eng, 2009. **131**(5): p. 051006.
151. Jackson, Z.S., A.I. Gotlieb, and B.L. Langille, *Wall Tissue Remodeling Regulates Longitudinal Tension in Arteries*. Circulation Research, 2002. **90**(8): p. 918-925.
152. Jackson, Z.S., et al., *Partial off-loading of longitudinal tension induces arterial tortuosity*. Arterioscler Thromb Vasc Biol, 2005. **25**(5): p. 957-62.
153. Desai, M., A.M. Seifalian, and G. Hamilton, *Role of prosthetic conduits in coronary artery bypass grafting*. Eur J Cardiothorac Surg, 2011. **40**(2): p. 394-8.
154. Borschel, G.H., et al., *Tissue engineering of recellularized small-diameter vascular grafts*. Tissue Eng, 2005. **11**(5-6): p. 778-86.
155. L'heureux, N., et al., *A completely biological tissue-engineered human blood vessel*. The FASEB Journal, 1998. **12**(1): p. 47-56.
156. Mitchell, S.L. and L.E. Niklason, *Requirements for growing tissue-engineered vascular grafts*. Cardiovasc Pathol, 2003. **12**(2): p. 59-64.
157. Wang, X., et al., *Development of Small-Diameter Vascular Grafts*. World Journal of Surgery, 2007. **31**(4): p. 682-689.
158. Clark, J.M. and M.D. Hirtenstein, *Optimizing culture conditions for the production of animal cells in microcarrier culture*. Ann N Y Acad Sci, 1981. **369**: p. 33-46.
159. Hirtenstein, M., et al., *Microcarriers for animal cell culture: a brief review of theory and practice*. Dev Biol Stand, 1980. **46**: p. 109-16.
160. Van Wezel, A.L., *Growth of Cell-strains and Primary Cells on Micro-carriers in Homogeneous Culture*. Nature, 1967. **216**(5110): p. 64-65.
161. Mignot, G., et al., *Production of recombinant Von Willebrand factor by CHO cells cultured in macroporous microcarriers*. Cytotechnology, 1990. **4**(2): p. 163-71.
162. Nikolai, T.J. and W.S. Hu, *Cultivation of mammalian cells on macroporous microcarriers*. Enzyme Microb Technol, 1992. **14**(3): p. 203-8.
163. Cox, R.H., *Comparison of arterial wall mechanics using ring and cylindrical segments*. Vol. 244. 1983. H298-H303.
164. Hoeltzel, D.A., et al., *Strip Extensiometry for Comparison of the Mechanical Response of Bovine, Rabbit, and Human Corneas*. Journal of Biomechanical Engineering, 1992. **114**(2): p. 202-215.
165. Sokolis, D.P., *Passive mechanical properties and structure of the aorta: segmental analysis*. Acta Physiologica, 2007. **190**(4): p. 277-289.
166. Tanaka, T.T. and Y.-C. Fung, *Elastic and inelastic properties of the canine aorta and their variation along the aortic tree*. Journal of Biomechanics. **7**(4): p. 357-370.

167. Holzapfel, G.A., et al., *Determination of layer-specific mechanical properties of human coronary arteries with nonatherosclerotic intimal thickening and related constitutive modeling*. Vol. 289. 2005. H2048-H2058.
168. Konig, G., et al., *Mechanical properties of completely autologous human tissue engineered blood vessels compared to human saphenous vein and mammary artery*. Biomaterials, 2009. **30**(8): p. 1542-50.
169. Quint, C., et al., *Allogeneic human tissue-engineered blood vessel*. Journal of Vascular Surgery, 2012. **55**(3): p. 790-798.
170. L'Heureux, N., et al., *Human tissue-engineered blood vessels for adult arterial revascularization*. Nat Med, 2006. **12**(3): p. 361-365.
171. Pellegata, A.F., et al., *Detergent-Enzymatic Decellularization of Swine Blood Vessels: Insight on Mechanical Properties for Vascular Tissue Engineering*. BioMed Research International, 2013. **2013**: p. 8.
172. Quint, C., et al., *Allogeneic human tissue-engineered blood vessel*. J Vasc Surg, 2012. **55**(3): p. 790-8.
173. Sheridan, W.S., G.P. Duffy, and B.P. Murphy, *Mechanical characterization of a customized decellularized scaffold for vascular tissue engineering*. J Mech Behav Biomed Mater, 2012. **8**: p. 58-70.
174. Roach, M.R. and A.C. Burton, *THE REASON FOR THE SHAPE OF THE DISTENSIBILITY CURVES OF ARTERIES*. Canadian Journal of Biochemistry and Physiology, 1957. **35**(8): p. 681-690.
175. Martin, Y., et al., *Microcarriers and their potential in tissue regeneration*. Tissue Eng Part B Rev, 2011. **17**(1): p. 71-80.
176. Voigt, M., et al., *Cultured epidermal keratinocytes on a microspherical transport system are feasible to reconstitute the epidermis in full-thickness wounds*. Tissue Eng, 1999. **5**(6): p. 563-72.
177. Liu, J.Y., et al., *Autologous cultured keratinocytes on porcine gelatin microbeads effectively heal chronic venous leg ulcers*. Wound Repair Regen, 2004. **12**(2): p. 148-56.
178. Kim, S.S., et al., *Skin regeneration using keratinocytes and dermal fibroblasts cultured on biodegradable microspherical polymer scaffolds*. J Biomed Mater Res B Appl Biomater, 2005. **75**(2): p. 369-77.
179. Gustafson, C.J., et al., *Employing human keratinocytes cultured on macroporous gelatin spheres to treat full thickness-wounds: an in vivo study on athymic rats*. Burns, 2007. **33**(6): p. 726-35.
180. Lippens, E., et al., *Evaluation of bone regeneration with an injectable, in situ polymerizable Pluronic F127 hydrogel derivative combined with autologous mesenchymal stem cells in a goat tibia defect model*. Tissue Eng Part A, 2010. **16**(2): p. 617-27.
181. Yang, Y., B. Hallgrímsson, and E.E. Putnins, *Craniofacial defect regeneration using engineered bone marrow mesenchymal stromal cells*. J Biomed Mater Res A, 2011. **99**(1): p. 74-85.
182. Clavijo-Alvarez, J.A., et al., *Comparison of biodegradable conduits within aged rat sciatic nerve defects*. Plast Reconstr Surg, 2007. **119**(6): p. 1839-51.
183. Seliktar, D., R.M. Nerem, and Z.S. Galis, *Mechanical strain-stimulated remodeling of tissue-engineered blood vessel constructs*. Tissue Eng, 2003. **9**(4): p. 657-66.
184. Zhang, X., et al., *Dynamic culture conditions to generate silk-based tissue-engineered vascular grafts*. Biomaterials, 2009. **30**(19): p. 3213-23.
185. Seliktar, D., et al., *Dynamic mechanical conditioning of collagen-gel blood vessel constructs induces remodeling in vitro*. Ann Biomed Eng, 2000. **28**(4): p. 351-62.

186. Parks, W.C., M.E. Kolodziej, and R.A. Pierce, *Phorbol ester-mediated downregulation of tropoelastin expression is controlled by a posttranscriptional mechanism*. *Biochemistry*, 1992. **31**(29): p. 6639-6645.
187. Opitz, F., et al., *Tissue engineering of aortic tissue: dire consequence of suboptimal elastic fiber synthesis in vivo*. *Cardiovasc Res*, 2004. **63**(4): p. 719-30.
188. Zou, Y. and Y. Zhang, *An experimental and theoretical study on the anisotropy of elastin network*. *Ann Biomed Eng*, 2009. **37**(8): p. 1572-83.
189. Hinek, A., et al., *Retrovirally mediated overexpression of versican v3 reverses impaired elastogenesis and heightened proliferation exhibited by fibroblasts from Costello syndrome and Hurler disease patients*. *Am J Pathol*, 2004. **164**(1): p. 119-31.
190. Merrilees, M.J., et al., *Retrovirally mediated overexpression of versican v3 by arterial smooth muscle cells induces tropoelastin synthesis and elastic fiber formation in vitro and in neointima after vascular injury*. *Circ Res*, 2002. **90**(4): p. 481-7.
191. Snyder, J.C., A.C. Zemke, and B.R. Stripp, *Reparative capacity of airway epithelium impacts deposition and remodeling of extracellular matrix*. *Am J Respir Cell Mol Biol*, 2009. **40**(6): p. 633-42.
192. Chen, L., et al., *Positional differences in the wound transcriptome of skin and oral mucosa*. *BMC Genomics*, 2010. **11**: p. 471.
193. Gonye, G.E., et al., *From promoter analysis to transcriptional regulatory network prediction using PAINTE*. *Methods Mol Biol*, 2007. **408**: p. 49-68.
194. Hofmann, C.S., et al., *B-Myb represses elastin gene expression in aortic smooth muscle cells*. *J Biol Chem*, 2005. **280**(9): p. 7694-701.
195. Chue, W.-L., et al., *Dog peritoneal and pleural cavities as bioreactors to grow autologous vascular grafts*. *Journal of Vascular Surgery*, 2004. **39**(4): p. 859-867.
196. Nieponice, A., et al., *Development of a tissue-engineered vascular graft combining a biodegradable scaffold, muscle-derived stem cells and a rotational vacuum seeding technique*. *Biomaterials*, 2008. **29**(7): p. 825-33.
197. L'Heureux, N., et al., *Human tissue-engineered blood vessels for adult arterial revascularization*. *Nat Med*, 2006. **12**(3): p. 361-5.
198. Niklason, L.E., et al., *Functional Arteries Grown in Vitro*. *Science*, 1999. **284**(5413): p. 489-493.
199. Lee, K.-W., D.B. Stolz, and Y. Wang, *Substantial expression of mature elastin in arterial constructs*. *Proceedings of the National Academy of Sciences*, 2011. **108**(7): p. 2705-2710.

LIST OF PUBLICATIONS

Journal Papers

1. Boran Zhou, Lauren Wolf, Alexander Rachev, Tarek SHAZLY, "A *Structure-motivated Model of the Passive Mechanical Response of the Primary Porcine Renal Artery*". *Journal of Mechanics in Medicine and Biology*, 2014. 14(03): p. 1450033.
2. Twal Waleed, Klatt Sandra, Harikrishnan Keerthi, Gerges Ebtesam, Cooley Marion, Trusk Thomas, Boran Zhou, Mohamed Gabr, Tarek Shazly, Susan Lessner, Roger Markwald, Williams. S. Argraves, "*Cellularized Microcarriers as Adhesive Building Blocks for Fabrication of Tubular Tissue Constructs*." *Annals of Biomedical Engineering*, 2013: p. 1-12.
3. Tarek Shazly, Alexander Rachev, Susan Lessner, Williams Argraves, Ferdous Jahid, Boran Zhou, Alexandria Moreira, Michael Sutton, "*On the Uniaxial Ring Test of Tissue Engineered Constructs*". *Experimental Mechanics*, 2014: p. 1-11.
4. Boran Zhou, Alexander Rachev, Tarek Shazly, "*Active Stresses in the Porcine Primary Renal Artery*", in preparation.
5. Boran Zhou*, David Primm*, Tarek Shazly, John Eberth, "*Mechanical Analysis of Coronary Artery Bypass Vessels*", in preparation, * INDICATES EQUAL AUTHOR CONTRIBUTION.

6.

Comference Presentations

1. Boran Zhou, Alexander Rachev, Tarek Shazly, “*Active Stress in the Porcine Renal Artery*”, SBC 2013, Oregon.
2. Mohamed Gabr, Boran Zhou, Sandy Klatt, Tarek Shazly, Susan M. Lessner and W. Scott Argraves, “*Mechanical Response of Tissue Constructs Fabricated From Self-Adhering Cellularized Microcarriers*”, SBC 2013, Oregon.
3. Boran Zhou, Mohamed Gabr, Sandy Klatt, Waleed O Twal, Tarek Shazly, Susan Lessner, William Argraves, “*Mechanical Characterization of Cellularized and Decellularized Tissue Constructs*”, BMES 2013 Annual Meeting, Seattle.
4. Boran Zhou, Tarek Shazly, Gregory Brower, Heather Doviak, Frank Spinale , “*Active Stresses In The Porcine Common Carotid Artery*” , BMES 2014 Annual Meeting, San Antonio.
5. David Primm, Boran Zhou, Tarek Shazly, John Eberth, “*Mechanical Analysis of Coronary Artery Bypass Vessels*”, NCTERMS14.